APPLICATION OF THE CROSS-HOLE RADIO IMAGING METHOD IN DETECTING GEOLOGICAL ANOMALIES, MACLENNAN TOWNSHIP, SUDBURY ONTARIO

by

Ladan Karimi Sharif

A thesis submitted in partial fulfillment
of the requirements for the degree of
Master of Science (MSc) in Geology

The School of Graduate Studies
Laurentian University
Sudbury, Ontario, Canada

THESIS DEFENCE COMMITTEE/COMITÉ DE SOUTENANCE DE THÈSE

Laurentian Université/Université Laurentienne
School of Graduate Studies/École des études supérieures

Title of Thesis Titre de la thèse	APPLICATION OF THE CROSS-HOLE RADIO IMAGING METHOD IN DETECTING GEOLOGICAL ANOMALIES MACLENNAN TOWNSHIP, SUDBURY ONTARIO
Name of Candidate Nom du candidat	Karimi Sharif, Ladan
Degree Diplôme	Master of Science
Department/Program Département/Programme	Geology
Date of Defence Date de la soutenance	September 18, 2013

APPROVED/APPROUVÉ

Thesis Examiners/Examinateurs de thèse:

Dr. Richard Smith
(Supervisor/Directeur de thèse)

Dr. Bruno Lafrance
(Committee member/Membre du comité)

Glenn McDowell
(Committee member/Membre du comité)

Dr. Ian J. Ferguson
(External Examiner/Examinateur externe)

Approved for the School of Graduate Studies
Approuvé pour l'École des études supérieures
Dr. David Lesbarrères
Mr. David Lesbarrères
Director, School of Graduate Studies
Directeur, École des études supérieure

ACCESSIBILITY CLAUSE AND PERMISSION TO USE

Abstract

The occurrence of conductive sulphide in an otherwise highly-resistive host rock is the ideal situation for exploring using high-frequency electromagnetic methods. The FARA radio imaging (RIM) system was deployed to explore the rock properties between two boreholes MAC104 and MAC100G, which are about 182 m apart, on the Nickel Rim South property (MacLennan Township) 22 km northeast of Sudbury. Tomographic data were collected and processed at 625 kHz and 1250 kHz. One data set has the transmitter in MAC100G and the receiver in MAC104; the other "reciprocal" data set has the transmitter in MAC104 and the receiver in MAC100G. The amplitude data were reduced, edited, and processed to generate tomograms employing the SIRT algorithm. Separate tomograms were created for the reciprocal data sets in the ImageWin software. A sensitivity analysis was conducted to assess the influence that perturbations in the ImageWin processing parameters have on the resulting tomograms. The sensitivity study of the tomograms along with the information obtained from the value of fit analysis can be used to select appropriate processing parameters. Finally, the two reciprocal sets of conductivity values were averaged and imported into Geosoft to create a final tomogram for the panel.

The resistivity values of the studied zone obtained from the FARA modeling package agree fairly well with the conductivity data set generated by the ImageWin modeling package when compared using the Geosoft and GOCAD visualization software. Differences between the two tomograms are attributed to the different solver methods employed by FARA and ImageWin and the statistical analysis used for averaging the attenuation value over ray paths. Furthermore, it is

shown that the tomographic results are consistent with the location of conductive zones that were identified using down-hole geophysical logging.

The main focus of the project is to understand how the radio imaging (RIM) data is processed with the ImageWin software to construct an attenuation tomogram.

This research showed that both tomograms created by ImageWin and FARA illustrate the same pattern with two conductive zones at the same depth; however, the values of conductivity are slightly different. The FARA resistivity values obtained for the upper zone is a factor of two lower than the resistivity calculated by ImageWin. The resistivity values obtained for the lower zone using the FARA processing is a factor of eight lower than the resistivity calculated by ImageWin. Also, there is a slight discrepancy in the orientation of the upper and lower zones on the two tomographic images generated using the two processing packages. In the tomograms generated by FARA software both upper and lower zones are continuous linear zones from one hole to the other with dips from MAC104 towards MAC100G, whereas in the tomograms created by ImageWin the upper and lower zones are less linear and do not have obvious dips.

Keywords: radio-imaging-method, cross-holes, geophysical-tomograms, boreholes, ImageWin

Acknowledgments

I would like to thank Professor Richard Smith for providing me with the much appreciated supervision which allowed for the successful completion of this project. I owe particular thanks to my industrial supervisor Warren Hughes for sharing with me his knowledge and expertise. Also, I would like to thank Dr. Peter Fullagar for his continued support during this project.

I am most grateful to the members of Supervisory Committee Dr. Glenn McDowell, Dr. Bruno Lafrance, and Dr. Ian J. Ferguson for their useful suggestions and constructive comments on earlier drafts.

I would like to extend my sincere thanks and appreciation to Sudbury Integrated Nickel Operations, Vale, Wallbridge Mining, KGHM International, Center for Excellence in Mining Innovation, and NSERC for their financial support.

I would like to particularly thank my family who have supported me throughout the years without complaint; I realize and appreciate all that you have done for me.

Table of Contents

List of Tables

List of Figures

1 Introduction

The cross-hole Radio Imaging (RIM) method has a transmitter in one hole that emits high frequency electromagnetic (EM) wave that is monitored with a receiver in another hole. As the EM wave travels from the transmitter to the receiver, the energy of the EM wave is absorbed by geological features in the intervening material. The method exploits the fact that the attenuation and velocity of EM waves vary in the presence of geological features. The attenuation of the propagating wave is measured, and normally given in dB per meter. The attenuation is used to characterises the geological features: The more conductive a geological feature is, the greater the EM attenuation. The primary focus of the current research project is to construct and interpret the attenuation tomograms obtained from the RIM data using the ImageWin software.

In Sudbury, RIM data is collected by the company GEOFARA using the FARA equipment. This equipment measures the raw amplitude (signal strength) and phase of the electromagnetic wave at the receiving antenna. In this thesis, these data are processed so that tomograms can be constructed and used to interpret the data. These tomograms will be generated via a number of steps. First, the total absorption coefficient values for each of the ray paths are calculated from the measured recorded data. Then the investigation area is divided into identical cells and the absorption coefficient will be calculated for each cell and then the attenuation rate tomogram will

be calculated for the surveyed area. The resulting image should demonstrate the physical rock properties of the area investigated.

These results will be compared against the ground-truth geological and logging data in and around the two holes. The comparisons are presented using the LogView software. Through such studies, the strengths and weaknesses of the RIM technology for locating the geological features will be assessed.

The thesis aims to provide insight into how the ImageWin software works and how it can be effectively used to analyze and visualize RIM data. A sensitivity analysis is performed to examine the impact of a number of parameters by seeing how systematically adjusting these parameters change the tomographic images. The preferred tomograms created by ImageWin will be compared to the tomogram constructed by a different software analysis package used by GEOFARA. The comparison is intended to explore the pros and cons of each software and understand their capabilities and characteristics.

2 Literature Review

The radio imaging method is a non-contact electromagnetic method that can be used to provide an image of the distribution of the ground conductivity. The method uses a transmitter emitting radio frequency electromagnetic radiation in one borehole (or access tunnel) and a receiver in another borehole (or access tunnel). By placing the transmitter at multiple positions in the borehole or tunnel and having the receiver occupy multiple positions for each transmitter position (or vice versa) it is possible to construct a tomographic image. Hence, the mode of acquiring this data is similar to how medical Computed Tomography (CT) data are acquired (Kruger et al. 1999).

Electromagnetic waves propagate without significant attenuation through resistive material such as coal seams, but can be reflected or attenuated by conductive rock or a nickel sulphide vein (Wait, 1976). In the space between the two drill holes there might be intrusions, dykes, faults, fracture zones, etc. These geological features alter the velocity of electromagnetic wave propagation and the attenuation of the wave's amplitude (the rate of signal dissipation with respect to a distance along the ray path, normally measured in dB/m).

The utility of the method is that the RIM images can reduce the need for more drill holes, improve the possibility of discovering additional conductive zones, permit early recognition of mining hazards, and expedite cost-efficient mine planning (Fallon, Fullagar and Sheard 1997).

The ability of the RIM measurements to detect highly conductive zones in resistive host rock makes the method ideal for use in the Sudbury area, as the host rock in Sudbury is resistive and the only significantly conductive material is ore (Watts, 1997). The application of this method is not restricted to geophysical exploration; it can also be applied to a wide variety of other fields as discussed below.

2.1 A brief history of the electromagnetic methods

Tomographic imaging can be generated based on the equations developed by J.C. Maxwell (1831-1879) describing the propagation of electromagnetic radiation such as light and radio waves. Twenty years later, Heinrich Hertz (1857-1894) generated radio waves in a laboratory (Sengupta and Sarkar, 2003). Subsequently, radio waves have been used for transmitting information through the earth's atmosphere and space. Such radio waves are in the frequency range of roughly 30 kHz to 300 GHz corresponding to wavelengths between 10,000 meters and 1 millimetre.

Different frequencies of electromagnetic waves experience different amounts of reflection, refraction, polarization, diffraction and absorption (Bohren and Huffman, 2008). For instance, visible light being reflected off objects allows us to see outlines of the objects and their textures. Variable reflection and/or absorption at different frequencies allow us to identify different colors of objects. If we are on the other side of an object from the source of electromagnetic radiation,

then absorption of the light allows us to infer the presence of the object by the shadow or lack of light. Higher frequency radiation, such as X-rays, allows us to see inside the body as the energy is absorbed to different extents: tissue provides little absorption, while bones absorb a greater amount of the radiation (Manohara et al., 2011).

Electromagnetic methods in exploration geophysics generally cover a broad range of frequencies, the depth of penetration of these methods generally being a function of the frequency used. There are three main classes of methods. Diffusive methods (e.g. audiomagnetotellurics) operate at low frequencies from tens of Hz to up to a few tens of kHz, which corresponds to depths between ten of meters up to a few kilometers (Wilkinson, 2005). The radio imaging method is an intermediate frequency range from 312.5 kHz to 2500 kHz with penetration distances of the orders of hundreds of meters in resistive rock (Wilkinson, 2005). The ground penetrating radar method operates in the highest range of frequencies from tens to hundreds of MHz (10MHz-1GHz) which corresponds to depths of a few meters in typical rock (Nuzzo et al., 2002). The ability of the radio wave in the intermediate frequency range to penetrate through resistive rocks and to be attenuated by an electrically conductive object (Manohara et al., 2011) also supports the conclusion that Sudbury ore bodies are highly suitable for RIM investigations. The theory behind the radio imaging method (RIM) was advanced approximately twenty years ago (Wait, 1976).

2.2 History of EM wave geophysical methods

The very first use of the radio imaging method dates back to 1910 when it was employed to detect geological features between holes (Thomson and Hinde, 1993). The attenuation characteristics of the radio waves underwent investigation in Germany in the 1930s (Rust, 1938). However, it was not until the 1970s that Lytle and others did scientific work on generating geotomographic images and raised the level of interest of the geophysical community (Spies, 1996). An experiment for measuring the subsurface electrical properties of rocks on the moon was undertaken as part of the Apollo 17 mission in the 1967. Subsequent work has been undertaken by the Geological Survey of Canada and the United States Army Cold Regions Research and Engineering Laboratory (Monaghan, 2007).

The method has also been tested in the Australian coal mining industry and has been applied as well to base metal deposits in the Mount Isa area. In the latter case, M.I.M. Exploration Pty Ltd undertook in-mine and borehole surveys in and around the Hilton Mine, using medium-frequency radio waves of 20-520 kHz to delineate the intervening electrical conductivity of the rock mass. This was used to infer the amount of Pb/Zn mineralization (Thomson et al., 1992).

Subsequently the mining industry has displayed a developing interest in this technology to detect and delineate geological conditions. The Quecreek mining accident that took place on July 24,

2002, has highlighted the importance of using the radio imaging method to enhance mine safety by investigating the hazards associated with mine voids (Commonwealth of Pennsylvania, 2002).

2.3 Other applications of radio tomography

2.3.1 Seeing through walls

Radio tomography networks have been used for tracking the location of a person or object through walls. The main advantage of the method is the ability to scan without the necessity for electronic devices on the target. The changes in signal strength caused by moving physical objects are used as a guide to locate and identify the target. This particularly helps police, military forces and firefighters when entry is not possible or is likely threatening. Hence radio tomography is considered as a life-saving method. The main objective of the research in this area is to propose a model which can best relate motion in spatial voxels to the changes in signal strength measured at the receiver locations (Wilson and Patwari, 2011).

Wilson and Patwari (2011) show that the amplitude and phase of an electromagnetic wave is a strong function of spatial positions of conductive objects and zones relative to the location of the transmitter and receiver. In other words, the area of highly attenuated signals moves in accordance with the location of moving object relative to the receiver and transmitter. In this case, the physics of electromagnetic waves will provide a powerful tool to understand, visualize, and interpret the constructed tomograms from the attenuation field. The use of ray path losses on

links between many pairs of nodes is demonstrated on the image within the network area in Figure 2-1(Wilson and Patwari, 2011).

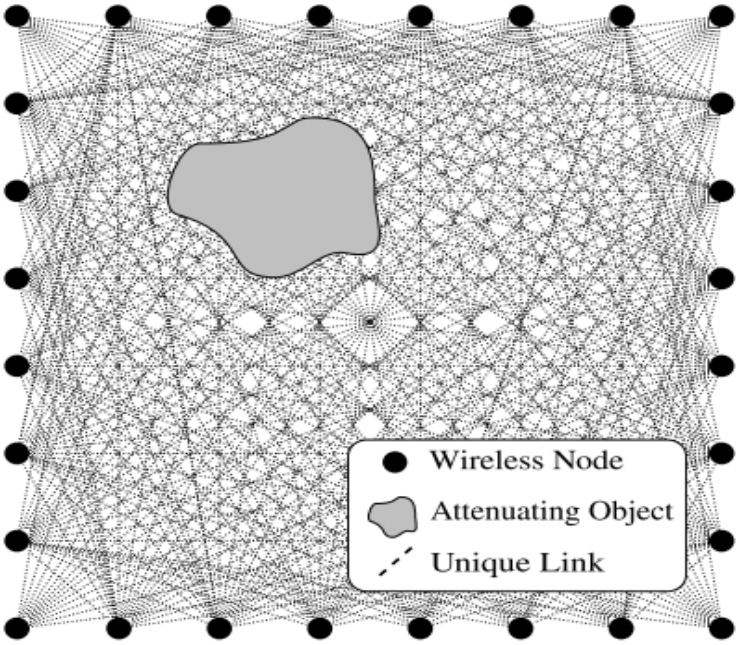

Figure 2-1: Display of a radio tomographic imaging network; each node transmits to the others, creating many projections used to reconstruct the image of objects inside the network area, adapted from (Wilson and Patwari 2011).

2.3.2 Medical tomographic imaging

The radio imaging method has been used in medical imaging of the human breast at an operating frequency of 434 MHz in the prototype thermoacoustic CT scanner (Kruger et al. 1999). In this method, the electric signals were employed to build a three-dimensional data set and the images

were generated in multiple slices. The attenuation of energy at radio frequencies in biological tissue is governed by its electrical properties such as dielectric permittivity and conductivity. The energy absorption coefficient (α) is modified with these three parameters and also with the radio frequency, as seen in the following formula (Kruger et al. 1999):

$$\boldsymbol{\alpha(f,\sigma,\varepsilon) = 4\pi f \sqrt{\frac{\mu_0\varepsilon_0}{2}\left(\sqrt{1+\frac{\sigma}{2\pi f\varepsilon_0\varepsilon}}-1\right)}} \qquad \textbf{(2-1)}$$

where μ_0 is the permeability and ε_0 is the permittivity of free space, f is the frequency, ε is the relative permittivity of tissue and σ is the conductivity of the tissue. The measured changes in absorption reflect changes in the conductivity and permittivity of tissues, which generally reflect changes in the fractional water content. The absorption coefficient for soft and fat tissues has been computed by using this model. The calculated absorption coefficient values in cancerous breast tissues are two to five times more powerful than are surrounding normal breast tissues in the range of 300-500 MHz. Considering that thermoacoustic CT method can be operated at any electromagnetic frequency, many areas of the electromagnetic spectrum may now be appropriate for medical imaging—such as the visible, infrared, RF, and microwave regions (Kruger et al. 1999).

2.3.3 Imaging coal seams and mining hazards with the Radio Imaging Method (RIM)

The coal seam is an electrical insulator with relatively high electrical resistance. Generally a coal seam will be surrounded by a more conductive medium which acts as a waveguide in the frequency range from 10 kHz to 500 kHz (Stolarczyk et al., 2003). The lower-frequencies penetrate a larger distance in comparison to the higher frequencies, because the attenuation rate increases with frequency. Importantly, the dielectric properties of the coal seam can be impacted by structures that cut across the coal seam like dykes and fault zones.

The first RIM surveys in coal mines were carried out in 1985 and 1986 by Mr. Roger Fry, Senior Geologist at Utah Power and Light Company, and Stephen Doe, Senior Geologist at American Electric Power's Meigs Division mining complex (Stolarczyk et al., 2003). These coal surveys were undertaken as in-mine surveys, with the transmitters and receivers in access tunnels on either side of the volume being investigated. Since then, radio imaging method has been applied to mapping features of coal seams in the United States, Australia, New Zealand, South Africa, and the United Kingdom. The RIM method is a money-saving instrument as it can detect geological anomalies and voids in coal beds. The contrast of the physical properties between the coal bed and the scours, dykes, partings and faults (Figure 2-2) means that RIM is able to identify and delineate these anomalous zones (Stolarczyk et al., 2003).

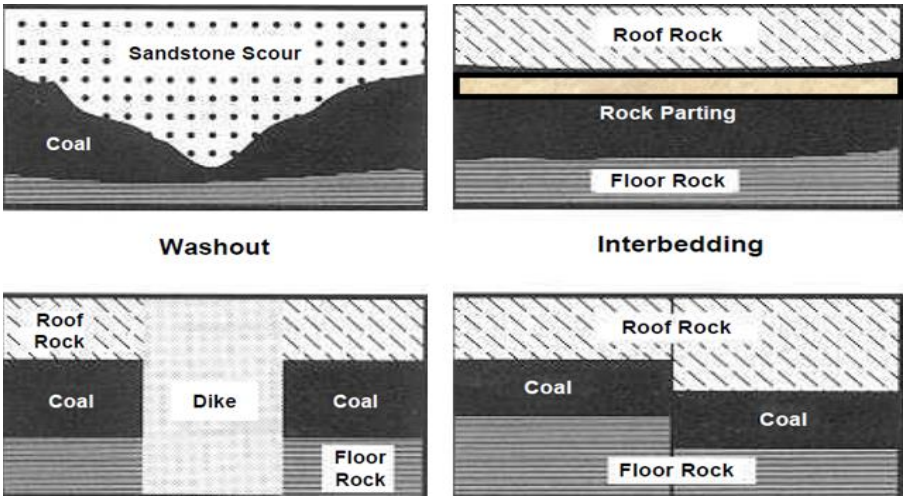

Figure 2-2: Typical coal seam anomalies (Stolarczyk et al., 2003).

In a coal mine, dikes, faults, paleochannels, and the associated perched aquifers (Figure 2-3) are potential mining hazards. In some cases these zones are associated with roof falls (Stolarczyk et al., 2003). Identifying these zones will enhance mine safety, productivity and coal recovery.

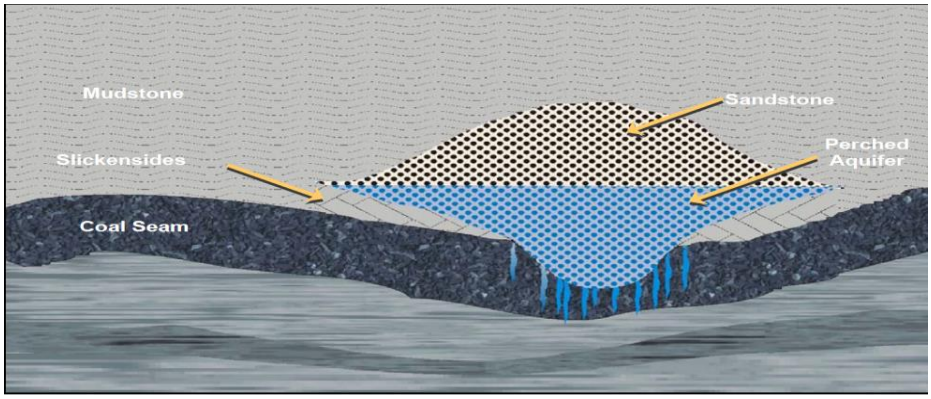

Figure 2-3: Cross section of paleochannel (Stolarczyk et al., 2003).

Stolarczyk et al. (2003) describes a RIM survey of a barrier pillar (the area of solid coal between the old works and planned works). The objective of this survey was to identify the zone below the paleochannel, where the high pressure water and gas are trapped in slip fault that was ahead of the coal mining face. The RIM tomography surveys can map zones of higher attenuation associated with the water-filled fault zones. The survey did not detect a water filled zone, but identified the shape, orientation and thickness of a dyke that attenuated the RIM signal more than the coal seam.

In this survey, the algebraic reconstruction technique (ART) was used to calculate the RIM tomograms. This algorithm assumes that the signal at a fixed frequency travels on a straight ray path with the amplitude of the EM wave being attenuated by increasing distance traveled. The ray's signal energy changes when it interacts with geological anomalies, faults, dykes, paleochannels, seam thinning and increased water in the seam (Stolarczyk et al., 2003).

Underground mine accidents can be very destructive and result in loss of life. One example is the 1968 Farmington Mine Disaster which took place in the coal mine north of Farmington and Mannington, West Virginia, which killed 79 miners. A second example is the Willberg Mine disaster which occurred in a coal mine in Emery County, Utah, in December 1984 and killed 28 miners. The damage and loss of life encouraged the National Research Council of Canada (NRC) to consider a course of action to improve underground mining safety (Stolarczyk, 2012). The

scientific investigations by the company Stolar have shown that radio geophysics can assist in identifying zones of potential mine accidents.

RIM surveys have been carried out after the accident at the Quecreek Mine (Somerset County, Pennsylvania). Studies using a DLRG (deep look ground penetrating radar gradiometer) concluded that the accident occurred due to the lack of information about mine voids (Stolarcyzk, 2012). Stolarcyzk (2012) using the RIM method (RIM-6 instrumentation) with transmitters and receivers in the underground workings at Quecreek, mapped the intrusions into a coal seam and located the ancient boreholes from the surface which are a potential source of water in-rush hazards (Stolarczyk, 2012).

The RIM method has also been tested in the coal mining industry in Australia. In one cross-hole experiment RIM was a useful tool for defining ore shapes between holes. The survey was undertaken between two boreholes with 30 m separation using 300 kHz horizontal magnetic-dipole loop antennas. A tomographic image of the high conductivity zone between boreholes was created (Thomson et al., 1992).

2.3.4 Metaliferous mines

The RIM method has excellent potential applications for different base metal sulphide deposits. This is because the host rock can be resistive and the ore can attenuate or reflect the waves. The Russian scientists have undertaken a number of tests of RIM, which they call the “radio wave

shadow" (RWS) method (Nickel et al., 1989). Tests of the Russian equipment in base metal deposits in Czechoslovakia and Yugoslavia by the Federal Institute for Geosciences and Natural Resources (BGR) in Germany have been documented by Nickel and Cerny (1989). They use five different frequencies between 10 and 30 MHz and deploy moveable transmitters and receivers in a cross-hole mode. The method produced promising results, imaging the metal sulphide deposits.

Another location where the RIM method was tested in a cross-hole configuration, for the purpose of planning mine development, was in the 1990s at the Century deposit in Queensland, Australia. Tomographic inversion images were derived from the data using software developed by VIRG-Rudgeofizika and known as the FARA RFEM algorithm, which uses both amplitude and phase information. The use of the radio imaging system at Century has inferred the presence of a fault near its known position. Mutton (2000) concluded that if the RIM method had been adequately developed and validated at the time of the Century discovery, a better evaluation of the deposit could have been obtained at a significantly lower cost by reducing the number and type of boreholes required. As well there would have been an increased level of confidence in the amount of reserves, the mine design and the mining plan (Mutton, 2000).

In 1992, the RIM method was tested in Pb/Zn mines at Mount Isa for MIM Exploration Pty Ltd (Anderson and Logan, 1992). The equipment that was used operated in the frequency range of 50 to 520 kHz and the boreholes were separated by about 64 m. Tomographic image processing carried out by the CSIRO Division of Radiophysics derived a conductivity distribution using several assumptions: the straight ray-path, the far-field approximation and homogeneous host rock (Anderson et.al., 1992). The results derived from the 50 kHz data showed two zones, one corresponding the low-grade Zn ore and second to high-grade Pb ore. Anderson and Logan (1992) concluded that the ability of the RIM method to detect geological anomalies between holes meant that the method could be useful as a mine planning tool.

In 1995 a RIM study at Mt.Isa was undertaken as a part of a CMTE/AMIRA project to detect ore in metalliferous mines. METS (Mine Exploration and Technical Services) conducted the survey using the RIM II system. The data were reduced and displayed by showing only raypaths of signals with amplitudes greater than 30 dB. This was considered as a very quick way to define the number and location of the conductive zones. The results are shown in Figure 2-4, where three conductive zones are evident as the zones where there are no ray paths (Zhou et al., 1998).

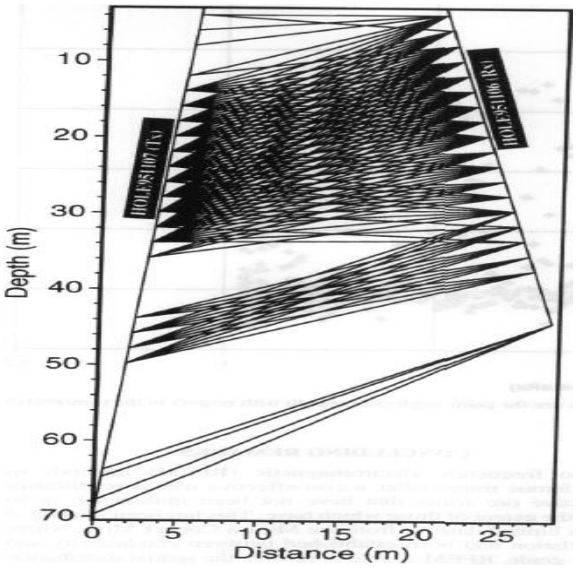

Figure 2-4: Amplitude-masked raypath coverage diagram showing rays with signal strength above 30 dB after (Zhou et al., 1998).

In South Africa, radio tomography (RT) surveys were conducted at a disseminated sulphide deposit in Mpumalanga, South Africa, using five different frequencies in the range of 500 kHz to 30000 kHz (van Schoor and Duvenhage, 1999). The RT survey was carried out using the Pluto-6 RT system developed by the Mining Technology Division (Miningtek) of the Council for Scientific and Industrial Research (CSIR) in South Africa. The Pluto-6 RT system used electric dipole antennas and measured the amplitude of the received signal. The data was processed and inverted using a maximum entropy inversion routine developed by Neil Pendock (University of the Witwatersrand) that utilized a modified gradient algorithm.

The results are shown in the form of 2D images of conductivity distribution (Figure 2-5). The color bar depicts the logarithm of the calculated resistivity (van Schoor and Duvenhage, 1999).

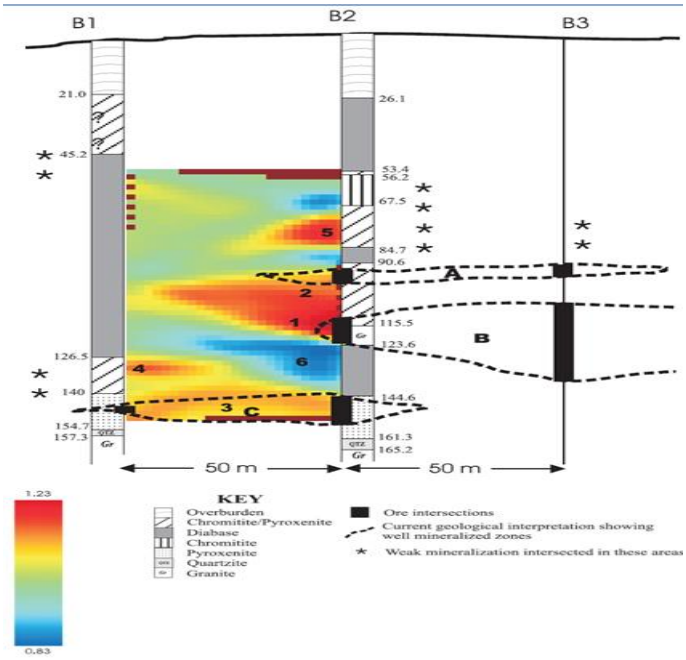

Figure 2-5: The radio tomography image obtained at 12500 kHz (Van Schoor and Duvenhage, 1999). The tomogram was constructed based on the results obtained at 12500 kHz and it shows four areas (red) of high attenuation which is in a good agreement with the geology, e.g. chromitite and pyroxenite, at different depths.

Work with the cross-hole radio imaging method was conducted at Eurajoki Olkiluoto in Finland in late 2005 (Heikkinen et al., 2006). The objective of the research was to characterize a potential site to be used for the underground disposal of waste nuclear fuel. The work was carried out jointly with Geological Survey of Finland and FGUNPP Geologorazvedka from Russia, using the FARA-MCH tool. The collar distance between holes was 250-300 m. The measured amplitude

data were reduced and processed to calculate the resistivity tomograms delineating more conductive horizons. The locations of the conductive zones were consistent with geology and the borehole geophysics logs (Heikkinen et al., 2006).

2.4 Sudbury deposits

The Sudbury Igneous Complex (SIC) is one of the largest Ni-Cu-Co and PGE ore producers in the world (Stevens et al., 2000). The lowermost unit of the complex is the Sublayer Norite (SLN) which is the contact sublayer between the Sudbury igneous complex (main mass) and the footwall rocks. Pyrrhotite, pentlandite and chalcopyrite are the main ore bearing sulphides and as they are conductive, they reflect and attenuate the signal. Measurements of the resistivity indicate that the resistivity of the host rocks is between 10 and 10000 ohm-m while the resistivity of the disseminated and massive sulphide mineralization is between 10 to 1000 times more conductive (Stevens et al., 2000).

Stevens et al. (2000) describe RIM surveys at three mine sites: Craig, Onaping and Fraser. The image in Figure 2-6 shows the location of these mines in the northwest part of the Sudbury Igneous complex. The purpose of the cross-hole surveys was to explore underground copper and nickel sulphide deposits (The equipment used four operating frequencies between 312 and 2500 kHz).

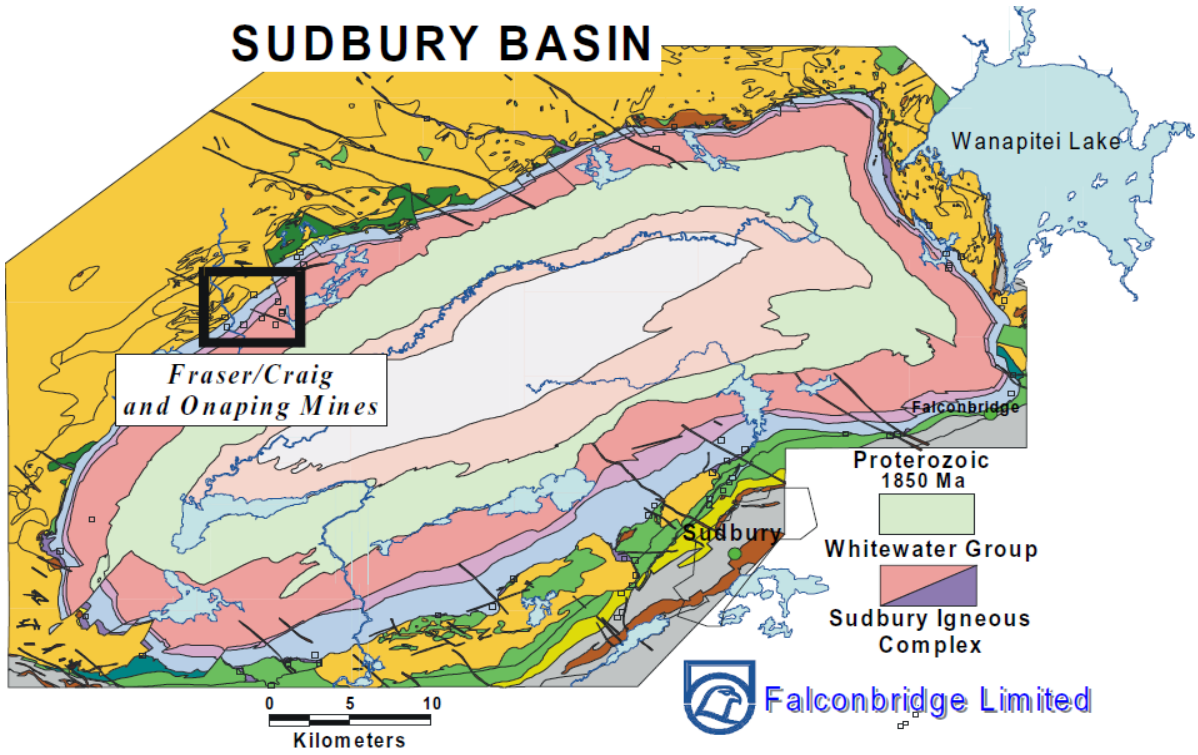

Figure 2-6: Plan view of geological features of the Sudbury Igneous Complex. Locations of the Fraser, Onaping and Craig Mine complexes are also shown (Stevens et al., 2000).

The RIM surveys at the Craig depth project were acquired in 1996 using the Chinese electric dipole cross-hole system (JW-4). The survey used two holes CD-49-003 and CD-49-001 with a 100-200 meter distance between boreholes. The 2D attenuation tomogram derived from the 1200 kHz data is shown in Figure 2-7. Several zones were detected with large attenuation coefficients in the range of 0.075-0.105 dB/m. Comparing the sulphide histograms (in black) with the 2D attenuation image, the highly attenuated zones correspond roughly to the mineralized zones.

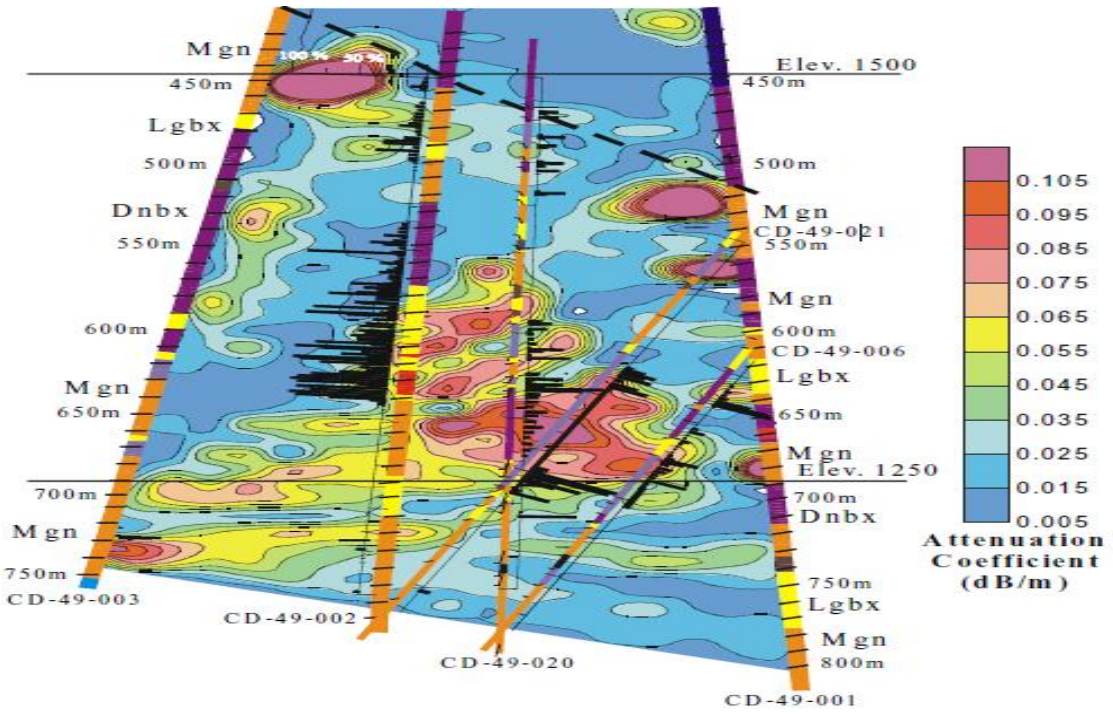

Figure 2-7: image from 1996 using JW-4 system at the Craig Mine (Stevens et al., 2000).

In the Onaping project (1998), the RIM surveys were carried out using the FARA-MF system of VIRG-RudGeofizika, of St. Petersburg, Russia. In this case, two panels of data were acquired – between holes 31 and 21 and between 21A and 26. The borehole distances were about 300 m and 200 m for these two panels respectively and useful results were obtained at a frequency of 1250 kHz. The RIM tomograms delineated the mineralization boundaries between the boreholes. In Figure 2-8, the range of resistivities estimated from the data is from 790 to 4500 ohm-m and the sulphide histogram (in white) corresponds to the highly attenuated zones with lowest resistivity of about 800-850 ohm-m (Stevens et al., 2000).

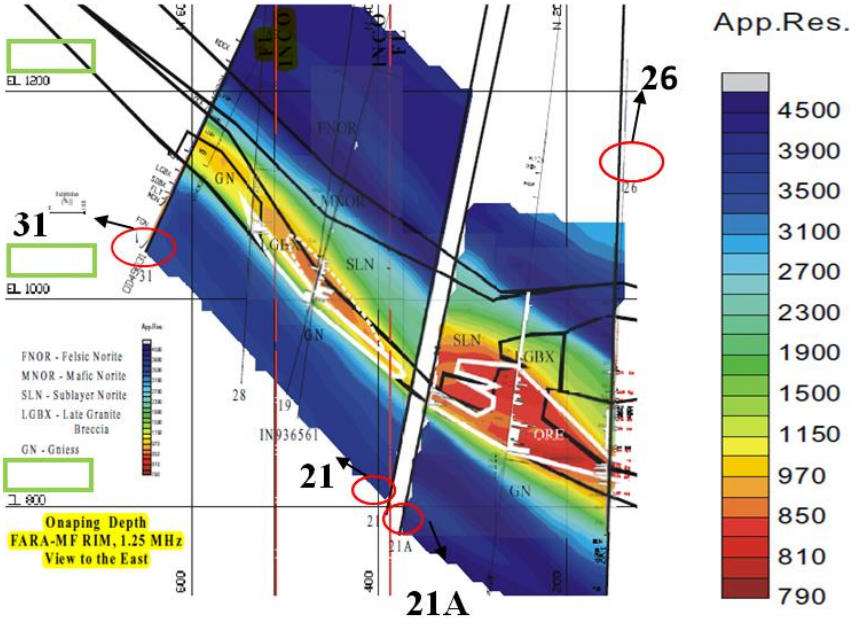

Figure 2-8: RIM image from 1998 using FARA-MF system at the Onaping Mine (Stevens et al., 2000). Elevation is in meters; the apparent resistivity (App. Res.) color bar is in ohm-m.

In the same year (1998) the FARA system was used to acquire measurements at the Fraser mine site at a frequency of 625 kHz. The survey panel was between holes FR42617 and FR42618, which are approximately 25-50 metres apart. The resistivity images were derived from the data and confirmed the presence of the sulphide ore shown as a highly attenuated zone in the image with a resistivity range of 100-1600 ohm-m (Figure 2-9). These low resistive zones correspond to the areas where sulphide mineralization has been identified in the drill core and displayed with black histograms (Stevens et al., 2000).

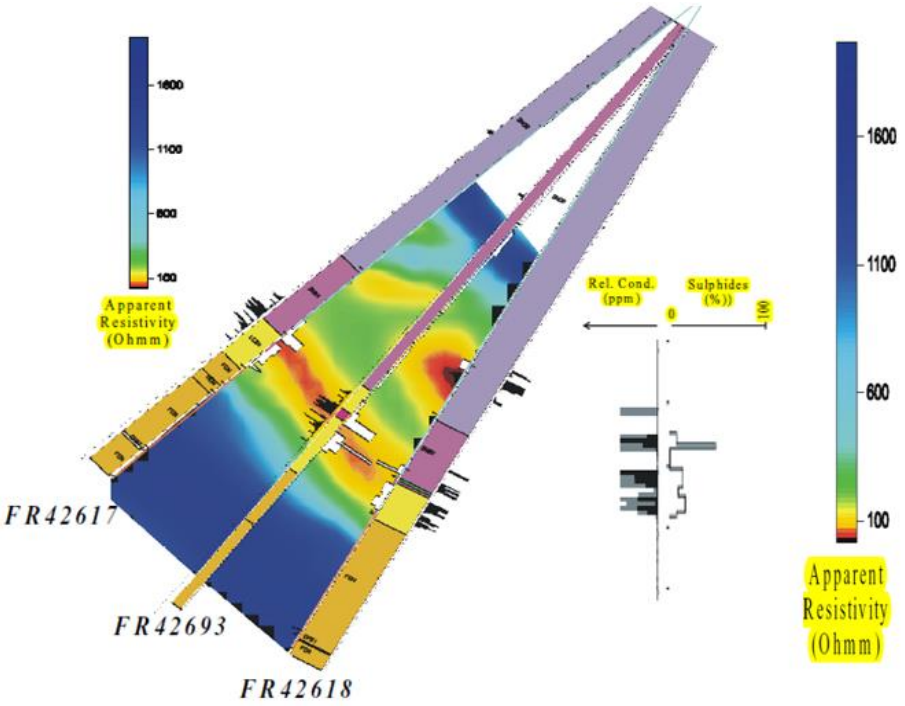

Figure 2-9: RIM image from 1998 using FARA-MF system at the Fraser Mine (Stevens et al., 2000).

The three studies discussed above demonstrate the effectiveness of the RIM method in the Sudbury Basin for detecting and delineating ore bodies and zones of elevated sulphide mineralization as well as tracing contacts between of rocks with contrasting conductivities. The tomographic images obtained from each site are in good agreement with other geophysical methods, in particular with the physical properties logs, the geological data available and with the test drilling results (Stevens et al., 2000).

2.5 Study location and thesis overview

This project summarizes the results of processing data from a radio imaging survey undertaken at MAC100G and MAC104, a pair of holes in the Nickel Rim South property. This property is located entirely within MacLennan Township, 22 kilometers northeast of the city of Sudbury (Figure 2-10).

The property is prospective for mineralization, lying across the eastern part of the Sudbury Igneous Complex close to the old mines at Falconbridge and the new Nickel Rim mine managed by Sudbury Integrated Nickel Operations. The two holes in this study contain mineralization and a better understanding of its extent and any controlling structures was sought from further geophysical surveys: e.g. borehole EM, down-hole geophysical logging and radio imaging surveys. The radio imaging survey is compiled, processed and interpreted in this study. The radio imaging equipment used to acquire the data was manufactured by the Russian company FARA and the data were acquired by Geofara acting on behalf of FARA Systems Canada. This is converted to a conductivity tomogram (S/m) and compared with the resistivity tomogram (ohm-m) generated using FARA's proprietary software. As well, the radio imaging tomograms will be compared with physical properties data derived from down-hole logs collected in both MAC104 and MAC100G holes.

Figure 2-10: Google map view of MacLennan Township (Google Maps, 2013). The symbol 'A' represents the township location.

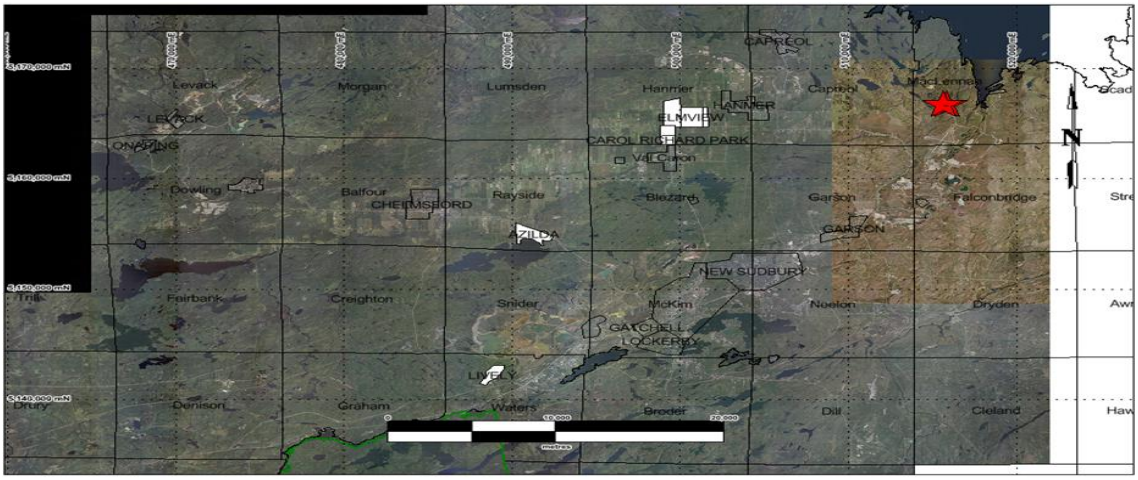

Figure 2-11: Regional locations of MAC100G and MAC104. Townships are indicated with an outline and the surveyed area is marked with a red star.

2.6 Objective of the research

The primary objective of this research is to investigate the feasibility and effectiveness of processing and interpreting the raw RIM data using the ImageWin software package with a goal to identify geological anomalies that may lead to the discovery or delineation of a mineral deposit.

A commercially available package, ImageWin (Fullagar, 2012), is used to construct an attenuation tomogram, from which it is possible to estimate the conductivity between boreholes. Accurate modeling of the propagation and diffusion of electromagnetic waves in geological media can be complex. However, simplifications can be made (e.g. assuming a straight ray path) to make calculations manageable (Korpisalo, 2005). The secondary objective of this study is to utilize the Geosoft and GOCAD mapping tools to visualize and compare the resulting tomograms of the RIM data constructed by ImageWin with those created by the FARA processing tool. The Imagewin results are compared with those derived from a proprietary package developed by FARA, which uses both the phase shift and the attenuation of the signal to derive the conductivity of the medium (Korpisalo et.al, 2008). It is assumed that the electrical properties are linear and independent of source strength and that the effect of dielectric permittivity is negligible (Korpisalo et.al, 2008). The tomograms derived from the two packages are discussed with respect to their consistency in locating geological anomalies and the estimated conductivity values. The

identified conductive zones are visualized in GOCAD software, which provides an enabling framework to map the geology information obtained from the RIM study.

The tertiary objective of this research work is to compare the results obtained from the two independent processing software packages, i.e. ImageWin and FARA, with the electrical properties of the rock (conductivity and magnetic susceptibility) measured with down-hole tools. This task is undertaken using the LogView tool, which allows a side-by-side comparison.

The final task is to investigate the procedure of calculating the conductivity values from the attenuation values output by the ImageWin software. These calculated conductivity values are compared with those that are exported from ImageWin and FARA.

3 RIM Raw Data Analysis

3.1 RIM raw data format and processing

The raw data generated in the RIM-FARA instrumentation is a proprietary-format file (*.far) which can be opened and read in the FarEdit software. From the FarEdit software, the raw RIM data can be exported in two different kinds of data sets, “Data average” where the data is averaged for each depth counter tick (*.dat) and “All data” (*.dat), which contains unaveraged data. The *.dat file (Figure 3-1) can be opened in Microsoft Notepad or other software programs, e.g. Golden Software Surfer.

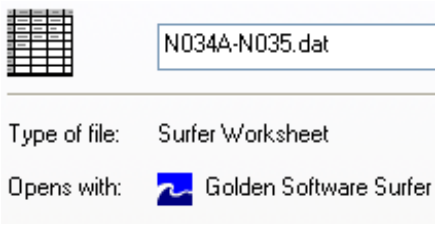

Figure 3-1: Example of .dat file used in this study.

The raw data were recorded using reciprocal locations of the transmitters and receivers. In the raw file, the column depth (1) represents the transmitter and receiver station’s locations in MAC104 where the transmitters were located at depths between 1100 and 1780 meters and the receivers were located at a depth ranging from 831 to 1516 meters. The column depth (2) shows the transmitter and receiver station’s locations in MAC100G where the transmitters were located

at depths between 1180 and 1820 meters and the receivers were located at a depth of 900 to 1355 meters.

The average for every counter tick (*.dat) file was then imported and plotted in Matlab. Figure 3-2 shows when the transmitters were in MAC104 and the receivers were located in MAC100G and Figure 3-3 shows the reciprocal set when the receivers are in MAC104 and the transmitters in MAC100G. The Y-axis represents the signal strength in counts and the X-axis represents the receiver depths in meters. Each curve represents a different transmitter location, with the largest signal generally being at a receiver depth that is generally most proximal to the transmitter in the other hole. From these plots it is possible to estimate the approximate depths of the attenuation zones using only the raw data, as will be demonstrated below.

Figure 3-2 shows amplitudes as large as 9000000 counts (normalized to the maximum voltage at the receiver antenna) when the receiver is between 1000 to 1400 meters. In the depth range of 1400 to 1430 meters, the amplitude values dropped significantly. Between 1430 to 1500 meters, the amplitude values showed a slight rise, and from the depth of 1500 to 1560 meters, the amplitude values decrease again. These results confirm the existence of material which strongly attenuates the emitting signal between the depth ranges of 1400 to 1430 meters as well as from 1500 to 1560 meters, i.e. close to MAC100G.

Figure 3-3 (receivers in MAC104) shows two zones that are associated with the high amplitude values: at depths between 1000 and 1320 m and 1520 and 1840 m. From the depth of 1320 to 1520 meters, the amplitude values dropped significantly, except for a slight increase in amplitude at the depth of around1400 m.

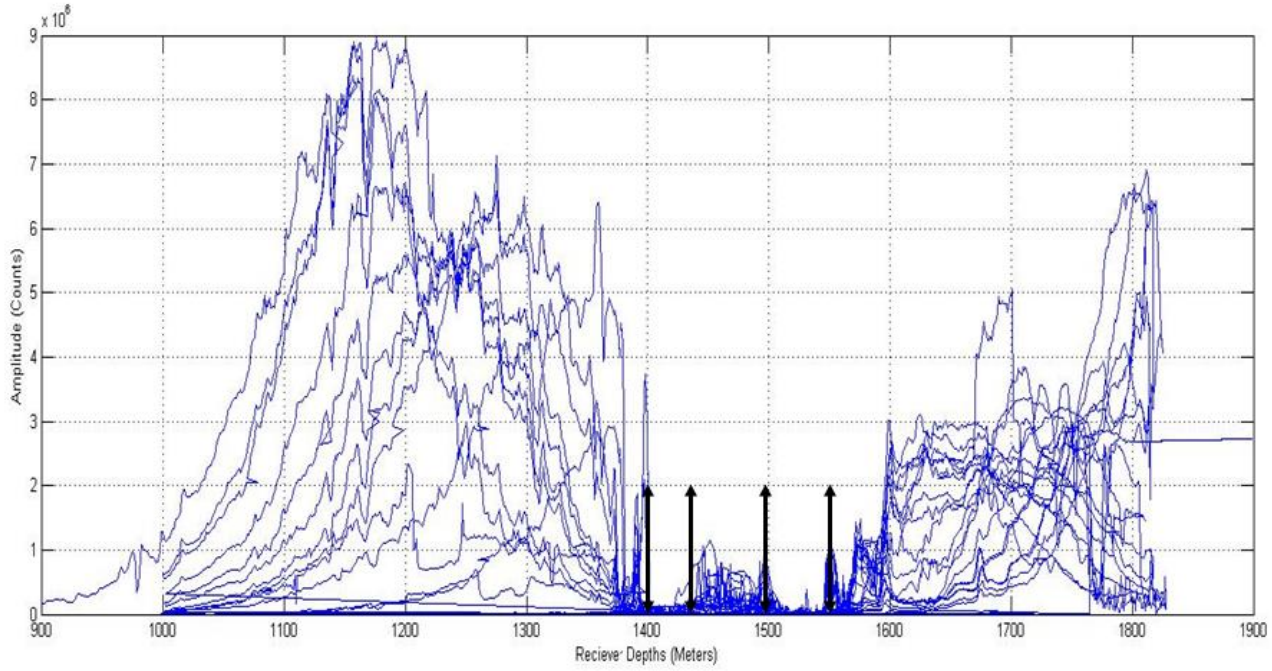

Figure 3-2: The amplitude data recorded when the receiver is at different depths in MAC100G. The zones between the two left arrows and the two right arrows show strong attenuation of signal as a result of the presence of highly conductive materials along the path between the transmitter and the receiver.

These results can be explained by the existence of two highly attenuated zones that are separated with slightly resistive material around 1400 m, making it therefore possible to differentiate the attenuating zones from the non-attenuating zone.

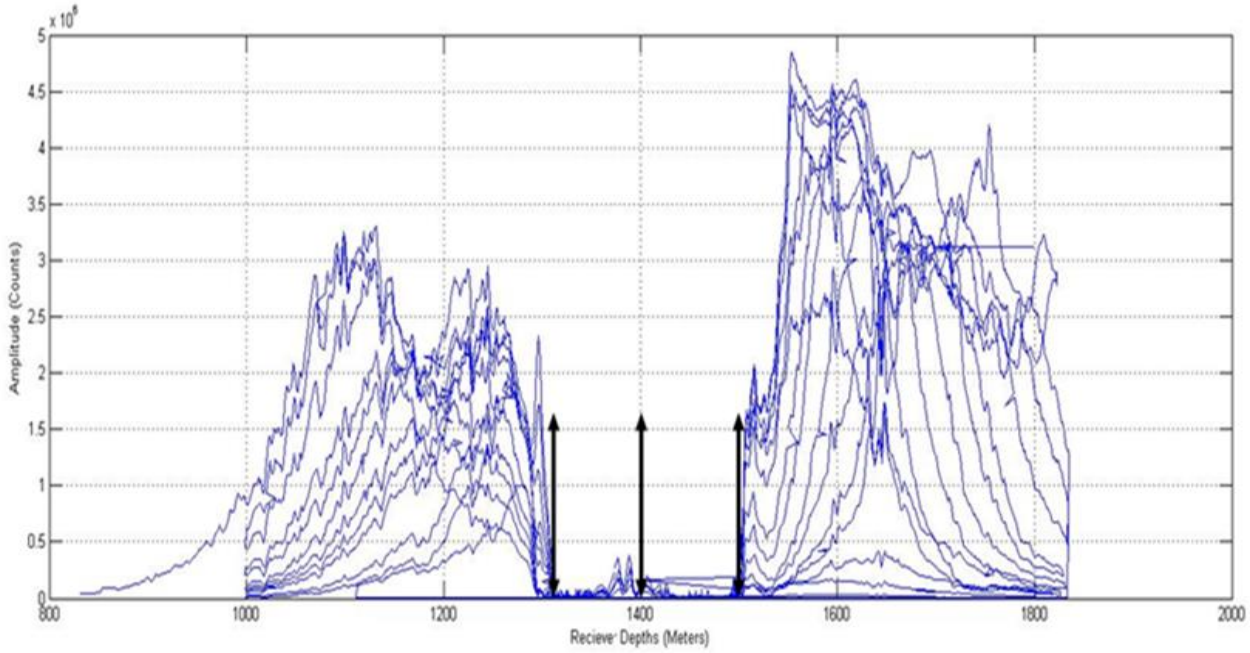

Figure 3-3: The amplitude data recorded when the receiver is at different depth in MAC104. There is attenuation between the left and right arrows, except for a slight increase close to the middle arrow.

3.2 Available raw data for borehole geometry, survey (depth, azimuth, dip) and collar (XYZ for the top of the holes)

The geometry of the holes was determined using the collar and survey files. The collar file contains the easting, northing and elevation of the top (collar) of the hole (NAD 27) in a UTM

grid. The coordinates of different locations down the holes can be inferred from measurements of the depth (distance down the hole) and the azimuth and dip at these depths. The latter information is contained in the survey file of the hole.

The azimuth angle is the compass orientation of the surface projection of a segment of the drillhole with respect to true geographic north (Figure 3-4.a and Figure 3-4.b). Dip is defined as an orientation or attitude of the hole relative to a horizontal plane and is given by numbers from 0˚-90˚ (Figure 3-4.a and Figure 3-4.b). The azimuth, dip and depth of different stations were measured using a compass that shows directions in a frame of reference relative to the surface of the earth.

The three components of the 'hole vector' are shown in Figure 3-4 a and b.

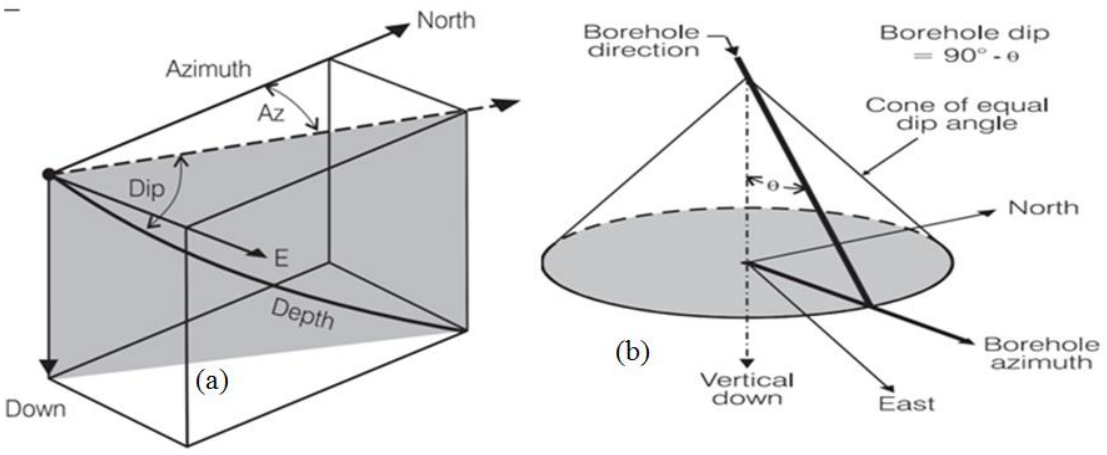

Figure 3-4: (a) Three components of the 'hole vector'; the dip, azimuth and depth. (b) The hole path may be in any direction on a cone of equal dip until the azimuth is also measured (Killeen and Elliott, 1987).

3.3 Introduction to ImageWin data processing package

ImageWin is a tomographic imaging package developed by the Center for Mining Technology and Equipment (CMTE) in Brisbane, Australia (Fullagar, 2012). This software is designed to plot tomograms using the coordinates of the transmitters and receivers. However, it should be noted that selecting different display modes allows the amplitude and the phase data to be plotted in other forms as well, e.g. by Tx or Rx gathers. Tomograms are derived from the amplitude and phase data for each frequency of acquisition. Four different algorithms can be used for tomographic reconstruction: ART (Algebraic Reconstruction technique), SIRT (Simultaneous Iterative Reconstruction Technique), LSQR (Least squares algorithm) and CGLS (Conjugate gradient for least squares problem) (Fullagar, 2012).

The program first applies different corrections to the amplitude values (reduction) and then calculates the attenuation from the corrected amplitude values. The images can be easily exported from ImageWin in XYZ file format. These files contain the slowness/velocity and conductivity values with respect to the XYZ location, where the XYZ coordinates system is that used for the location of the borehole collar. This file can be used to detect the location of the conductive zones and their associated conductivity values.

3.4 Data input for ImageWin

The ImageWin data file is generated from the raw FARA data file and the collar and survey file. The FARA file contains the measurement locations defined in terms of depth down-hole. The collar and survey file are used to locate these measurements in the X, Y and Z coordinate system (generally, easting, northing and depth). A sample drill hole survey file is shown in Appendix A.

Practically, the input file is prepared using two computer programs namely SURVEY and XYZsrv, developed by Dr. Peter Fullagar. First the SURVEY program was run on the survey data for both holes to determine the XYZ data (3D geometry) of the holes; second these geometry data were used by the XYZsrv program, in combination with the FARA data file to generate the ray-path file. The detailed instructions are given in Appendix B.

During FARA data acquisition, data were collected in "Tx gathers", i.e. with transmitter stationary and with receiver moving, and then the transmitter location is changed and the receiver is again moved in the adjacent hole. The transmitters and receivers were swapped from one hole to the other about half way through the survey, but both reciprocal data sets were included in the one file. In order to import the raw data into the ImageWin software, it is necessary to separate the data into two subsets: (Tx =MAC104, Rx=MAC100G and Tx =MAC100G, Rx=MAC104), representing the two reciprocal data sets that have Tx gathers from the two holes. The reason for this is that the XYZsrv program is set up to accept all the data from the transmitter gathers

obtained from one hole independently; the transmitter gathers from the other hole must be input separately. This results in a data set that can be more easily quality controlled as the depth in one (transmitter) hole was fixed for many records in succession while the depth in the other (receiver) hole varied. Finally, two files were generated for each frequency, i.e. 625 kHz and 1250 kHz. The two subsets were examined separately, i.e. (Tx=MAC100G, Rx=MAC104) and (Tx=MAC104, Rx=MAC100G).

The results obtained when importing the file without splitting the data into the two reciprocal data sets are discussed in Appendix C.

3.5 Converting data to dB

The signal strength can be defined in units of power (W), voltage (V), or decibels (dB), so the intention was to convert the data in counts to volts or dB so that it can be further processed. The dB is conveniently used to measure the sound level, but it is also widely used in electronics, signal and communication (Bureau International des Poids et Mesures (BIPM), 2006). It is a logarithmic unit used to describe a ratio of two quantities which is typically a power, but can be a sound pressure, voltage, intensity or several other things. In this case there are two signal strengths involved; the first is the signal strength from the dipole transmitter that emits an electromagnetic energy with power P1, and another is the signal strength from the dipole receiver

that records a reduced electromagnetic energy with power P2. The difference in decibels between the two powers was calculated using the formula (BIPM, 2006):

$$\mathbf{10 \log_{10} \frac{P_1}{P_2}} \qquad \textbf{(3-1)}$$

This conversion can be applied using the following command window in ImageWin Figure 3-5

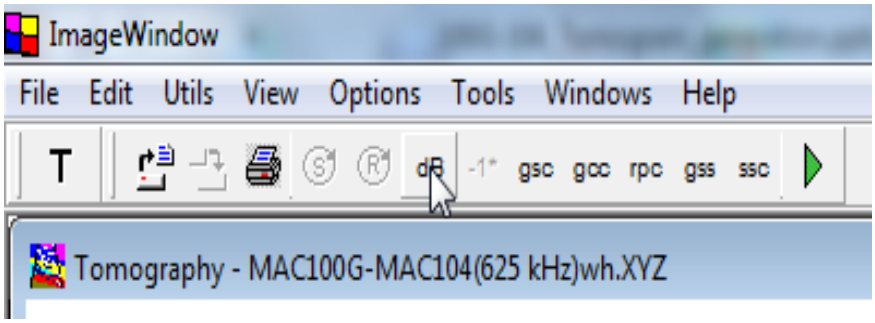

Figure 3-5: Demonstration of data conversion from counts to dB in ImageWin.

The bel and decibel, B and dB, where 1 dB =10 bel, are used to express the values of logarithmic ratio of power whose numerical values are based on the decadic logarithm, $l_g = \log_{10}$, so that dB = 10 $\log_{10}$ (P/P_0) and bel=$\log_{10}(P/P_0)$. The Neper is like the bel, but based on the natural log, so that Np=$\log_e(H/H_0)$ and the values H_i are field amplitudes or potentials, not normally powers P_i. (BIPM, 2006).The neper, bel and decibel units were recognized by BIPM for use with the International System, but they are not considered as SI units. Although it will be explained in more detail in the next chapters, it is worth mentioning that the data in dB/m should be converted to neper/m in order to calculate resistivity values based on the formula derived from Maxwell's

equations. The bel, decibel and Neper units are dimensionless and are used to convey information on the relative size of the quantities concerned.

3.6 Amplitude reduction

Amplitude reduction is performed before tomographic reconstruction. The tomographic reconstruction allows the user to estimate the absorption coefficient and hence the physical properties that might allow the user to infer the geology.

After the conversion to dB (discussed above), the amplitude data must undergo the following processes: (1) correction for geometrical spreading; (2) correction for the radiation pattern of the transmitter; (3) correction for the angular sensitivity of the receiver; and (4) accounting for the strength of the source. All the corrections assume the waves are propagating in the far-field regime. The electric far-field amplitude (A) for an ideal electric dipole transmitter and receiver can be calculated using (Fullagar et al., 1996):

$$\boldsymbol{A = A_0 \frac{\sin\theta_T \sin\theta_R}{r} e^{-\alpha r}} \qquad \textbf{(3-2)}$$

where A_0 defines the frequency dependent source strength; r is the length of the straight-ray path from transmitter to receiver known as the ray length; $\sin(\theta)_T$ defines the radiation pattern for the dipole transmitter; $\sin(\theta_R)$ is the receiver radiation pattern and α is the absorption coefficient along the ray path.

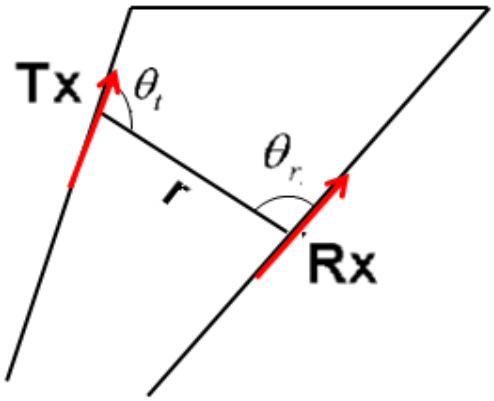

Figure 3-6: Simplified schematic of the ray polar angles at the transmitter and receiver.

The angles θ_T and θ_R are defined as the polar angles of the ray path with respect to the axis of the dipole transmitter and the dipole receiver antenna axes respectively (Figure 3-6) The factor 1/r accounts for the geometrical spreading of the far-field wave in a homogeneous medium.

The equation (3.2) is a non-linear exponential equation with respect to the absorption coefficient; taking the log of both sides linearizes the equation with respect to absorption coefficient (Pears and Fullagar, 1998):

$$\boldsymbol{\alpha r} = \boldsymbol{\tau} = \boldsymbol{a_0} - \boldsymbol{a} - \mathbf{20}\log_{10}\frac{r}{\sin\theta_T \sin\theta_R} \qquad \textbf{(3-3)}$$

In this formula, a is the log recorded field amplitude in dB, a_0 is the log source strength.

RIM amplitude strength at any particular station is sensitive to the distance between the transmitter and the receiver. This means the geometry of the boreholes used for the survey plays

an important role and can significantly impact the measured amplitude. It is important that survey is designed in a way to achieve good results. However, even with a very careful design the user shall be aware of the potential errors and the resulting impact this has on the results. The distance between the transmitter and the receiver can be calculated from the information in the input file. The absorption due to the waves travelling this distance can be accounted for by assuming spherical or cylindrical spreading. The former would be most suitable if the transmitter dipole is small relative to *r*, the latter if the dipole length is relatively large. The corrections are:

$Amplitude + 20 \log_{10}(r)$ [for spherical geometry spreading].

Or

$Amplitude + 10 \log_{10}(r)$ [for cylindrical geometry spreading].

The ImageWin buttons for these conversions are shown below (Figure 3-7) in which "gsc" stands for geometry spherical correction and "gcc" stands for geometry cylindrical correction.

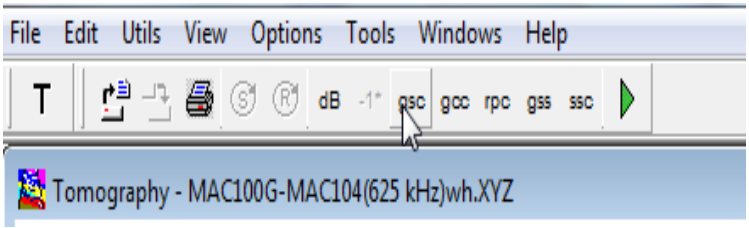

Figure 3-7: ImageWin window of the geometrical spherical correction (gsc). The button to the right is for the geometrical cylindrical correction (gcc).

The angles between the dipole axes of the transmitter and receiver respectively cause changes in the amplitude data, so the radiation pattern correction should be done by subtracting the term $20\log_{10}(|\sin\theta_T \sin\theta_R|)$. This gives the fourth correction:

$$\boldsymbol{Amplitude - 20\log_{10}(|\sin\theta_T \sin\theta_R|)}$$ [radiation pattern correction].

where the amplitude is in dB, $\sin\theta_T$ represents the radiation pattern for the dipole transmitter, $\sin\theta_R$ represents the receiver sensitivity function. The button for this conversion is rpc, which stands for radiation pattern correction (Figure 3-8).

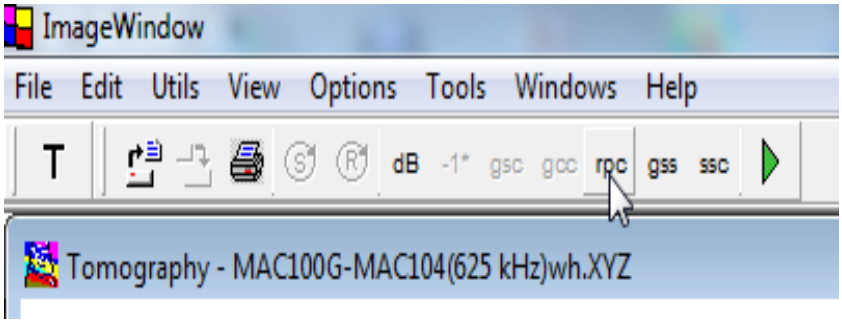

Figure 3-8: ImageWin window of the radiation pattern correction (rpc).

"gss" and "ssc" buttons on Figure 3-8, are global source strength and source strength correction, respectively. When choosing the "gss" option the software asks for the global source strength, the default value being calculated by the software, for the example data set being processed this default value is 158.3 dB (Figure 3-9). If the ImageWin user is not happy with this global value, a local strength can be selected, but this option was not selected in this study.

Figure 3-9: Global source strength window.

The "ssc" applies the correction on source strength (Figure 3-10.a) through several iterations. The final value of the source strength used in the study is displayed in Figure 3-10.b. Prior to construction of tomograms, a window should pop up showing ray paths with negative attenuation values that have been rejected (Figure 3-11). If there are too many of these, then the reduction process has not worked well.

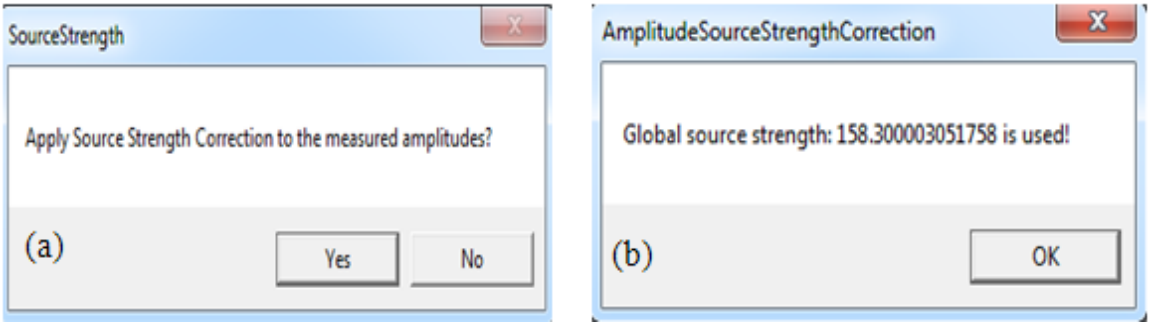

Figure 3-10: (a) Apply source strength correction window. (b) Final value of source strength window.

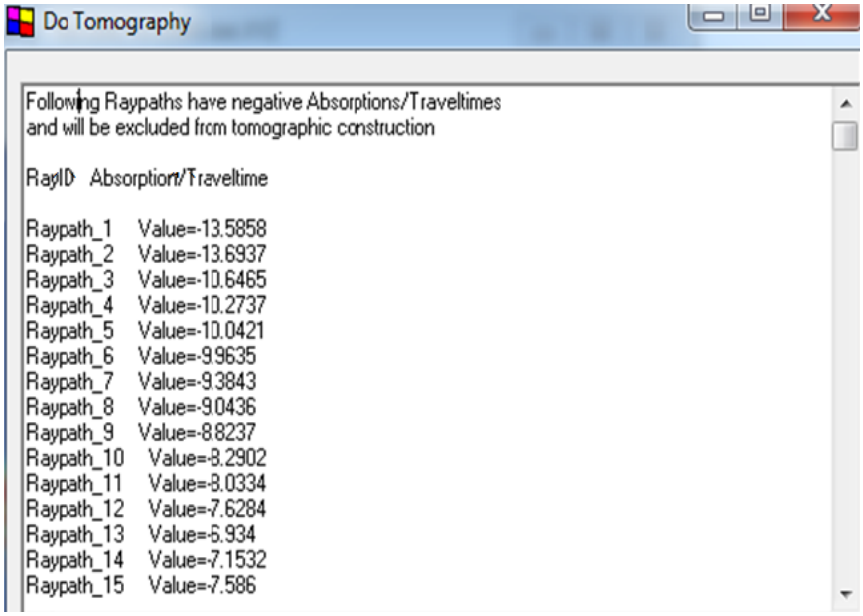

Figure 3-11: The tomographic inversion result of the RIM test. The first column (a) is the raypath numbers and the second column (b) is the rejected negative absorption value.

The software vendor (Dr. Peter Fullagar) has commented that the "source strength" value is not always reliable, particularly as it can vary significantly from transmitter location to transmitter location. A different value could give different resistivity results. The value of 158.6 was used for the source strength in this study, but processing the raw data again with different "source strength" values was not examined in this project.

3.7 Ray masking (using angle, amplitude)

Importing the amplitude and phase of the RIM data in ImageWin and then using the ray-masking facility makes it possible to detect conductive zones, specifically the number of zones and the approximate locations of these zones. However, now the locations of the attenuating conductive zones can be extrapolated away from the holes. Ray masking was applied by varying thresholds for the amplitude and angle of the ray in this project. These masks were applied to the amplitude and ray angle separately to identify the ray paths that are associated with strong attenuation.

Different modes of masking are available for masking out the rays: low cut or high cut (Fullagar, 2012, ImageWin Help). A low-cut mask selects for rejection (or masking) all the amplitudes (or ray angles) with values lower than the cut-off value, while a high-cut mask chooses all the rays with angles higher than the cut-off value. The high absorption regions can be identified by masking out the low-cut amplitude values as this will identify all the rays that have been attenuated and have low amplitude values (Fullagar, 2012, ImageWin Help). Depending on the chosen value for the low cut, a different number of rejected rays are displayed using a green line. In the following sections, the low-cut was varied for amplitude masking and the low-cut and high-cut values were varied for ray angle masking.

Figure 3-12 shows the ray angles for one transmitter position and two receiver antenna positions. The ray angle is measured from a line parallel to the borehole.

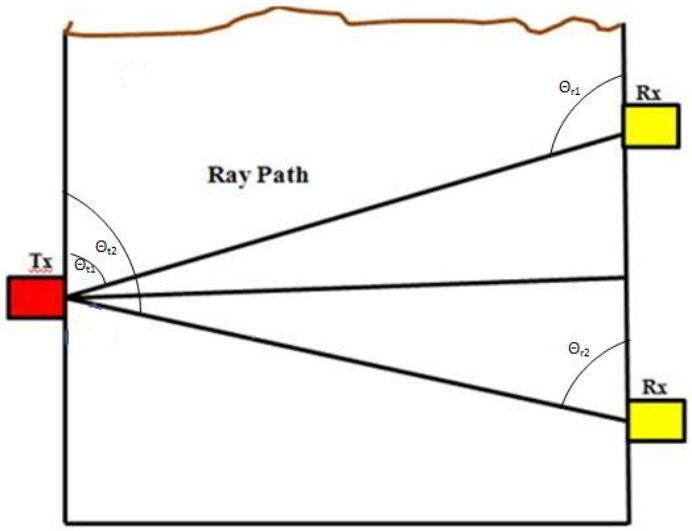

Figure 3-12: Ray angle demonstration.

3.7.1 Ray masking on reduced amplitude data for Rx= MAC104, Tx=MAC100G

In this section the data sets are masked out on reduced amplitude data (using a variety of values) with no ray angle masking. It is worthwhile to mention that the amplitude reduction removes the attenuation due to the ray-path being longer, so the only significant cause of attenuation is the presence of conductive material.

Figure 3-13 shows the "Ray Mask Setup" window for the first data set (Rx=MAC104, Tx =MAC100G). The box on the left is the amplitude masking, which shows the minimum and maximum amplitude rays in the data set (61.5784 to 183.717). The selected cut-off values can be

between these two values. The right box is the ray angle masking box – there has been no ray angle masking in this first example.

Five different values between the minimum and maximum were selected to investigate the most appropriate value for optimal visualization of the attenuated zones. Figure 3-14.a which uses a low cut of 61.58 shows no attenuated zone, as expected because there is no rays with amplitudes less than this. Using a low-cut value of 90 dB (Figure 3-14.b) shows two zones with attenuated rays that are a distance of about 100 m apart from each other next to MAC100G.

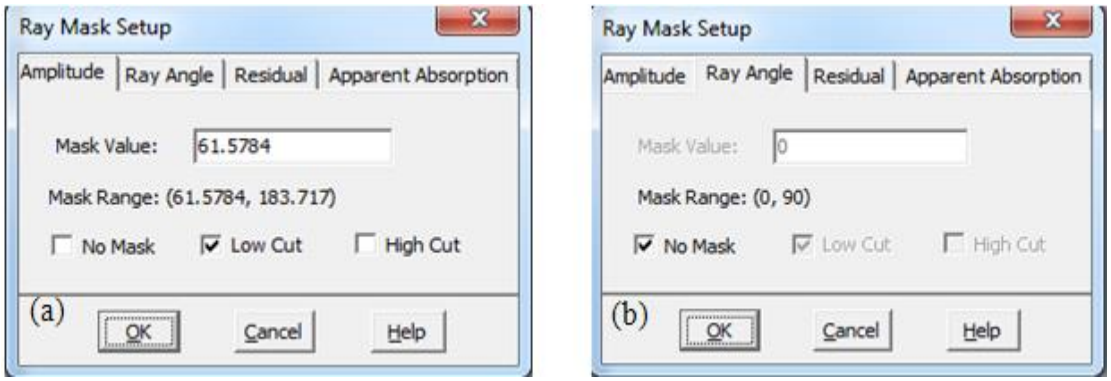

Figure 3-13: (a) Amplitude and (b) Ray Angle window under ray mask set-up for Rx=MAC104, Tx=MAC100G.

Figure 3-14.c shows the results obtained by using the low-cut reduced amplitude of 100 dB there are a lot more rays, and this makes the attenuated zones harder to see. Figure 3-14.d and Figure 3-14.e when the low-cut value of the reduced amplitude was chosen to be 120 and 183 dB, no specific zones can be identified as the area between Tx and Rx are fully covered (in green) with a

great number of masked rays. From these examples, it seems that the low cut of 90 allows the user to identify the approximate locations of the zones between holes. Further experiments could be done to see if values between 90 and 61 provide a better picture.

The method of plotting amplitude down the hole (Figure 3-2 and Figure 3-3) allowed the user to identify the attenuation zones in terms of depths down the hole. This method allows the user to identify where the zones might be between the holes.

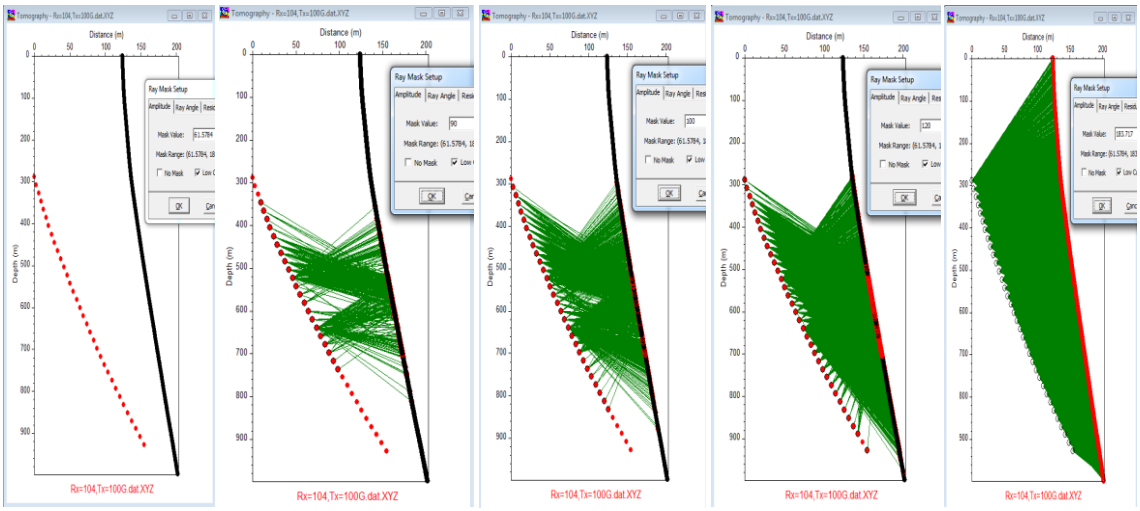

(a) (b) (c) (d) (e)

Figure 3-14: (a) The reduced low-cut amplitude=61.58. (b) The reduced low-cut amplitude=90. (c) The reduced low-cut amplitude=100. (d) The reduced low-cut amplitude=120. (e) The reduced low-cut amplitude=183.717.

3.7.2 Ray masking on reduced amplitude data for Rx= MAC100G, Tx=MAC104

The reciprocal data set (Rx= MAC100G, Tx=MAC104) were also masked using reduced amplitude data with no ray angle masking (Figure 3-15).

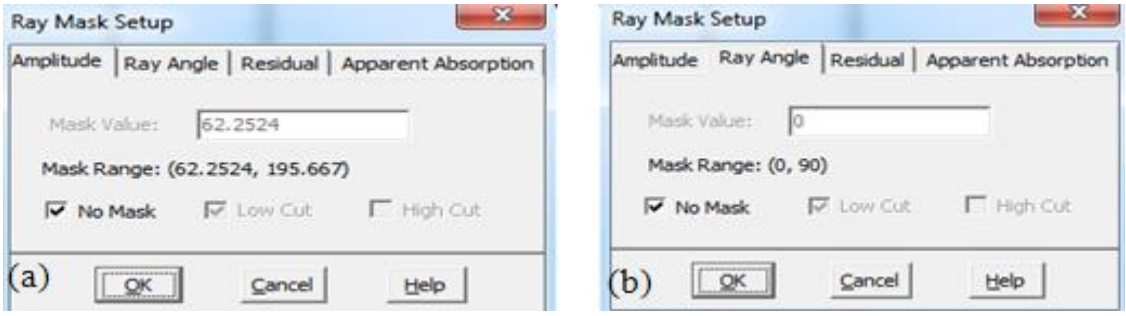

Figure 3-15: (a) Amplitude and (b) Ray Angle window under ray mask set-up for Rx=MAC100G, Tx=MAC104.

Applying the low-cut amplitude values of 62, 90, 100, 120 and 195dB, the changes in the number of deleted rays (the rays that are associated with the amplitude values that are less than the cut-off value) were investigated in order to find the attenuated zones. Figure 3-16.a (cut off of 62) shows no attenuated zones, as expected. Figure 3-16.b (low cut of 90) shows two attenuated zones about 200 m apart from each other next to MAC104. Figure 3-16.c, Figure 3-16.d and Figure 3-16.e shows the rays that have amplitudes below the cut offs of 100, 120 and 195 respectively. From the values tested, a low cut of 90 seems best, but further experimentation with values more or less than 90 might reveal more about the attenuating zone.

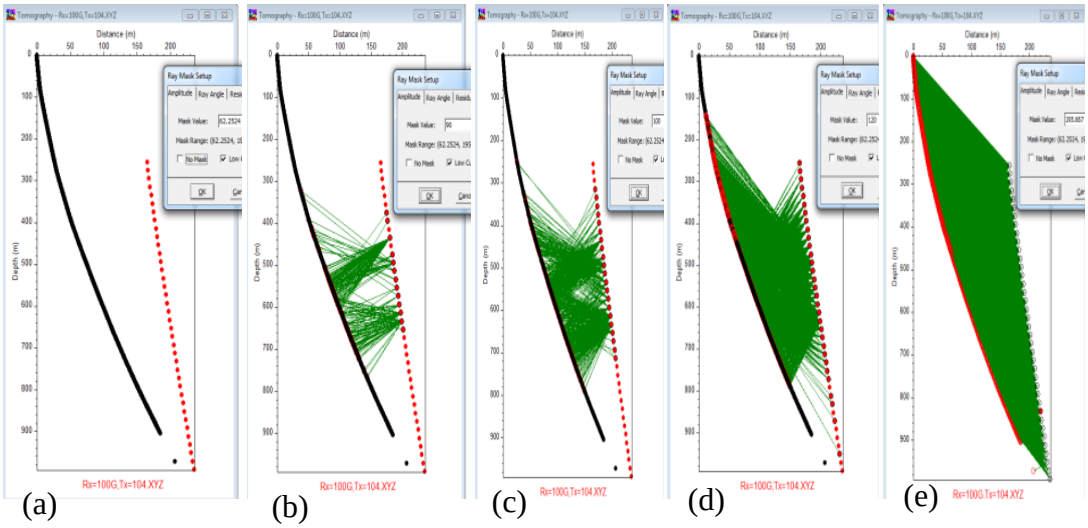

Figure 3-16: (a) The reduced low-cut amplitude=62.2524. (b) The reduced low-cut amplitude=90. (c) The reduced low-cut amplitude=100. (d) The reduced low-cut amplitude=120. (e) The reduced low-cut amplitude=195.667.

3.7.3 Ray masking on ray angle

In this section the impact of varying the value of the mask for the ray angles is investigated. This was tested with no amplitude masking using the Rx= MAC104, Tx=MAC100G data set.

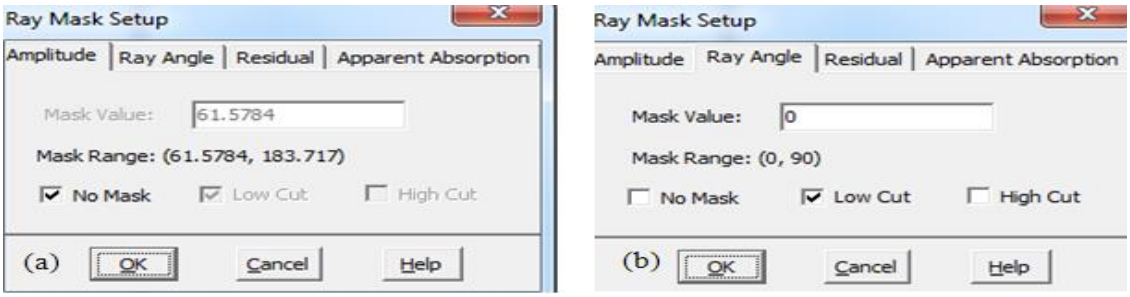

Figure 3-17: (a) Amplitude and (b) Ray Angle window under ray mask setup for Rx=MAC100G, Tx=MAC104.

Three masks for the ray angles were selected in order to evaluate how much geology can be inferred from the images. For the low-cut ray angle, the values of 0, 15 and 45 degrees and for the high-cut the values of 45, 85 and 90 degrees were chosen using no amplitude masking.

Figure 3-18.a (low cut 0 degrees) shows no rays removed. The low-cut angle of 15 degrees shows a number of rays at angles less than 15 degrees that have been plotted in green (Figure 3-18.b).

Setting the low-cut ray angle value to 45 degrees highlights a large number of rays (Figure 3-18.c). Selecting 45 degrees as a high-cut value, all the rays within the angle of more than 45 degrees will be deleted (Figure 3-19.a). In this case, the whole region is green. Figure 3-19.b shows the high-cut value of 85 degrees, which only highlights the rays that are approximately perpendicular to the holes, and the high-cut value of 90 shows no rays (Figure 3-19.c).

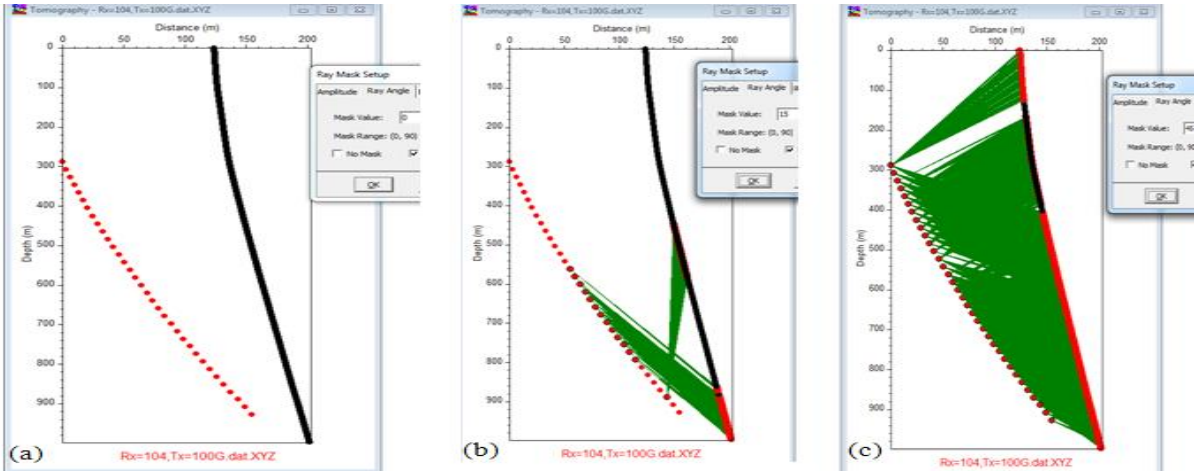

Figure 3-18: (a) The low cut ray angle of 0 degree. (b) the low cut ray angle of 15 degrees. (c) the low cut ray angle of 45 degrees.

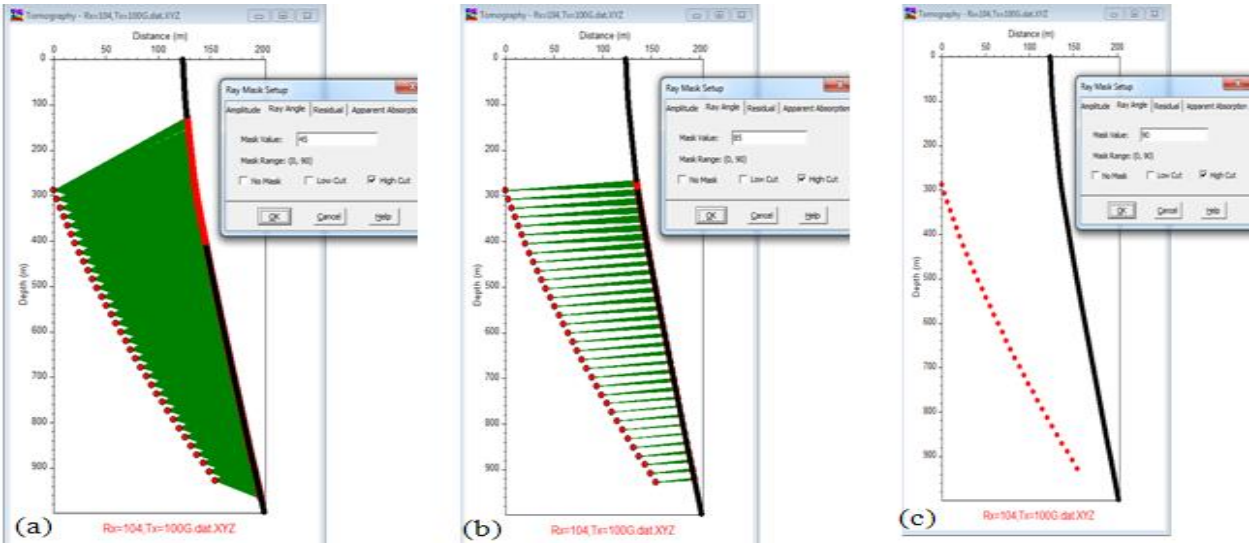

Figure 3-19: (a) The high-cut ray angle of 45 degrees. (b) the high-cut ray angle of 85 degrees. (c) the high-cut ray angle of 90 degrees.

The reciprocal data set shows very similar behaviour, so these results are not shown.

Using different ray angles, it is concluded that angle masking only really seems to give information about the angle of the rays, not the geology or locations of conductive zones. Perhaps this tool is useful for checking the ray paths that are included in the reduced data set, i.e. finding the location of the rejected rays listed in Figure 3-11. Essentially, ray masking is a tool that allows the user to examine the ray coverage effectively.

4 Impact of variables controlling tomography in ImageWin

In this section we examine the variables that control the tomography process in ImageWin. The constructed tomographic images can help to quantify the relative attenuation (conductivity) in all of the existent conductive zones.

The tomographic image is altered by selecting different values for variables available under the "tomography set up window" (Figure 4-1). These variables consist of those that define the "tomo areas", Vmin, Vmax, the choice of the type of the tomographic algorithm, the number of iterations, the starting velocity model and the weighting method. In this chapter, parameters were varied independently using ImageWin software to investigate the effects that each parameter has on the resultant attenuation tomogram.

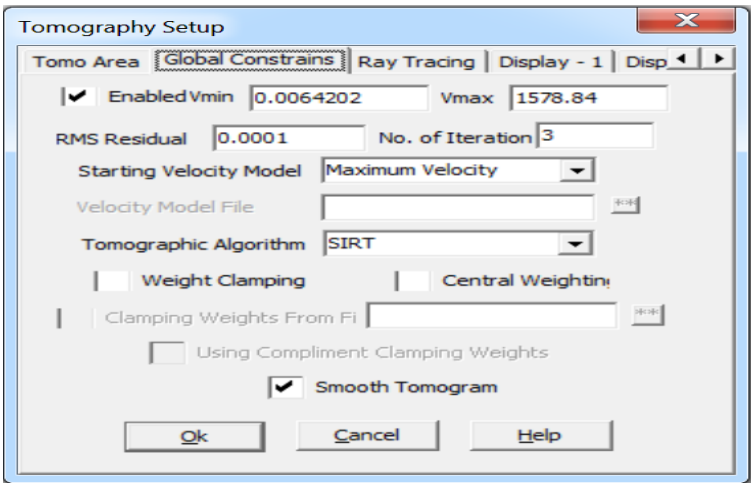

Figure 4-1: "Global constraint window" under "tomography set up window".

4.1 Sensitivity analysis for velocity range

The images displayed in ImageWin can be adjusted by restricting the displayed results to lying within a specific range of velocities. Velocity in this context is actually 1/absorption. ImageWin can also be used for seismic tomography, in which case “velocity” really is velocity. The values Vmin and Vmax determine the lower and upper limits of velocity. Restricting the velocity range is equivalent to restricting the absorption range. In the ImageWin program these values can be chosen by enabling the velocity check box. Otherwise, the default values are the minimum and maximum computed from the input data. For amplitude tomography, the Vmin and Vmax are specified as 1/ (Max Absorption) and 1/ (Min Absorption), respectively. It is possible to not apply these limits by unchecking the checkbox (Fullagar, 2012).

The primary aim of this section is to examine the effect on the displayed image of varying Vmin and Vmax. The results show that changing Vmin alters the conductivity range and appearance of the displayed image whereas altering Vmax values seems not to have a significant impact so it has been left constant at 16 m/dB. Vmin and Vmax are, in fact, upper and lower bounds that if augmented with other independent information and data about the physical properties of the rock such as conductivities of the host rock or the embedded conductive zones, they can provide more useful insights. If such information is not available, the Vmin and Vmax shall be chosen such that a good contrast with the underlying non-conductive host rocks can be attained.

The tomograms were created for four data sets (the two reciprocal data sets at two frequencies—625 and 1250 kHz). The impact on the displayed conductivities is examined.

4.1.1 Conductivity tomograms in 625 kHz for (Rx=MAC104, Tx=MAC100G) data set

The first tomogram (Figure 4-2.a) was constructed for the frequency of 625 kHz, in which transmitters were deployed in MAC100G and receivers were located in MAC104. In this part the comparisons are made between Figure 4-2.a, 4-2.b, 4-2.c and 4-2.d in order to analyze the changes using the same transmitter-receiver locations. These figures use Vmin values of 0.5, 2, 4 and 6 m/dB respectively, while keeping Vmax unchanged at 16 m/dB. The different images show a different range of conductivity values on the colour bar (Table 4-1). As Vmin increases, the range goes from being large 0.002 to 0.018 S/m (Figure 4-2.a) to being much smaller, from 0.0002 to 0.0012 S/m (Figure 4-2.d). The results obtained from this analysis demonstrate that the bigger the velocity range, the larger the range of the conductivity values since the velocity is proportional to 1/sqrt{conductivity}.

In terms of the appearance, the tomogram with smaller Vmin of 0.5 m/dB (Figure 4-2.a) is only showing red zones towards the transmitter location, while the tomogram with a bigger Vmin of 2 m/dB shows red zones at greater distance away from the transmitter (Figure 4-2.b). Care should be taken when interpreting the colour scales, for example the red in (a) is not the same as red in

(b), (c) or (d). Focusing on changes in the two zones of high attenuation in the tomograms (Figure 4-2.a), it becomes evident that the upper red zone has the highest conductivity of 0.018 S/m close to the transmitter locations in MAC100G whereas the second zone in the same tomogram shows a green color that is associated with low conductivity values of approximately 0.012 S/m. Increasing the value of Vmin to 2 m/dB makes a larger area red in both the upper and lower zones. On the other hand, having a small Vmin allows the user to discriminate between the highly conductive zones and the other more moderately conductive zones. In the tomogram with Vmin value of 2 m/dB (Figure 4-2.b), it is not apparent which zone – upper or lower – is more conductive.

In the third tomogram (Figure 4-2.c) with Vmin 4 m/dB, the attenuated zones appear saturated, the images are dominated by blue and red and do not show a significant amount of green or yellow. Further, the boundaries lie along straight ray paths. These straight edges are a direct outcome of the higher Vmin values. By increasing Vmin from 4 m/dB (Figure 4-2.c) to 6 m/dB (Figure 4-2.d), two attenuated zones are mixed a lot more in comparison to the appearance of Vmin=4 m/dB and the tomogram became much more saturated—there is essentially one large attenuated zone rather than two zones in the image (Figure 4-2.d). In other words, the tomogram with Vmin 6 m/dB is not capable of differentiating the strongly attenuated zones from the more weakly attenuated zones. This is especially to be expected if a high Vmin (low maximum

conductivity) is adopted. Also, the conductivity range is very small 0.0004- 0.00014(S/m) because a small range is demanded by choosing a large Vmin.

From the above comparison, Vmin values as low as 0.5 results in only seeing the most conductive zones, while high Vmin like 4 or 6 show a lower conductivity range and large highly saturated zones where is not possible to identify the locations of the most conductive zones. This investigation shows that some experimentation is required to adopt the best colour scale. In this case a value was selected consistent with the results of the raw amplitude graphs and ray masking facility which have shown two attenuated zones in between the holes. If the most conductive zone is required, then a very small value of Vmin is required. If the outline of the conductive zones is required, then Vmin should be increased. However, increasing it too much will result in saturation and little geological information. Essentially, in the absence any additional information about the physical properties of the rock it is sensible to adopt the default Vmin and Vmax.

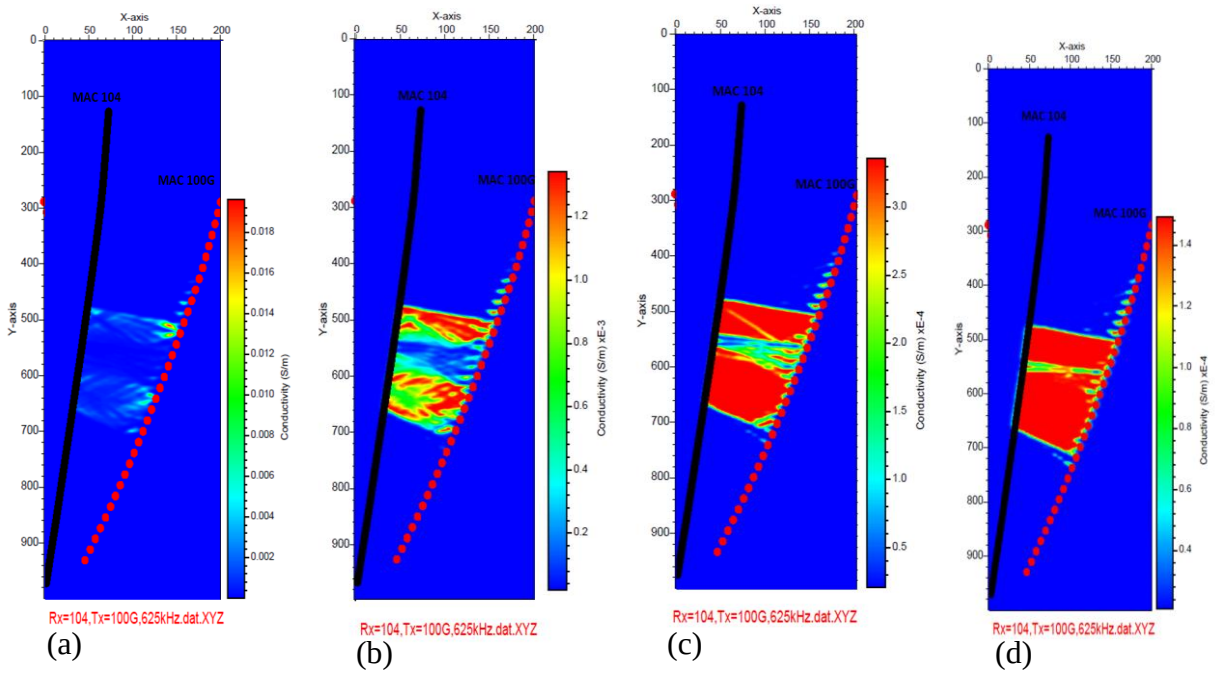

Figure 4-2: (a) Conductivity tomograms for 625 kHz data (a) Vmin=0.5 and Vmax=16. (b) Vmin=2 and Vmax=16. (c) Vmin=4 and Vmax=16. (d) Vmin=6 and Vmax=16. (The colour scales are different on the above tomograms).

Through using different Vmin and Vmax values the following points were noticed: 1) In terms of the conductivity, the lower the minimum velocity (Vmin) value, the higher the displayed conductivity that will be displayed in some zones. Note that the conductivity is not changing; only the colour with which a particular conductivity is being represented is changing. 2) The tomograms are somewhat different in terms of the coherency because the conductivity will saturate if Vmin is too high. 3) The tomograms with low Vmin values are spatially biased to the transmitter and tomograms with higher Vmin values show zones spread outwards from the transmitter. This can be attributed to the fact that the inversion has resulted in the very high

conductivity zones being located in the vicinity of the transmitter and if the amplitude to colour mapping is not set carefully, some zone will not be seen. 4) It was observed that the conductivity of the higher conductivity zones decreases with increased Vmin, which restricts the range of conductivity (Table 4-1).

Table 4-1: The summary of the velocity range and the associated conductivity range and the fit to the data for 2 iterations in 625 kHz.

Vmin- Vmax	**Conductivity min-Conductivity max**	**Fit to the data (RMS)**	
		1 iteration	**2 iterations**
0.5-16	0.002-0.018	18.4	18.3
2-16	0.0002-0.0012	18.52	18.45
4-16	0.-00005-0.0003	19.75	19.67
6-16	0.00004-0.00014	21.26	21.23

4.1.2 Conductivity tomograms at 1250 kHz for (Rx=MAC104, Tx=MAC100G)

The procedures of varying Vmin were applied to the 1250 kHz data set for (Rx=MAC104 and Tx=MAC100G) in order to compare the images. The resulting tomograms with different minimum velocity values are shown in Figure 4-3.a, b, c and d. The tomograms constructed at 1250 kHz are smoother than those constructed at 625 kHz while higher resolution would normally be expected at the higher frequencies, this is an issue that should be investigated in further studies, so the precise location of the zone boundaries are easier to identify at 625 kHz. This appears to be a characteristic of the difference in frequency. For both frequencies increasing Vmin results in the tomograms becoming more saturated.

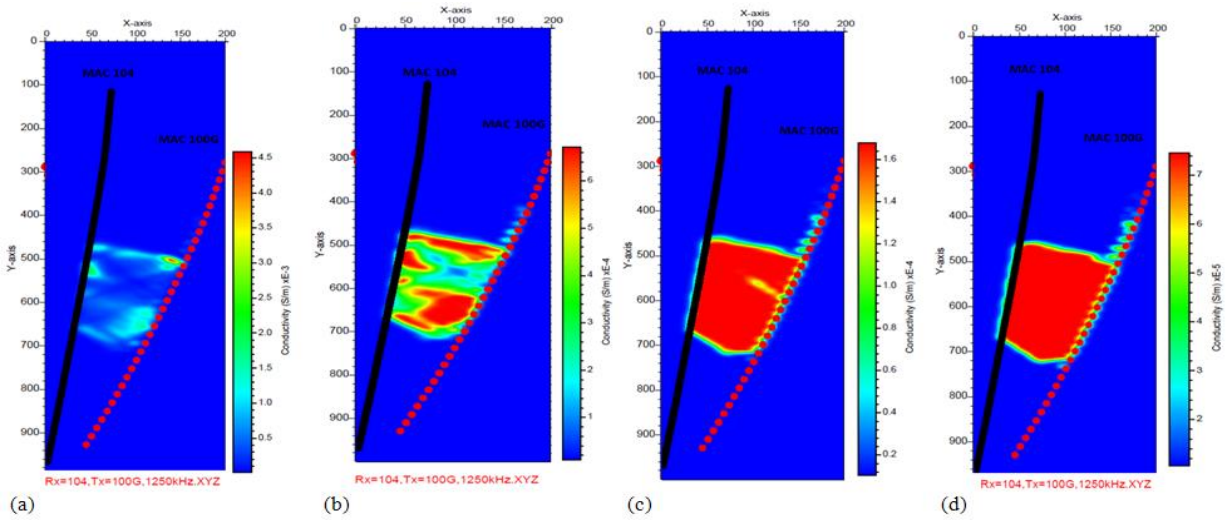

Figure 4-3: (a) Conductivity tomograms for 1250 kHz data (a) Vmin=0.5 and Vmax=16. (b) Vmin=2 and Vmax=16. (c) Vmin=4 and Vmax=16. (d) Vmin=8 and Vmax=16. (The colour scales are different on the above tomograms).

Table 4-2: Summary of the velocity range and the associated conductivity and the fit to the data for two iterations range in 1250 kHz.

Vmin- Vmax	Conductivity min-Conductivity max	Fit to the data (RMS)	
		1 iteration	2 iterations
0.5-16	0.00005-0.00045	21.69	21.54
2-16	0.0001-0.0006	21.69	21.54
4-16	0.00002-0.00016	21.69	21.57
6-16	0.00002-0.00007	21.91	21.88

Table 4-2 gives the conductivity range and the fit to the data associated with the specific Vmin and Vmax values in the frequency of 1250 kHz. As shown in Table 4-1 and Table 4-2, varying the frequency from 625 to 1250 kHz altered the conductivity range on the displayed images such that at the lower frequency, higher maximum conductivities were obtained. For instance, at Vmin=2 and Vmax=16, the maximum conductivity at 625 kHz is 0.0012 S/m and at 1250 kHz it

is 0.00035 S/m. This reduction for higher frequency is consistent for all different Vmin and Vmax values for the frequencies studied in this work. Such behaviour is to be expected if upper and lower bounds are imposed. Also, the use of a different frequency is expected to give a different conductivity model.

4.1.3 Conductivity tomograms in 625 kHz for (Rx=MAC100G, Tx=MAC104)

The reciprocal data set was imported into the ImageWin software and after reducing the amplitude data, different Vmin values were tested with a fixed value of Vmax at (16 m/s). First, the tomogram was created using Vmin 0.5, but the tomogram did not show two distinct zones. Varying the Vmin from 0.5 to 2 makes the two zones more apparent (Figure 4-4.a). However, this case shows strong bias with conductive zones close to the transmitter location. The upper and lower zones are evident, but unlike the cases discussed above, now the lower zone appears more conductive.

Figure 4-4.b shows the tomogram for the minimum velocity value of 4. The tomogram is noisy and the boundaries of the zones are not completely clear. High attenuated zones are biased to the transmitter location (MAC104). The lower zone is still showing more attenuation than the upper zone and the conductivity range is from 0.00005 to 0.00003 S/m. Figure 4-4.c with the Vmin value of 6 illustrates that the tomogram is still biased to the transmitter location with the

conductivity range of 0.000025-0.00008. Note that larger Vmin values have not resulted in strong saturation as was seen in the examples above.

For the reciprocal data set, the minimum and maximum velocities and the associated minimum and maximum conductivities are shown in Figure 4-4. The maximum conductivity decreased from 0.0012 to 0.00008 S/m with increasing Vmin from 2 to 6.

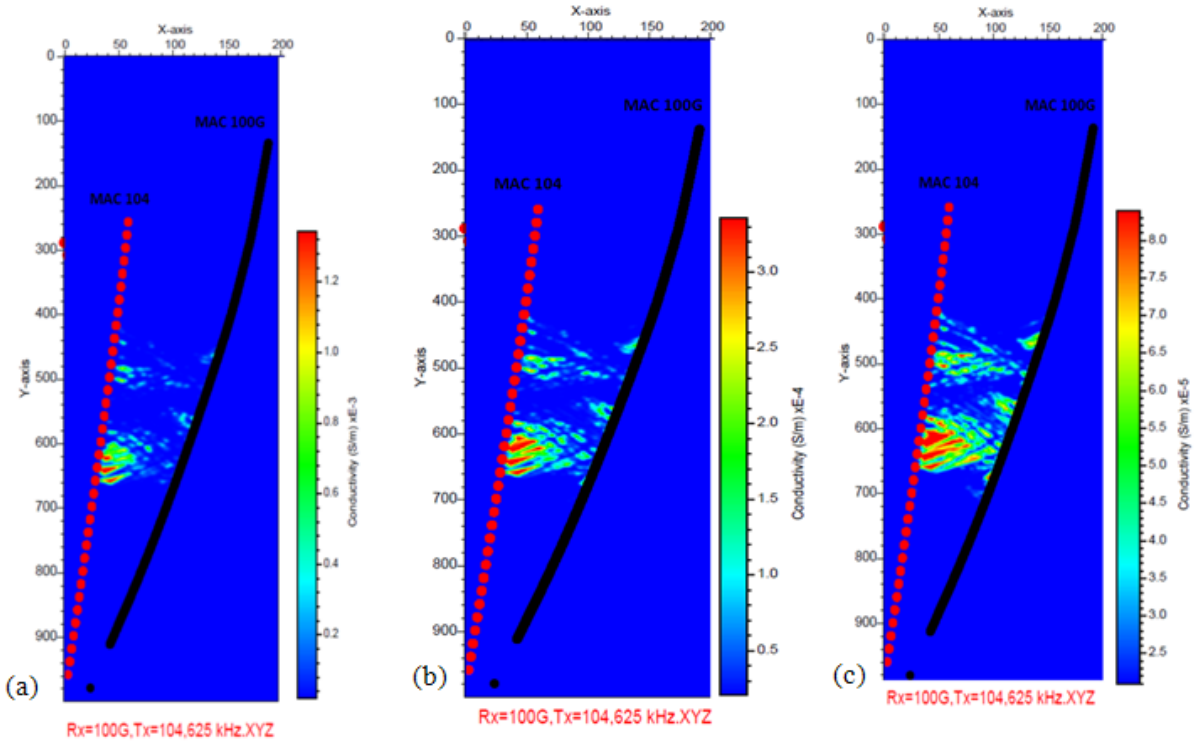

Figure 4-4: (a) Conductivity tomogram Vmin=2 and Vmax=16 for the 625 kHz data. (b) Vmin=4 and Vmax=16. (c) Vmin=6 and Vmax=16.

Table 4-3: Summary of the velocity range and the associated conductivity range and the fit to the data for two iterations in the 625 kHz image for Rx= MAC100G, Tx=MAC104.

Vmin-Vmax	Conductivity min-Conductivity max	Fit to the data (RMS)	
		1 iteration	2 iterations
2-16	0.0002-0.0012	25.75	25.44
4-16	0.00005-0.00003	25.82	25.66
6-16	0.000025-0.00008	26.13	26.09

4.1.4 Conductivity tomograms at 1250 kHz for (Rx=MAC100G, Tx=MAC104)

The tomograms were also constructed for the reciprocal data set (Rx=MAC100G and Tx=MAC104) at the higher frequency. The Vmin values were changed from 0.5 to 6 m/s while keeping the maximum velocity constant at 16 m/s. These higher frequency tomograms were also smoother in comparison to the tomograms constructed at the lower frequency. Figure 4-5.a shows

two highly attenuated zones 150 meter apart with Vmin=0.5 and Vmax=16 that also has the more conductive zones close to the transmitter in MAC104. The second tomogram with a Vmin value of 4 is better at depicting the zone further from the transmitter. Figure 4-5.c (Vmin=6 m/s) is not significantly different from Figure 4-5.b. As before, increasing Vmin shows an increase in the saturation level of the conductivity.

The velocity range and the associated conductivity range for two different frequencies of 625 and 1250 kHz are shown in Figure 4-3 and Figure 4-4. The behaviours are similar to that seen above. If the purpose of the images is to identify the spatial distribution of the upper and lower conductive zones, then for 625 kHz, the velocity range of 0.5-16 m/s gives the best results; however for 1250 kHz the range 4-16 m/s seems to give better results. This illustrates that in order to use Vmin as a parameter to adjust the colour bar, it is necessary to experiment with these parameters for each frequency and each reciprocal data set. The ImageWin program normally displays the hole that contains the transmitter with distinct red dots. In order to compare the reciprocal data sets, the images have been flipped so that hole MAC104 was arbitrarily to the left.

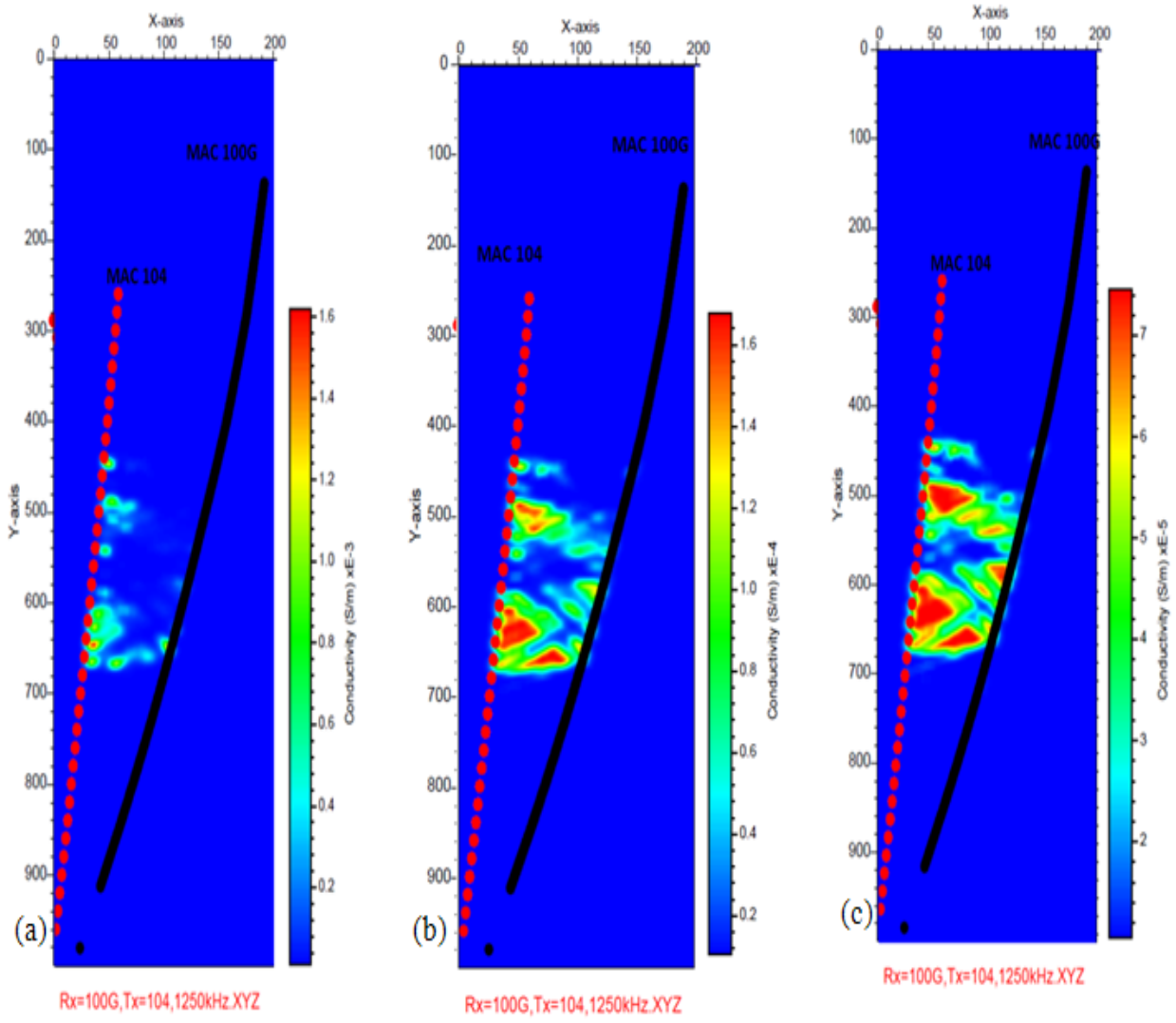

Figure 4-5: (a) Conductivity tomogram Vmin=0.5 and Vmax=16 in 1250 kHz. (b) Conductivity tomogram Vmin=4 and Vmax=16 in 1250 kHz. (c) Conductivity tomogram Vmin=6 and Vmax=16 in 1250 kHz.

Table 4-4: Minimum Velocity and the associated conductivity range with the fit to the data for Rx= MAC100G, Tx=MAC104 in 1250 kHz.

Vmin- Vmax	Conductivity range at 1250 kHz	Fit to the data (RMS)	
		1 iteration	2 iterations
0.5-16	0.0002-0.0016	21.69	21.54
2-16	0.00002-0.00016	21.38	21.35
4-16	0.00002-0.00016	21.69	21.57
6-16	0.00002-0.00007	21.91	21.88

4.1.5 Sensitivity analysis for Changing Tomo Areas

The "changing tomo areas" group under the tomography setup window contains the editing boxes which allow the user to specify the discretization of the tomographic area in the x- and y-directions. The default values are set by the program according to the input ray-path data. The

default values for the first data set (Rx=MAC104, Tx=MAC100G) is 113 cells in the x direction and 556 cells in the y. The result for this case is shown in Figure 4-7. Note that the images are now displayed so that hole MAC104 is on the right. For the reciprocal data set (Rx=MAC100G, Tx=MAC104) the defaults in the x and y directions are 143 and 599 respectively (Figure 4-6.a and b). The box labelled "Number of Cells" contains the variables that allow the user to define the number of grid cells in the x-and y-directions for tomographic imaging. As an experiment, the number of cells was modified for the first data set (Rx=MAC104 and Tx=MAC100G) in order to understand the impact.

The area is four times bigger in the y direction than the x direction, and thus five different combinations of (x, y) values for the number of cells was selected, specifically (40, 160), (80,320), (120, 480) and (150, 600) were input using the tomo area window (Figure 4-8.a and b). In Figure 4-8.a through Figure 4-8.c, the results are shown for Vmin, Vmax = (2, 16). The range of the conductivity values does not seem to be a strong function of the selected cell size.

Limiting the discretization of the tomographic area to 40 cells in the x- and 160 cells in the y-direction, gives a coarse tomogram, and the boundaries of the attenuated zones are not clear (Figure 4-8.a). Changing the number of cells to (80, 320), the edges of the attenuated zones are more clearly shown (Figure 4-8.b). Further increases in the number of cells to (120, 480), results in further improvements. A subsequent increase to (150, 600) would likely not give a further improvement and attempting this generated an error from the ImageWin code (Figure 4-9). This

was probably because the cell size is too small or the number of cells too large. The default values (Figure 4-7) seem to give results comparable to the best example in Figure 4-8.c, so there does not seem to be a requirement to experiment with these parameters. A smaller number of cells should be used to avoid error messages, or if faster run times are required. However, it should be noted that if the cell size is too small, some cells may not be crossed by any rays. So, it is important to determine the optimized cell size for any given survey.

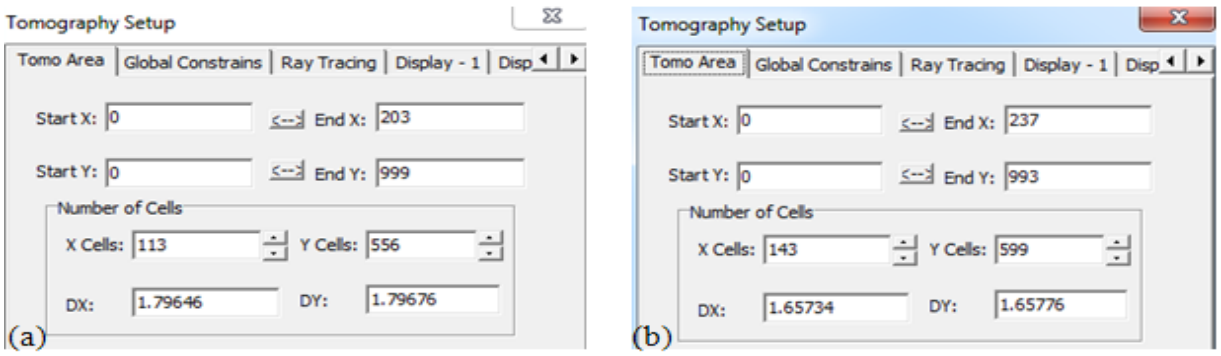

Figure 4-6: (a) Tomo area window for Rx=104,Tx=MAC100G with 113 number of x cells and 556 number of y cells. (b) Tomo area window for Rx=MAC100G,Tx=MAC104with 143 number of x cells and 599 number of y cells.

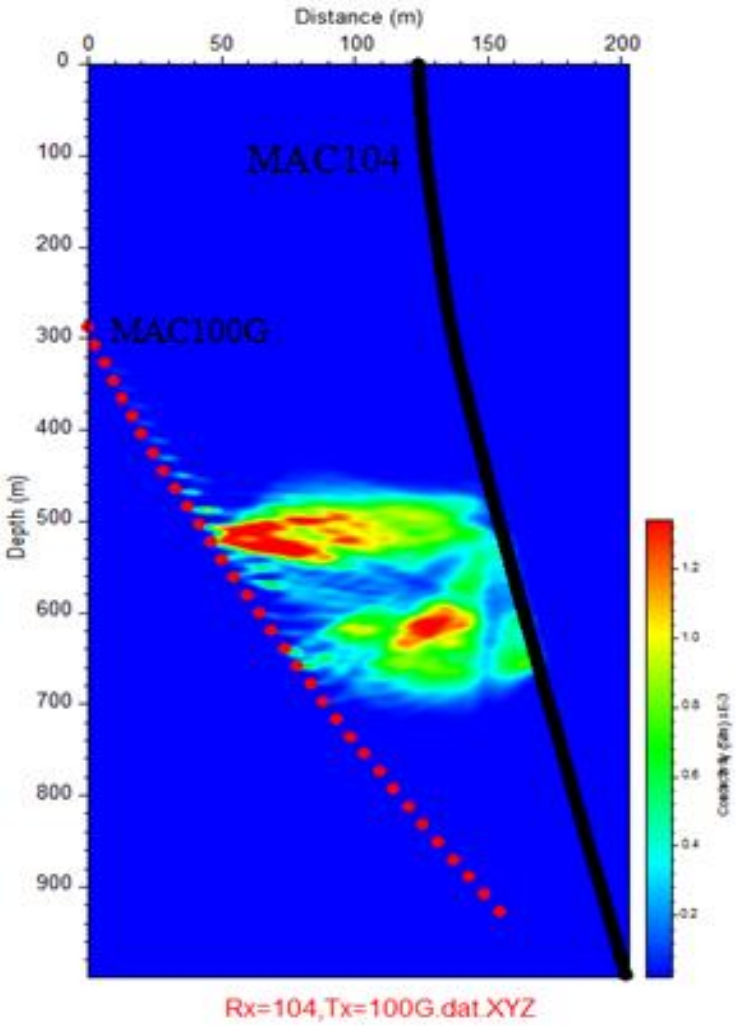

Figure 4-7: Tomo area of 113-556 (default values).

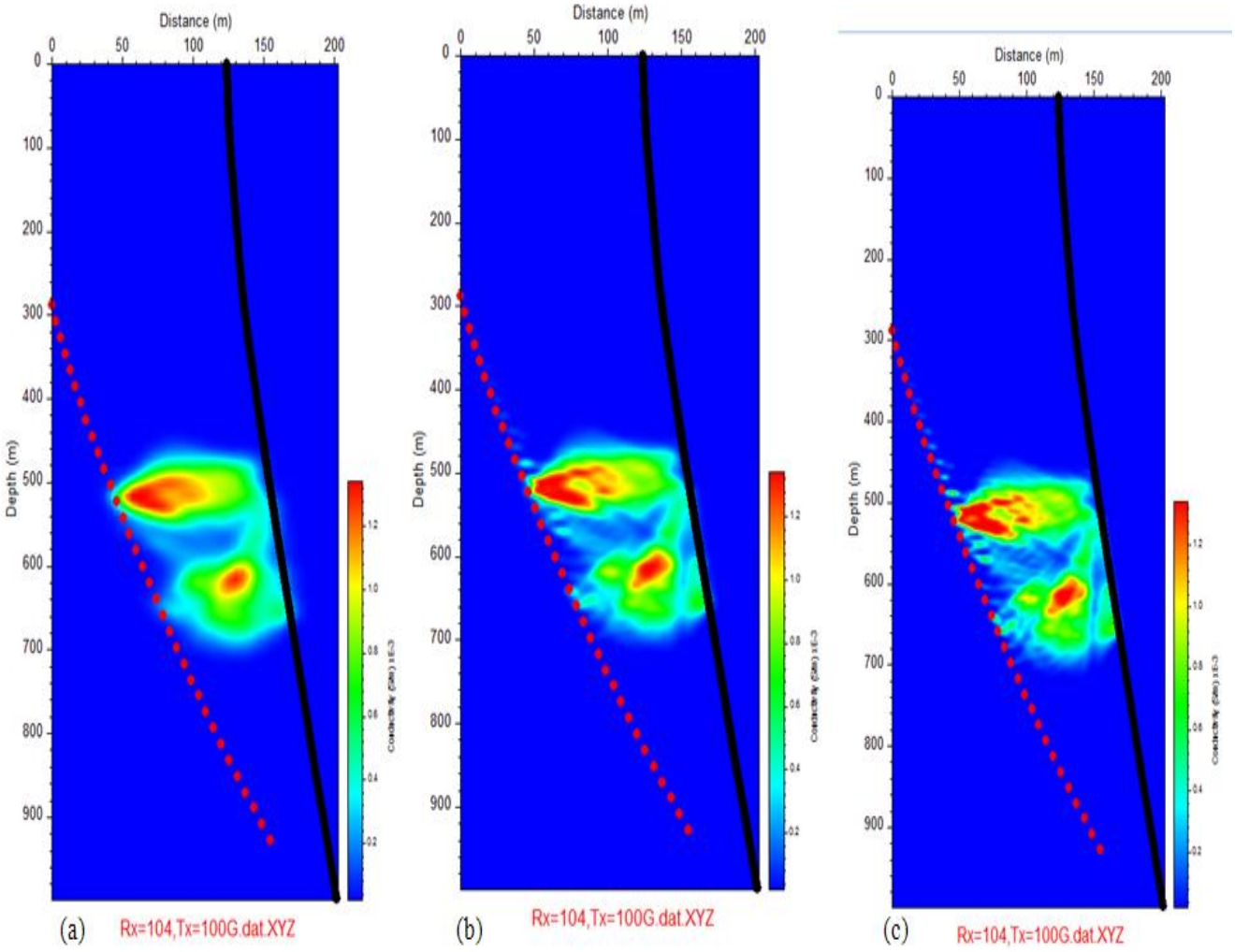

Figure 4-8: (a) Tomo area of 40x160 cells. (b) Tomo area of 80x320 cells. (c) Tomo area of 120x480 cells.

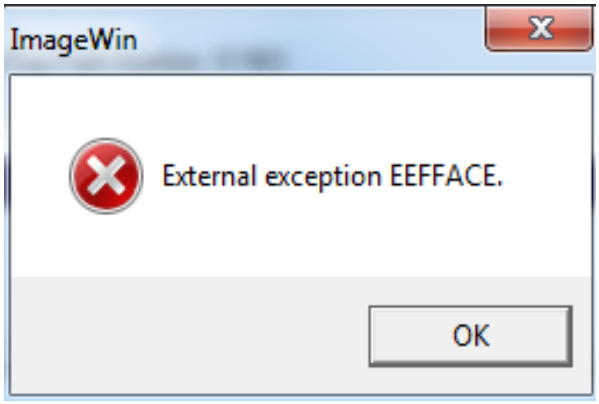

Figure 4-9: Tomo area of 150-600.

4.1.6 Sensitivity analysis - ray tracing method

The ImageWin program has three methods for ray tracing: a straight-ray tracing algorithm and two algorithms for curved ray tracing (John McGaughey and Zhou Bing's). Attempts to use these two algorithms on the MacLennan township data set gave two different errors; i.e. 1. "Floating point division by zero" and 2. "Floating point overflows", respectively (Figure 4-10.a and b). In theory, the curved ray tracing yields better results than straight ray tracing because it represents the physics more realistically. Perhaps these errors are a result of the specific hardware and operating system that the software was installed on. Perhaps these curved ray methods only work when there are significantly less cells. A detailed investigation of this issue was not undertaken.

In some cases, I found reinstalling the software on a different machine or sometimes even the same machine solved some of the issues I encountered.

The ImageWin algorithm utilizes amplitude tomography and generally curved ray processing is not used for amplitude tomography, mainly because the curvature is controlled by the velocity that is calculated based on the travel time or phase data (Prada et.al., 2000).

Figure 4-10: (a) The error in ImageWin using the John McGaughey's ray tracing method. (b) The error in ImageWin using the Zhou Bing's ray tracing method.

Hence, the tomograms in this study were generated using the straight-ray algorithm. The number of straight ray paths in one run is 85950 (Figure 4-11). The process of tracing the ray paths can be time-consuming, taking about 7 minutes.

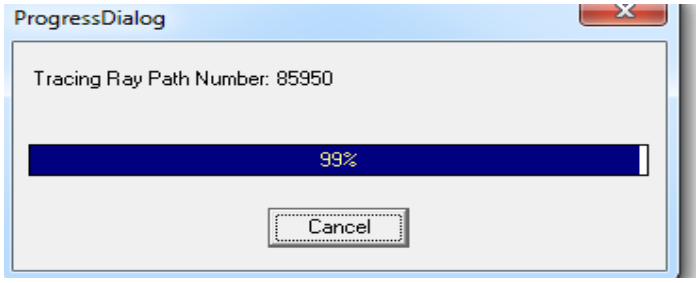

Figure 4-11: Number of straight ray paths in one run.

4.1.7 Sensitivity analysis for starting velocity model

The inversion of the tomographic data involves several iterative procedures which start with a specific initial model. The starting model for tomographic reconstruction is one of the choices that are made before tomographic construction in ImageWin. All starting models are homogeneous or constant over the whole panel (ImageWin help). There are four models currently implemented: maximum velocity model (default), minimum velocity model, average velocity model, zero slowness models. Figure 4-12.a, b, c and d shows the calculated conductivity tomograms using all four different initial models.

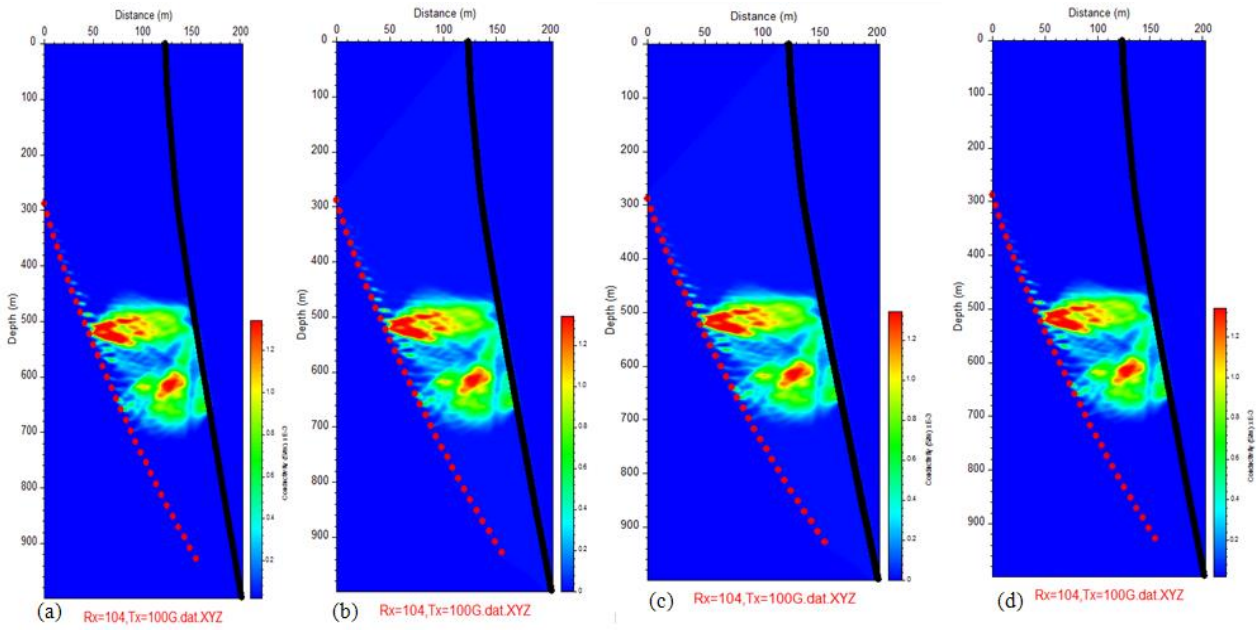

Figure 4-12: (a) Average velocity as an initial model. (b) Zero slowness as an initial model. (c) Minimum velocity as an initial model. (d) Maximum velocity as an initial model.

Figure 4-12.a through Figure 4-12.d show the same appearance and conductivity range and there is no evident difference in the features of interest in the tomograms. Exporting the conductivity values for each of these cases and plotting them will allow us to compare the results. The exported data consists of the conductivity values of column of cells within the discretized domain used in the model.

Figure 4-13 shows the plot of the conductivity as a function of depth. It should be noted that in ImageWin the depth scale is not defined for all points along the Z-axis but is only defined at certain locations. Therefore, it is only possible to see the conductivity between about 900 and 1200 m depth, while the actual depth range of the tomographic survey is approximately 1100 to 1960 m. There is essentially no difference between the four sets of results; in all cases two zones of high conductivity are visible.

Elsewhere in this study, the maximum velocity model was used for all calculated tomograms since this is the default initial model suggested by the ImageWin software.

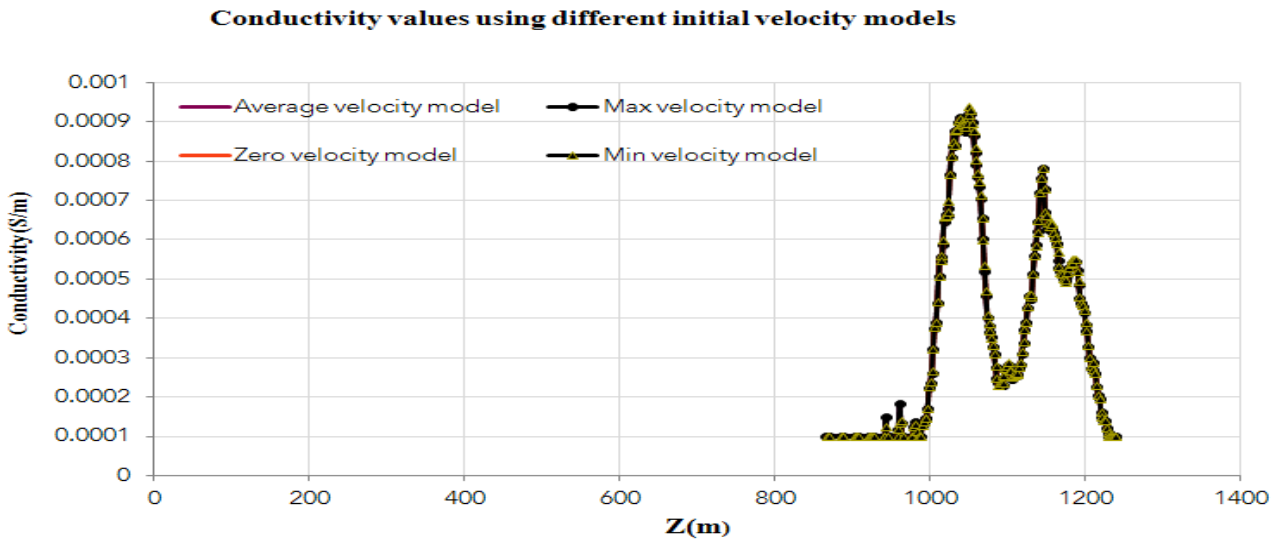

Figure 4-13: Conductivity values in terms of depth using various initial velocity models.

4.1.8 Sensitivity analysis for various tomographic algorithms

Various mathematical algorithms can be selected in ImageWin in order to solve for the tomographic inverse problem and to determine the absorption coefficients and hence to construct the tomogram. The four different algorithms currently implemented in ImageWin are: ART, SIRT, CGLS and LSQR (Figure 4-14.a, b, c and d). The default algorithm in ImageWin is SIRT. In this section, the four algorithms will be tested and the results are evaluated by displaying the images and plotting the conductivity as a function of depth.

Tomograms shown in Figure 4-14.a -d are shown with the same colour scales for all four panels. The SIRT has the most red or conductive features, followed by ART, LSQR, and finally CGLS

which has the smallest red area. In terms of appearance, all four tomograms show both the upper and lower zones. However, in between these two zones the results show variations in the computed conductivity values. The SIRT tomogram is the smoothest, but it shows some ray path artifacts (straight line features) in the top zone (Figure 4-14.a). The ART tomogram is somewhat noisy in comparison to SIRT (Figure 4-14.b) and shows more ray path artifacts. The LSQR tomogram has the strongest bias towards the transmitter (Figure 4-14.c) and a cross-hatching artifact. The CGLS tomogram in Figure 4-14.d shows least bias to the transmitter, and a cross hatching artifact.

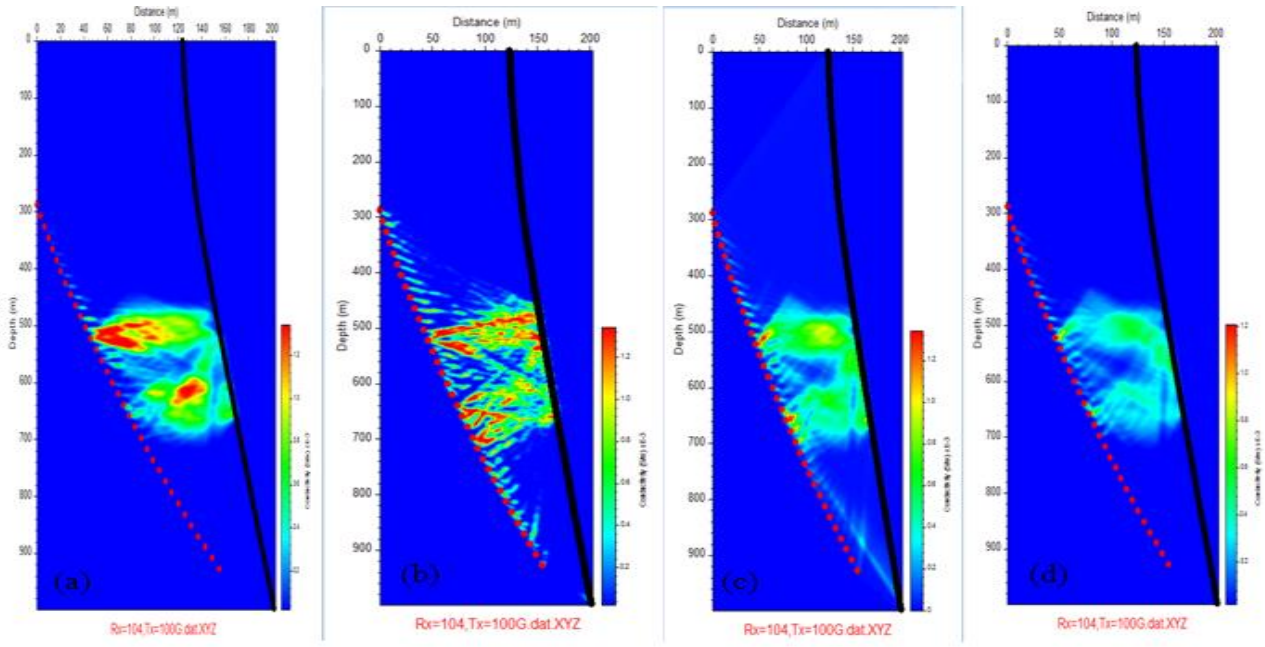

Figure 4-14: (a) Constructed tomogram using SIRT. (b) Constructed tomogram using ART. (c) Constructed tomogram using LSQR. (d) Constructed tomogram using CGLS.

The data misfit in each case is shown in Table 4-5. The SIRT algorithm with the lowest data misfit of 18.83 is chosen to be the best algorithm in this study.

Table 4-5: The data fit for various algorithms.

Algorithms	RMS	
	1 iteration	**2 iterations**
SIRT	19.29	18.83
ART	24.15	23.22
LSQR	21.81	20.31
CGLS	21.88	20.63

The exported conductivity values were plotted as a function of depth in Figure 4-15. The computed conductivity results obtained based on the SIRT algorithm showed two conductive zones on the red curve. The first conductive zone is located at 1040 m depth with the highest conductivity of 0.0009 S/m and then there is a second double peaked zone centered at 1180 m which has a peak conductivity of 0.0008 S/m.

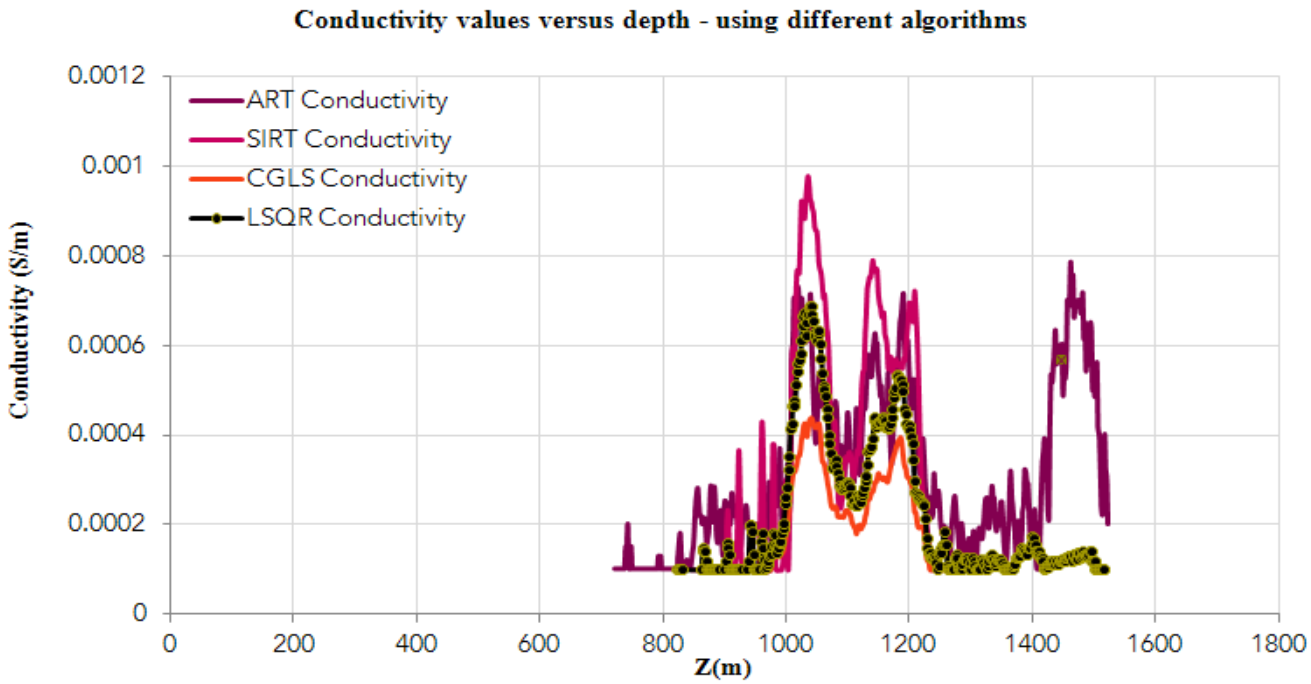

Figure 4-15: Conductivity values in respect to the depth using different tomographic algorithms.

The blue curve with three conductive zones in Figure 4-15 shows the depth plot of the exported conductivity values that were calculated using the ART algorithm. The first conductivity peak in the blue curve is at the same position as the first conductive peak in the red curve at about 1040 m. Furthermore, the position of the second double-peaked zone in the blue curve matches that of the double-peaked zone in the red curve at about 1180 m depth. However, the third peak in the blue curve associated with ART algorithm at 1480 m depth has the highest conductivity of 0.00075 S/m across the studied area. This zone is close to the transmitters in MAC100G and likely some type of transmitter artifact.

The purple curve in Figure 4-15 shows the conductivity values calculated using LSQR algorithm. The first conductive zone is located at about 1040 m depth with the conductivity of 0.00062 S/m and the second zone is placed at about1180 m depth with a conductivity of 0.0005 S/m. This second zone is not a double peaked zone, but has a single peak. This plot looks similar to the SIRT curve in terms of the smoothness.

The green curve in Figure 4-15 shows the plot of the conductivity versus depth obtained from the CGLS algorithm and illustrates that the first conductive zone is at 1040 m depth with the conductivity of 0.00042 S/m and the second zone (here single peaked) is located at 1180 m with the conductivity of 0.00035 S/m. The CGLS curve is smooth, and the conductivities are less.

For this example, the SIRT algorithm is smooth but shows some bias towards large conductivity values near the transmitter. The LSQR and CGLS algorithms show less bias but a smaller range of conductivity values.

In order to compare different tomographic algorithms more extensively, the tomograms are also constructed for higher number of iterations as shown in Figure 4-16. The misfit for each of the ten iterations using the four algorithms is shown on Table 4-6.

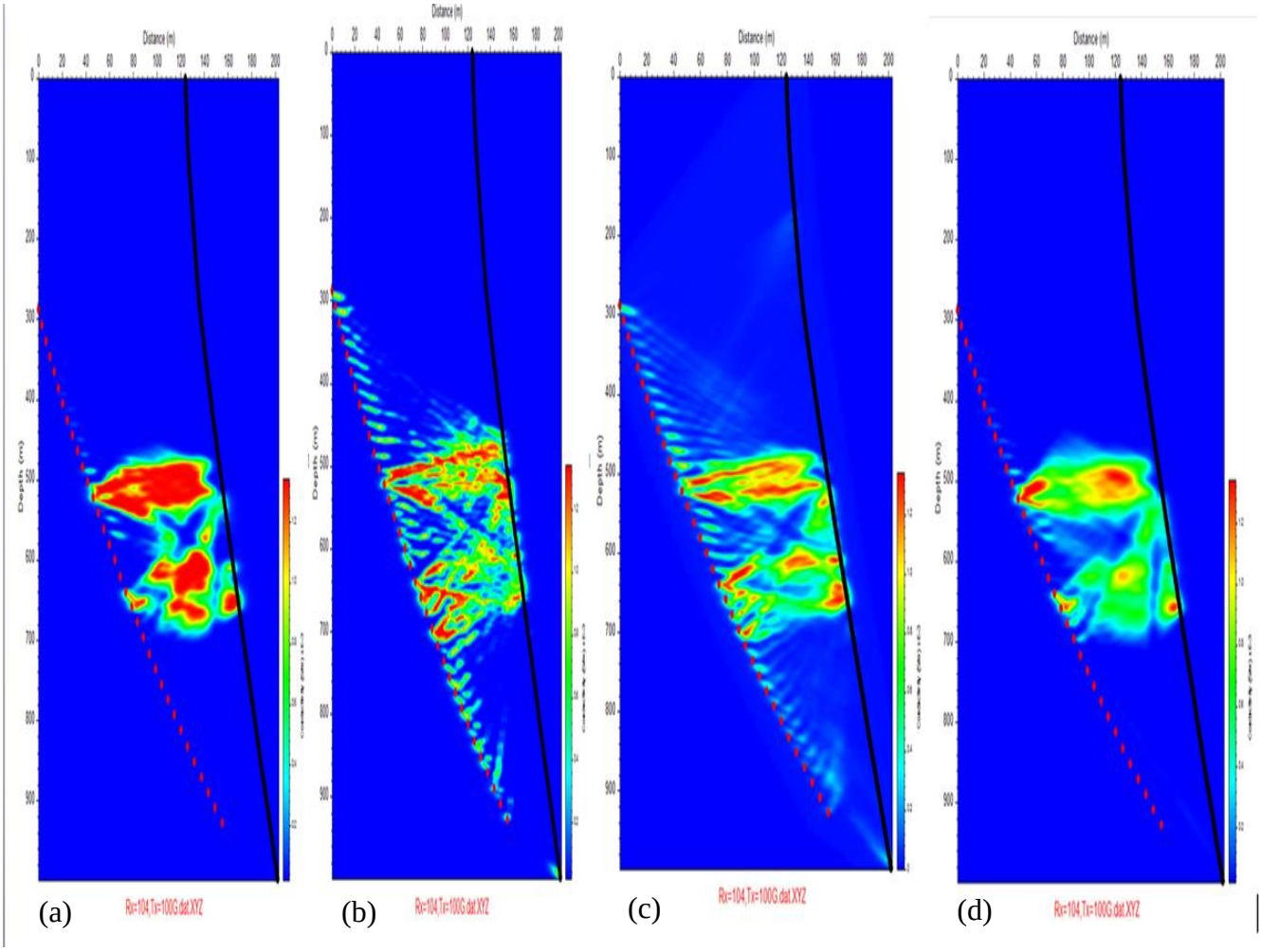

Figure 4-16: All four tomograms were constructed using ten iteration steps (a) Constructed tomograms using SIRT algorithm. (b) Constructed tomogram using ART algorithm. (c) Constructed tomogram using LSQR. (d) Constructed tomogram using CGLS.

Tomograms shown in Figure 4-16.a -d use the same colour scales for all four panels. By increasing the number of iterations from three to ten, the tomograms show more distinct features. Comparing the tomograms constructed with three iterations with the tomograms constructed with

ten iteration shows that the SIRT algorithm produces a smoother tomography than does the ART algorithm. For the SIRT algorithm, the data misfit value of 18.83 after two iterations dropped to 18.25 after 9 iterations. The SIRT image looked a little more saturated to red values, but otherwise quite similar. Given that only small drop in the misfit values was observed with the increased iterations, and that significantly more computation time was required, more than three iterations did not seem necessary.

The ART algorithm looks quite similar on Figure 4-14.b and Figure 4-16.b and the misfit has actually increases slightly from 23.22 to 23.26 going from 3 to 10 iterations. In this case three iterations seem sufficient.

The data misfit for LSQR increased from 20.31 (three iterations) to 24.54 (ten iterations). The LSQR image (Figure 4-16.c) showed more structure after 10 iterations, but the greater misfit implies that the structure might not be believable. In this example more iterations does not seem to be beneficial.

There is a significant difference between the CGLS images on Figure 4-14.d and Figure 4-16.d, suggesting that this algorithm continues to converge after three iterations. The data misfit for CGLS decreased from 20.63 (three iterations) to 18.89, a relatively large reduction, but a misfit still greater than SIRT after two iterations. For CGLS more iterations can provide better results, but not significantly different from three iterations of SIRT.

The SIRT and CGLS seem to have the same level of smoothness after ten iterations, show similar features and have similar misfits. The CGLS algorithm is the only one that significantly reduced the RMS misfit after three iterations. However, the images do change from three to ten iterations for the SIRT, LSQR and CGLS algorithms. If these changes are judged to be improvements, perhaps misfit is not a good indicator of a good image.

Table 4-6: Data misfit for ten iterations when using four different algorithms.

Algorithm	Data misfit (RMS) using different number of iterations								
	1	2	3	4	5	6	7	8	9
SIRT	18.33	18.31	18.29	18.28	18.27	18.26	18.26	18.26	18.25
ART	24.15	23.22	23.18	23.22	23.22	22.23	23.24	23.25	23.26
LSQR	21.81	20.31	22.93	22.45	23.81	23.84	24.46	24.31	24.54
CGLS	21.88	20.63	19.75	20.43	19.23	19.05	19.04	18.86	18.89

4.1.9 Sensitivity analysis for different types of weighting

Two styles of weighting can be applied if the ART or SIRT algorithms are selected. Clamping weights are intended for the case when there is a discrete and high contrast target to be imaged (Pears and Fullagar, 1998). Central weights can be utilized to enhance the visibility of the physical features in the middle of the tomogram. The intent is to move conductive features that we see in some of the previous examples away from the transmitter.

In order to better understand the weighted tomographic imaging, the tomograms were constructed using the SIRT algorithm with no clamping (Figure 4-17.a), weight clamping (Figure 4-17.b), central clamping (Figure 4-17.c), and mixed weight and central clamping (Figure 4-17.d). Figure 4-17.a through Figure 4-17.d show the same conductivity range while they are different in showing the geometry of the conductive zones.

No clamping results are shown in Figure 4-17.a, where the upper conductive zone dips from MAC100G to MAC104 and the second zone is more focused in the center of the image. Figure 4-17.b depicts the conductive zones with sharper edges, giving a bimodal blue and red image. As expected, the case with central clamping (Figure 4-17.c) shows both conductive zones in the center of the image. This image is also dominated by blues and reds. The mixed case (Figure 4-17.d) is very similar to Figure 4-17.b, except zones near the holes are erased. Whether

clamping and or central weighting is used will depend on the geological situation. If it is known that the conductive zone is in the centre of the panel, then central weighting might be appropriate; similarly if it is known that there is a high contrast target (red compared with a blue background), then clamping weights might be appropriate. However, the clamping weights image shows ray-tracing artifacts that do not appear geological, so in this example, no weighting of any kind might be appropriate.

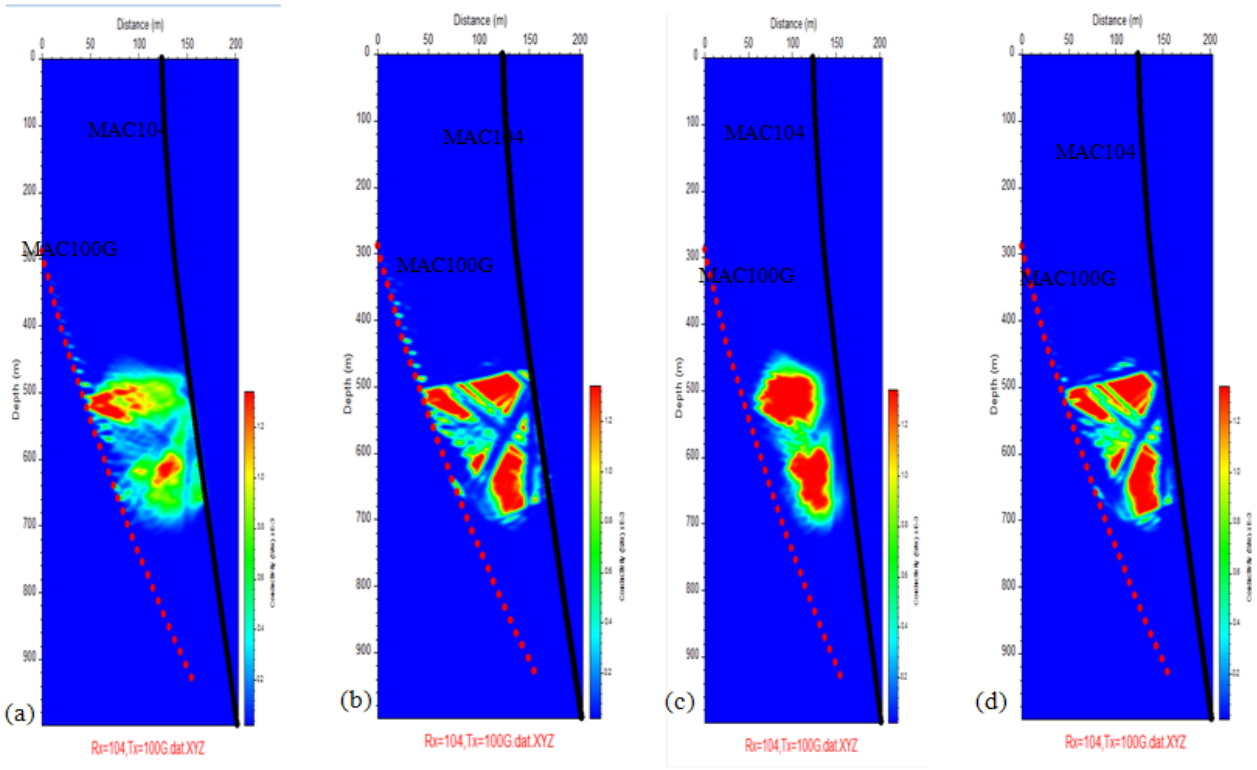

Figure 4-17: (a) Conductivity tomogram with no Clamping Weight. (b) Conductivity tomogram with clamping weight. (c) Conductivity tomogram with central Weight. (d) Conductivity tomogram with clamping and central weight. The SIRT algorithm is used in all cases.

4.1.10 Sensitivity analysis for number of iterations using SIRT

In the discussion above, it is shown that it is possible to adjust the number of iteration to compute the tomogram. In this section this is studied in more detail for the SIRT algorithm. This was tested on the (Rx=MAC104, Tx=MAC100G) dataset for Vmin, Vmax = (2, 16) to see how selecting the number of iterations in the SIRT algorithm might be able to improve the tomogram.

In order to get the optimal number of iterations and convergence rates, conductivity tomograms at different number of iterations were compared, and the data misfit is observed. The tomograms constructed with 1, 2, 3, 4 and 5 iterations are shown in Figure 4-18.a-e.

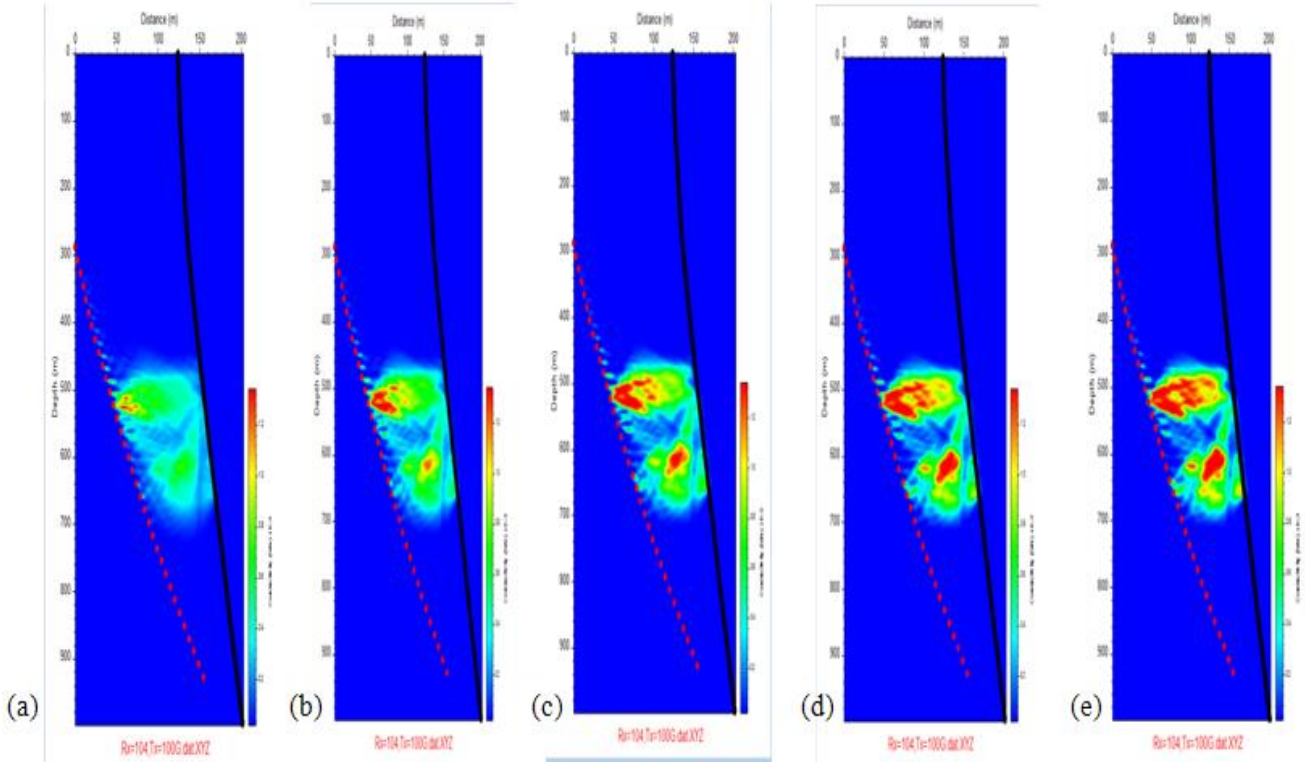

Figure 4-18: (a) Calculated tomogram with one iteration (Vmin=2, Vmax=16). (b) Calculated tomogram with two iterations. (c) Calculated tomogram with three iterations; (d) Calculated tomogram with four iterations (e) Calculated tomogram with five iterations. (the colour scales are the same).

In terms of appearance, as the number of iterations increases, the conductive zones on the tomograms become more visible and the bias of conductive zones towards the transmitter is reduced. These tomograms were for the case when (Vmin, Vmax) = (2, 16). The data misfits for the five different number of iterations (1 to 5) are 18.33, 18.31, 18.29, 18.28 and 18.27 respectively. The results verified that the data misfit decreases with increased number of the

iteration. However, the misfit changes are small, but there are significant changes in the images. This suggests that the number of iterations is a very important parameter in getting good results.

The tomograms constructed at (Vmin, Vmax) = (0.5, 16) are shown in Figure 4-19.a-d. In this case, the data misfit is 18.4, 18.3, 18.22 and 18.17 respectively after one to four iterations. Also, the colour scale varied slightly and the highest conductivity shown in the color scale changed with varying number of iterations: 0.0016, 0.0003, 0.0004 and 0.0005 S/m respectively from one to four iterations.

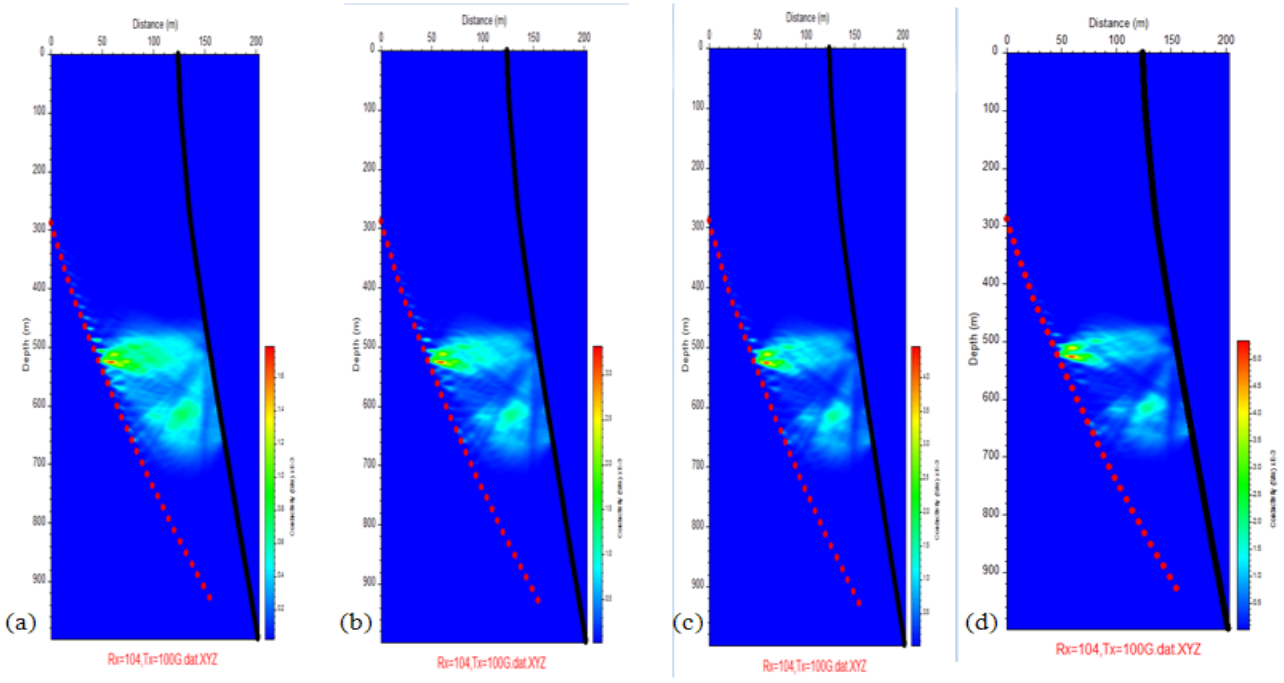

Figure 4-19: (a) Calculated tomogram with one iteration (Vmin=0.5, Vmax=16). (b) Calculated tomogram with two iterations. (c) Calculated tomogram with three iterations. (d) Calculated tomogram with four iterations.

Table 4-7: Data misfits for (Vmin=0.5, Vmax=16) in 5 iterations.

Algorithm	RMS value for different number of iterations			
	1	2	3	4
SIRT	18.4	18.3	18.22	18.17

4.2 Discussion of the results for the reciprocal data sets for the optimal parameters

The optimal parameters were chosen based on the consistency of the tomograms with the two attenuated zones shown in the graphs of amplitude raw data with respect to the depth and the ray masking option that also have shown two attenuated zones with a separation from each other. The second parameter is the fit to the data (RMS value) that is presented in various sensitivity analysis tables. The RMS misfit provides a measure of the overall fit of the tomogram to the data. Ideally, the RMS value should be close to the expected uncertainty in the data. More generally, a tomogram with a small RMS misfit should be preferred over another with a larger RMS. Hence, the optimal parameters and variables are given as the following:

1. Vmin=2, Vmax=16 m/s.
2. Straight ray path.

3. Maximum velocity model.
4. SIRT algorithm.
5. No weighting.
6. Three iterations.

The “optimal” attenuation tomograms for reciprocal data sets are shown in Figure 4-20.a and Figure 4-21.a with the data misfit.

Using the conversion option of the ImageWin, the conductivity tomograms were constructed by converting the attenuation data to the conductivity values (Figure 4-20.b and Figure 4-21.b). Comparing the attenuation and conductivity tomograms in terms of appearance, it is evident that, although the difference is not significant, the width of the conductive zone in the conductivity tomogram appeared to be smaller in size compared to the attenuation tomogram.

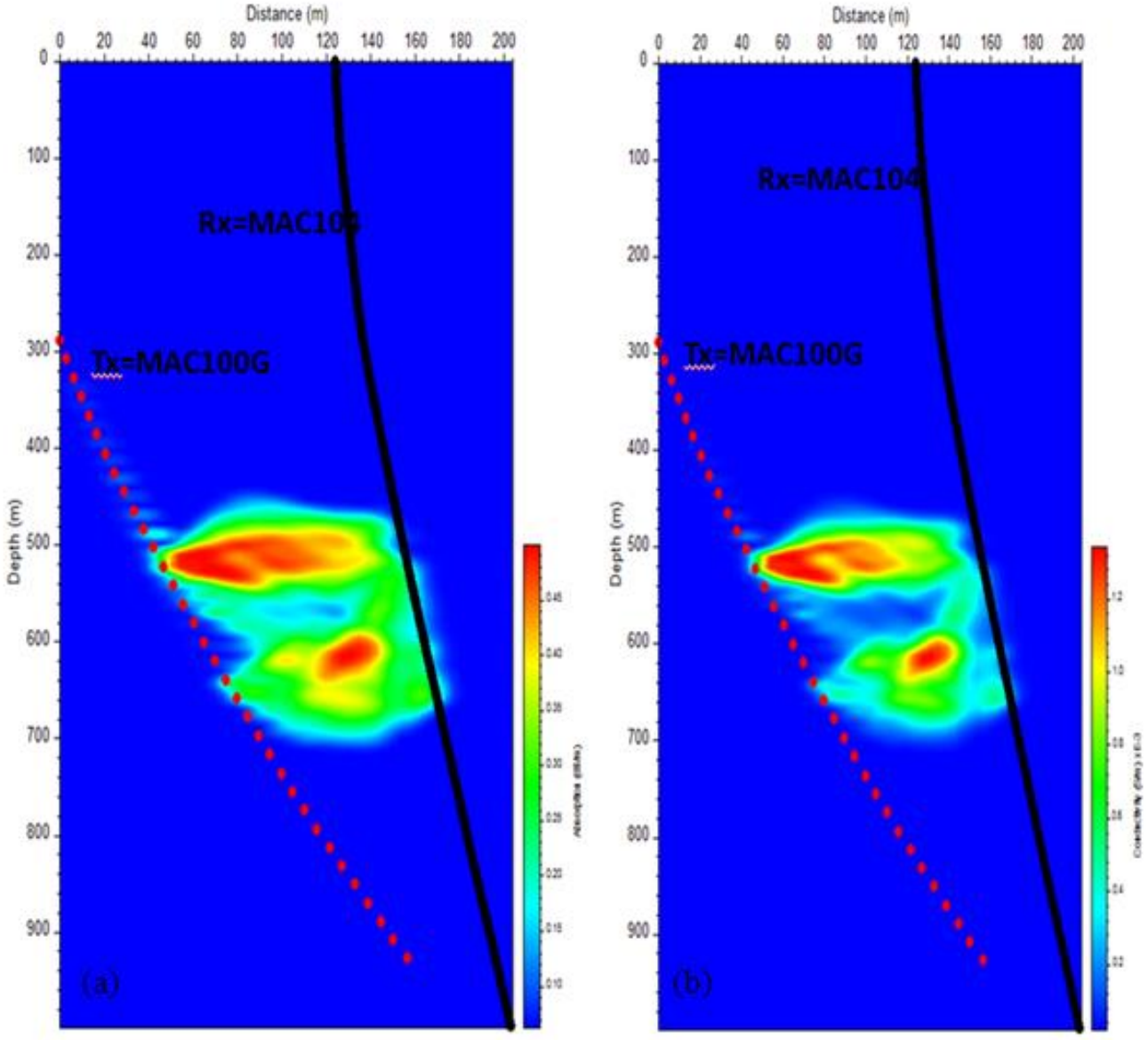

Figure 4-20: (a) Attenuation tomogram for (Tx=MAC100G, Rx=MAC104) data set in 625 kHz (using best values in the inversion with editing and smoothing applied). (b) Conductivity tomogram for (Tx=MAC100G, Rx=MAC104) data set (using best values in the inversion with editing and smoothing applied.

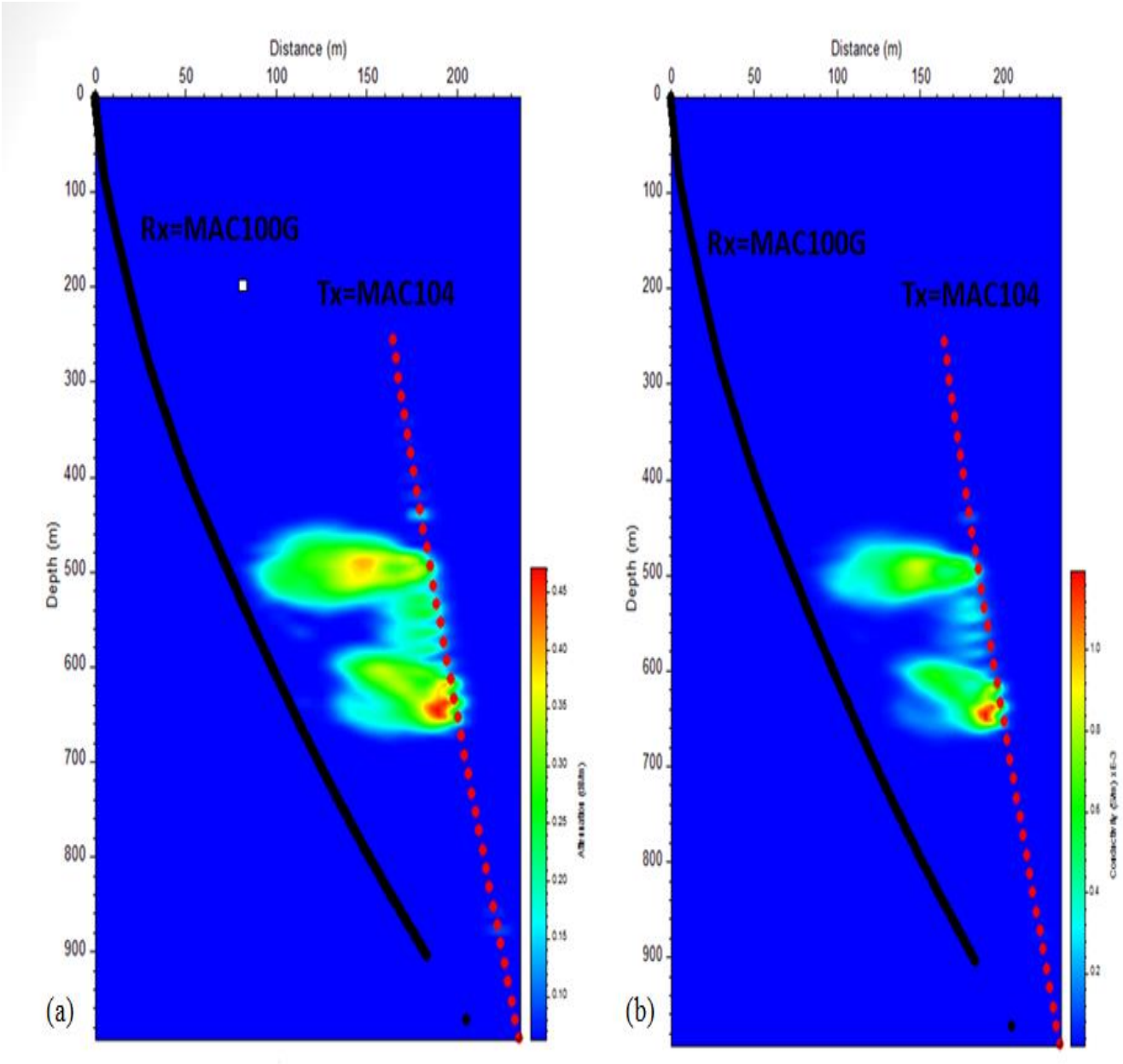

Figure 4-21: (a) Attenuation tomogram for (Tx=MAC104, Rx=MAC100G) data set in 625 kHz (using best values in the inversion with editing and smoothing applied). (b) Conductivity tomogram for (Tx=MAC104, Rx=MAC100G) data set (using best values in the inversion with editing and smoothing applied.

Furthermore, using the same parameters on the two different copies of the ImageWin software installed on two different computers resulted in different tomograms shown in Figure 4-22.a Figure 4-22.b.

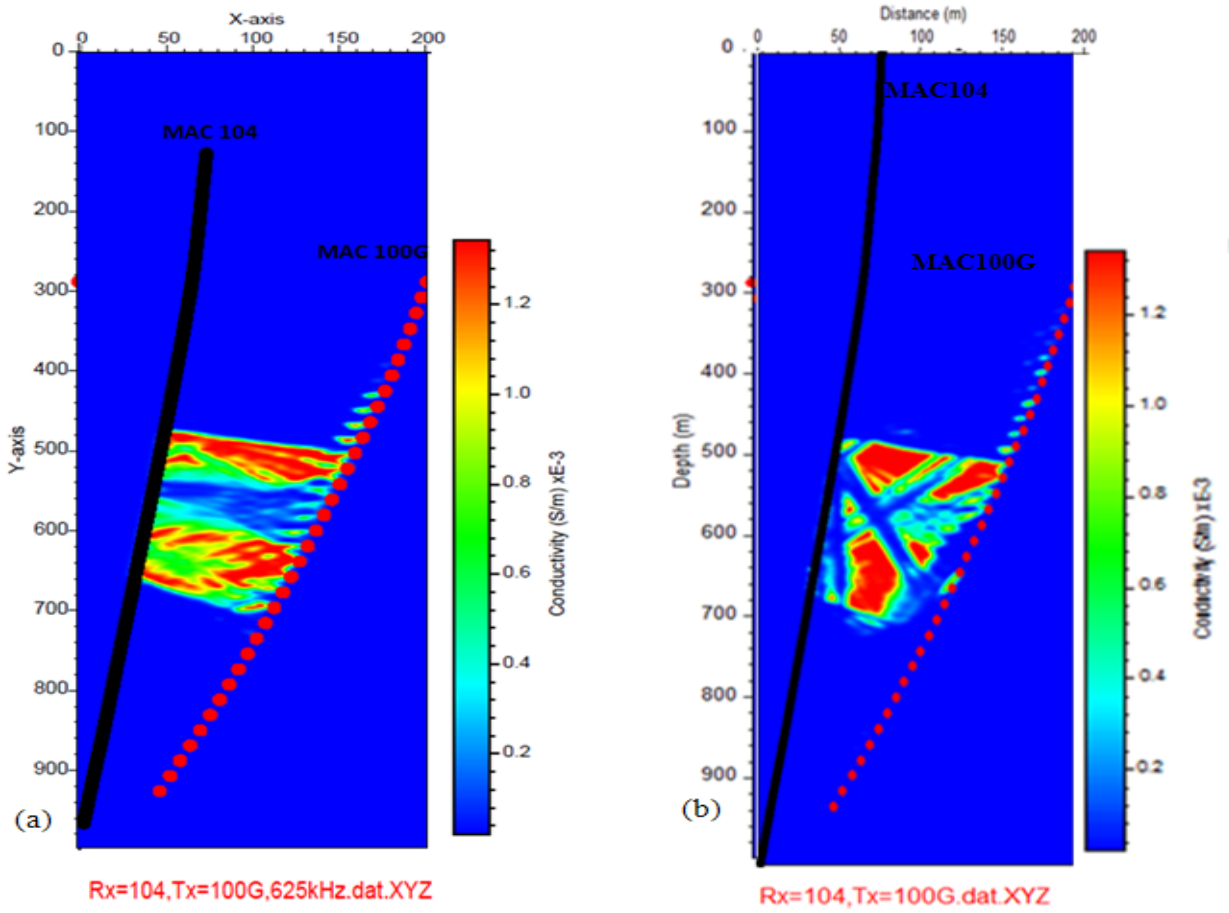

Figure 4-22: (a) Conductivity tomogram for Tx= MAC104, Rx= MAC100G dataset in 625 kHz. (ImageWin was installed in computer 1). (b) Conductivity tomogram for Tx= MAC104, Rx=MAC100G dataset in 625 kHz. (ImageWin was installed in computer 2).

The tomograms presented in Appendix C show the images of the ore body before splitting the data sets and before reducing and editing or smoothing the amplitude data. Higher quality tomograms were constructed after processing the raw data based on what was discussed in Chapters 2, 3 and 4, i.e., amplitude reduction, ray masking and optimal inversion parameters.

5 Generating a Single Conductivity Tomogram

The two reciprocal tomograms derived using the optimal parameters in Chapter 4 are merged into one data set using the Geosoft software. The procedure for averaging the two data sets is explained in this section and then the resulting average conductivity tomogram is interpreted.

Figure 5-1.a and 5.1.b show two snapshots of how to create a new database in Geosoft. On the Database menu, the Create New Database dialog enables the user to create and define a new database for a target by setting the initial size of the database (Figure 5-1.a). The conductivity values are exported from ImageWin as a file containing the Cartesian coordinates (X, Y, Z) and the conductivity. There is one such file for each of the two reciprocal datasets. One of these is shown being imported in the second dialog box (Data Import Wizard) in Geosoft as an Ascii file in Figure 5-1.b.

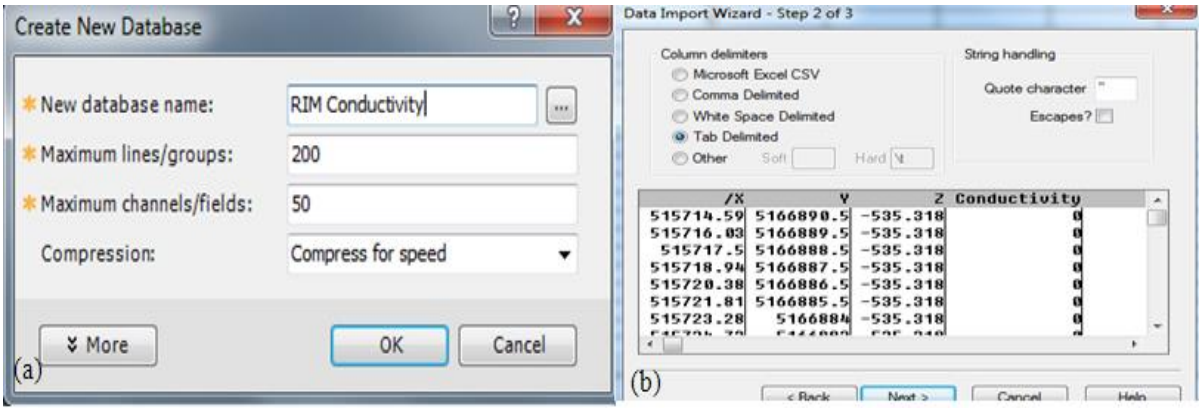

Figure 5-1: (a) New database dialog box in Geosoft. (b) Data Import Wizard dialog box in Geosoft.

The Voxel Grid GX was used to perform 3D Gridding by applying a basic statistical kriging algorithm to create a 3D voxel grid model from 3D (X, Y, Z, value) data contained in a Geosoft database as a GDB file. It is worthwhile mentioning a "Voxel" is a short for "volume pixel", the smallest distinguishable box-shaped element of a three-dimensional image and it is the 3D conceptual equivalent of the 2D pixel (Geosoft Help).

The X, Y are the horizontal directions (easting and northing) and Z is positive up (Geosoft Help). The "New Voxel file" was given the name "Conductivity Average" (Figure 5-2), and then the cell size was chosen to be 2 m.

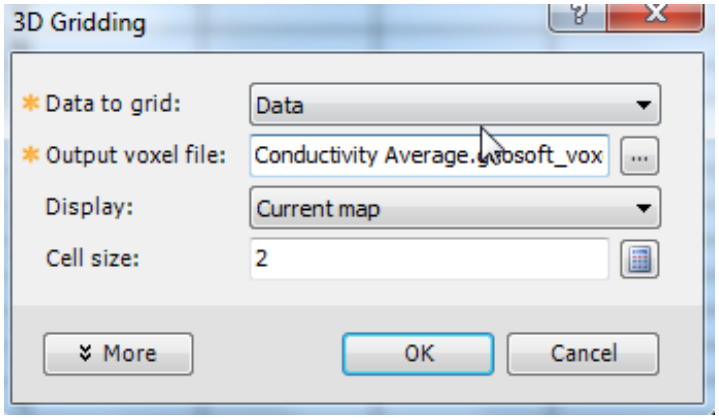

Figure 5-2: 3D gridding in Voxel Grid GX.

It usually takes 4-5 minutes for a Variogram to be constructed by Geosoft (Figure 5-3).

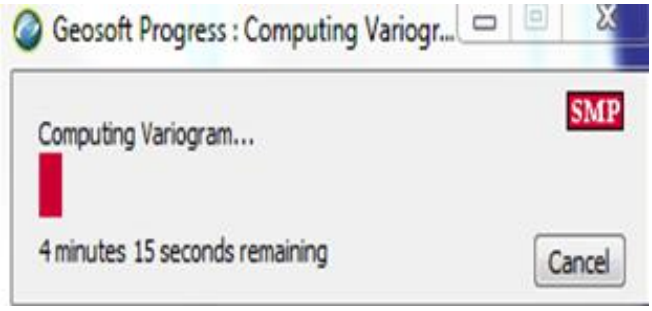

Figure 5-3: Computing the Variogram Window.

Figure 5-4 and Figure 5-5 show two Voxel grids that were created by Geosoft. In both these, the warmer shades indicate the higher attenuation rate (conductive) zones while the colder shades are indicative of the normal resistive zones. The colour transform is a linear distribution and the corresponding colour bar shows a maximum conductivity value of 0.0013 S/m.

In these reciprocal data sets, the estimated conductivity distributions are different. In Figure 5-4, two highly conductive zones are evident that extended outwards from the holes, whereas, in Figure 5-5, two moderately conductive zones can be identified close to the transmitter location. The image on the left is the tomogram displayed using the Geosoft software, where a depth scale is evident on the right of the 3D box (but there is no colour bar). The image on the right is displayed using the GOCAD software, where there is no depth scale, but the colour bar is shown on the bottom of the tomogram. Both data sets show two conductive zones that are located between 1000 to 1200 m depth. The exported data set from Geosoft was also imported in

GOCAD to better demonstrate the color changes using different range of conductivity values. The conductivity data range is 0.0002-0.0012 S/m (Figure 5-4 and Figure 5-5).

The second reciprocal data set also imported in Geosoft and GOCAD (Figure 5-5). As before, the maximum conductivity is 0.0013 S/m and the conductive zones are located between the depth of 1000 and 1200 m. The resulting conductivity tomograms shown in Figure 5-4 and Figure 5-5 were averaged in Geosoft using Voxel math utility by importing the $VO = (V1 + V2)/2$ formula as shown in the dialogue box of Figure 5-6.

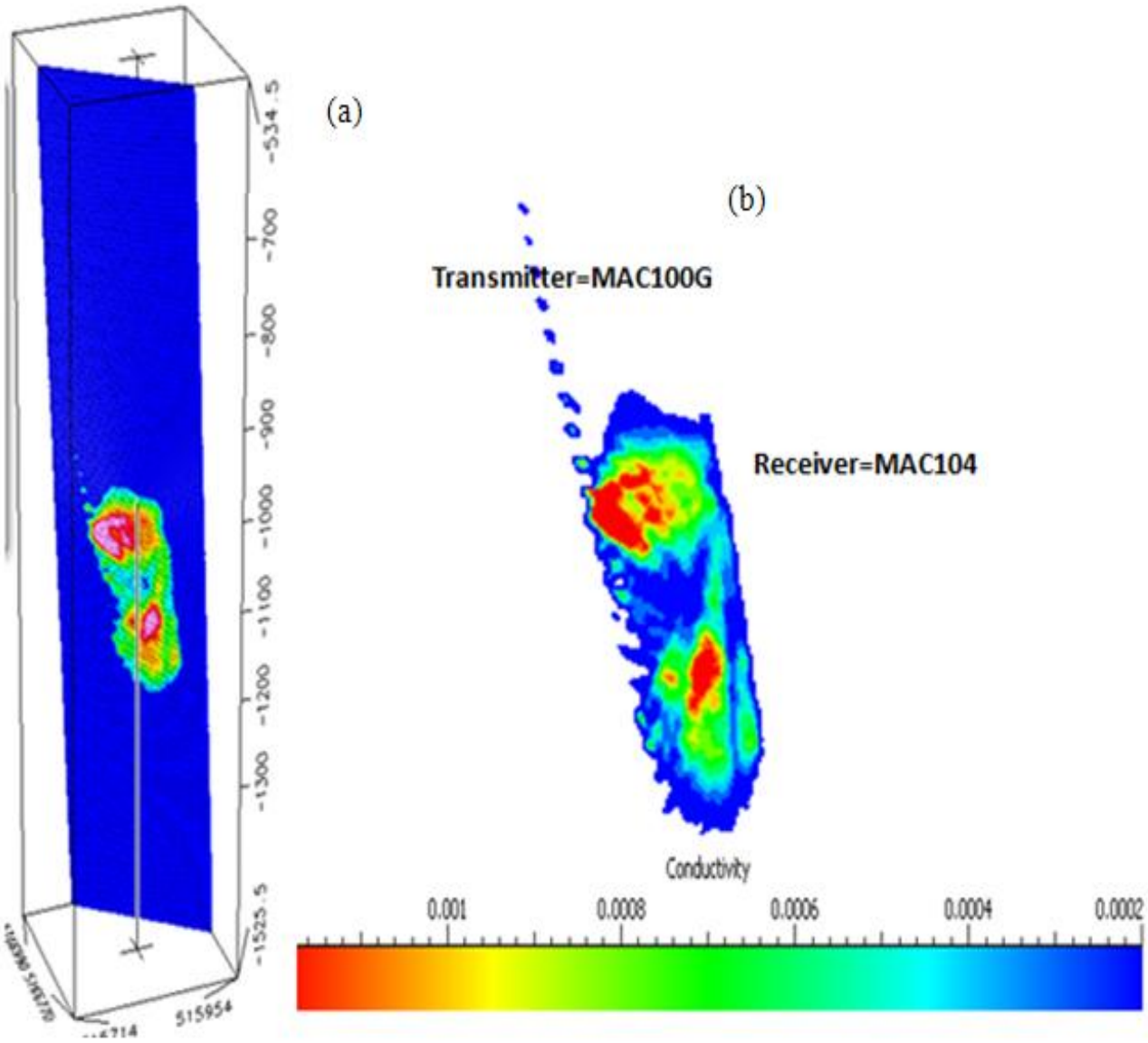

Figure 5-4: Conductivity in respect to the depth for Tx=MAC100G, Rx=MAC104 dataset in 625 kHz (Voxel data set V1). (a) The image on the left is from Geosoft, and (b) the right image is from GOCAD. The colour bar is for the GOCAD image.

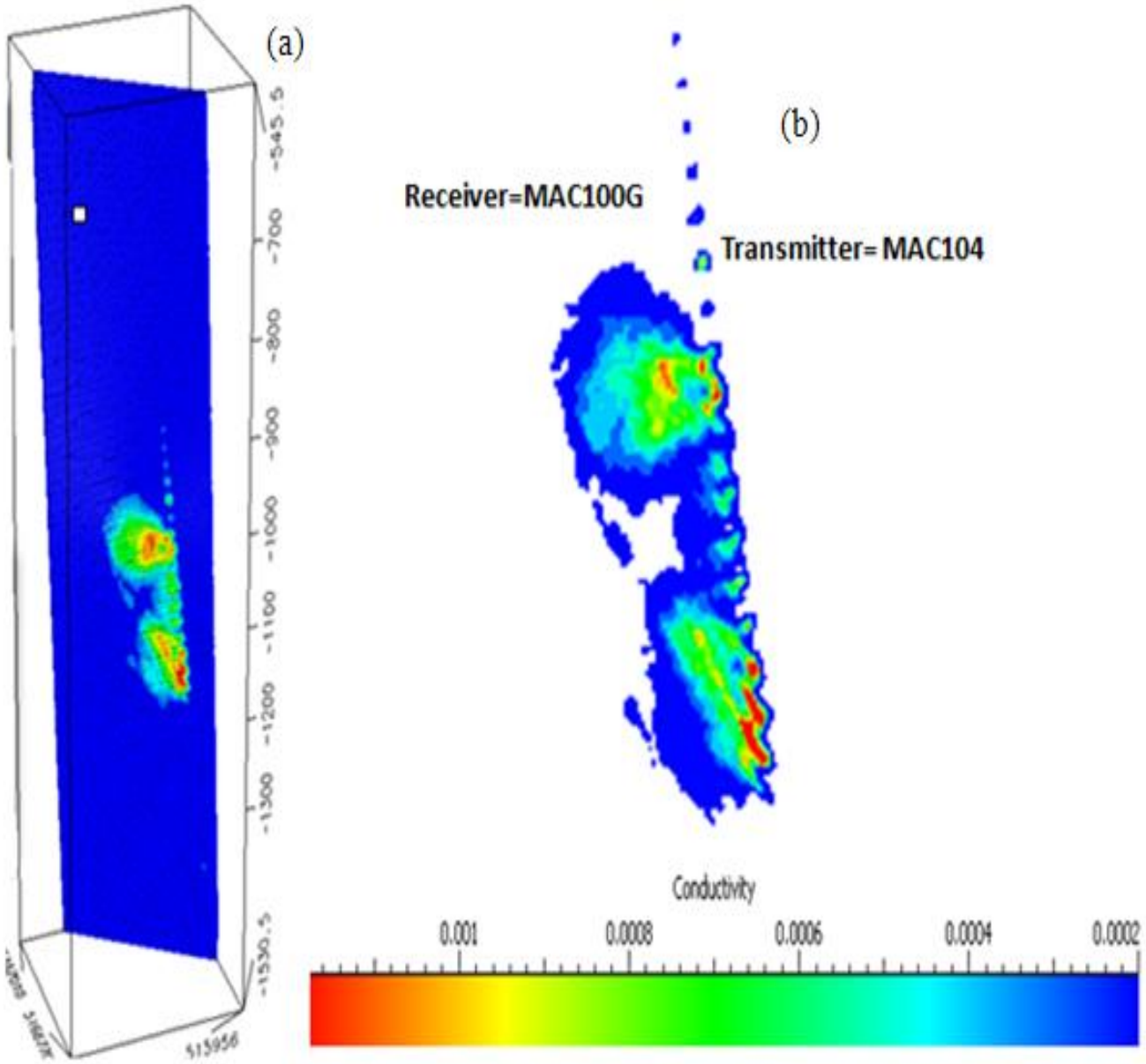

Figure 5-5: Conductivity in respect to the depth for Tx=MAC104, Rx=MAC100G dataset in 625 kHz (Voxel data set V2). (a) The image on the left is from Geosoft, and (b) the right image is from GOCAD. The colour bar is for the GOCAD image.

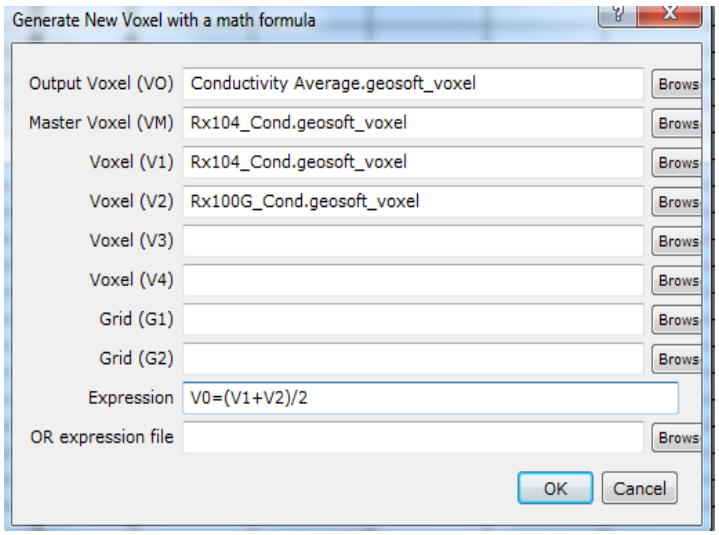

Figure 5-6: New Voxel with an average math formula.

The average tomogram V0 is shown on Figure 5-7, where there are two conductive zones, the first is located between 980 and 1100 m depth and the second zone is located between 1100 and 1150 m. These values are depth below the surface rather than depth down the hole.

Both conductive zones evident in Figure 5-7 dip from MAC100G to MAC104. The resulting average tomograms are shown in Figure 5-7.a, 5.7b, and 5.7c. Figure 5-7.a is the tomogram created in Geosoft and the axis for the Z direction is to the right of the 3D box. The Figure 5-7b and 5.7.c is the averaged conductivity values that were exported from Geosoft and imported into the GOCAD software and displayed using two different colour bars. In Figure 5-7.b, the colours are distributed linearly between (conductivity min, conductivity max) = (0.0002, 0.0012) , whereas in Figure 5-7c the range is 0.0002 to 0.0005 S/m. Adjusting the colour bars is more

straightforward in GOCAD. When the colour range is smaller in Figure 5-7.c, the image appears more saturated, being primarily blue and red.

For comparing the average conductivity tomogram V0 with the tomogram generated by FARA, the FARA results were also imported into both Geosoft and GOCAD (Figure 5-8). The FARA tomogram in Geosoft shows the upper conductive zone at 1020 next to MAC104 dipping towards MAC100G at 1070 m, which appears to be the opposite of what is seen in the V0 tomogram. The lower zone is located at 1130 m next to MAC104 is also dipping towards MAC100G at 1210 m. The dip of this lower zone is ambiguous from the ImageWin average and is different on the two reciprocal data sets. Comparing the depths on the FARA resistivity image imported in Geosoft (Figure 5-8 left) with the FARA tomogram shown in Figure 5-9, it can be seen that a value of approximately 320 meters were added to the Z values, so a different depth scale is being used.

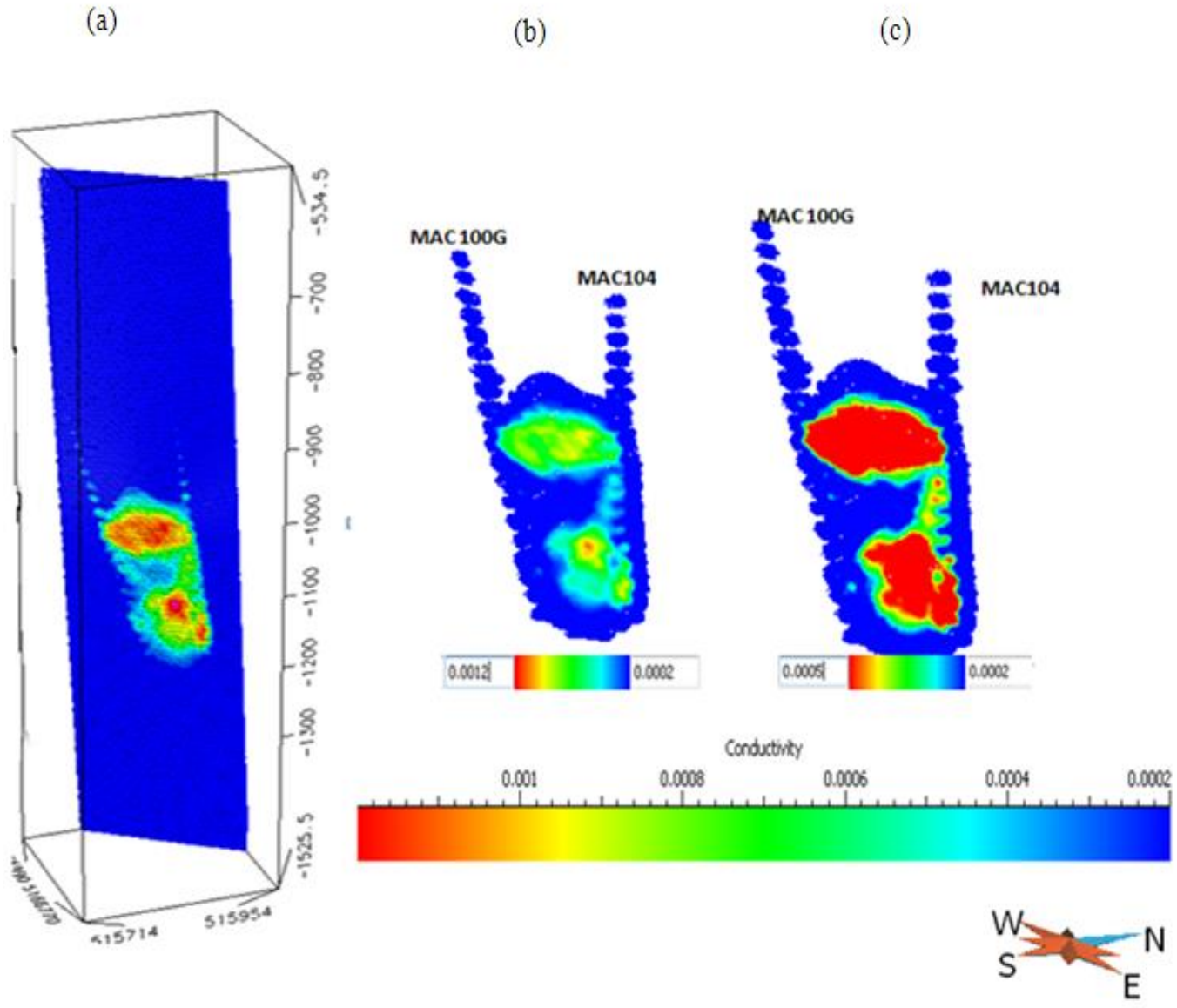

Figure 5-7: Average conductivity tomogram in 625 kHz (Average Voxel data set V0). (a) The image on the left is from Geosoft, and (b) the two right image are from GOCAD. The GOCAD images have a colour bar below each image. See text for the range. (The large colour bar at the bottom is for 3.7.b).

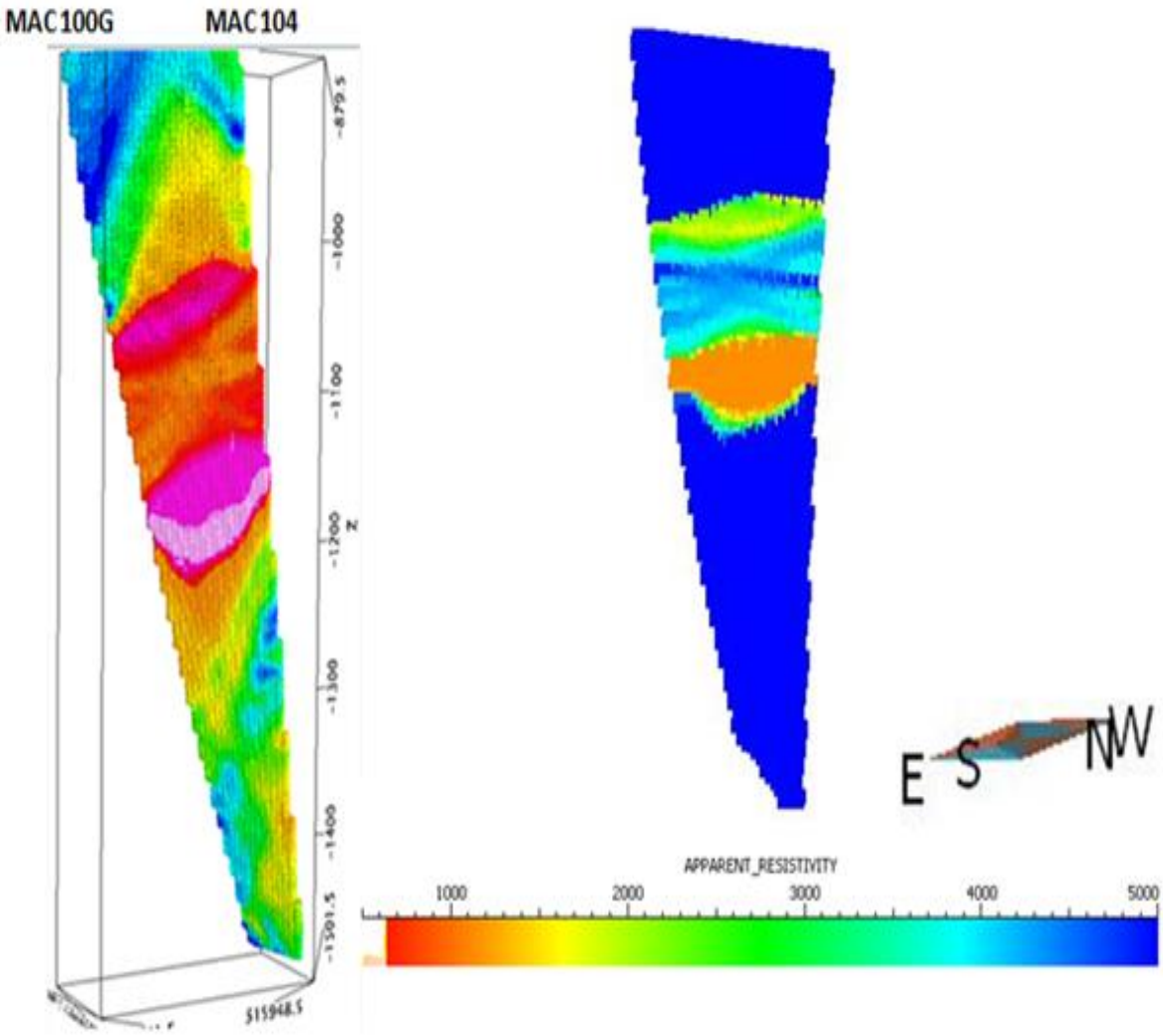

Figure 5-8: FARA resistivity in Geosoft (left) and GOCAD (right).

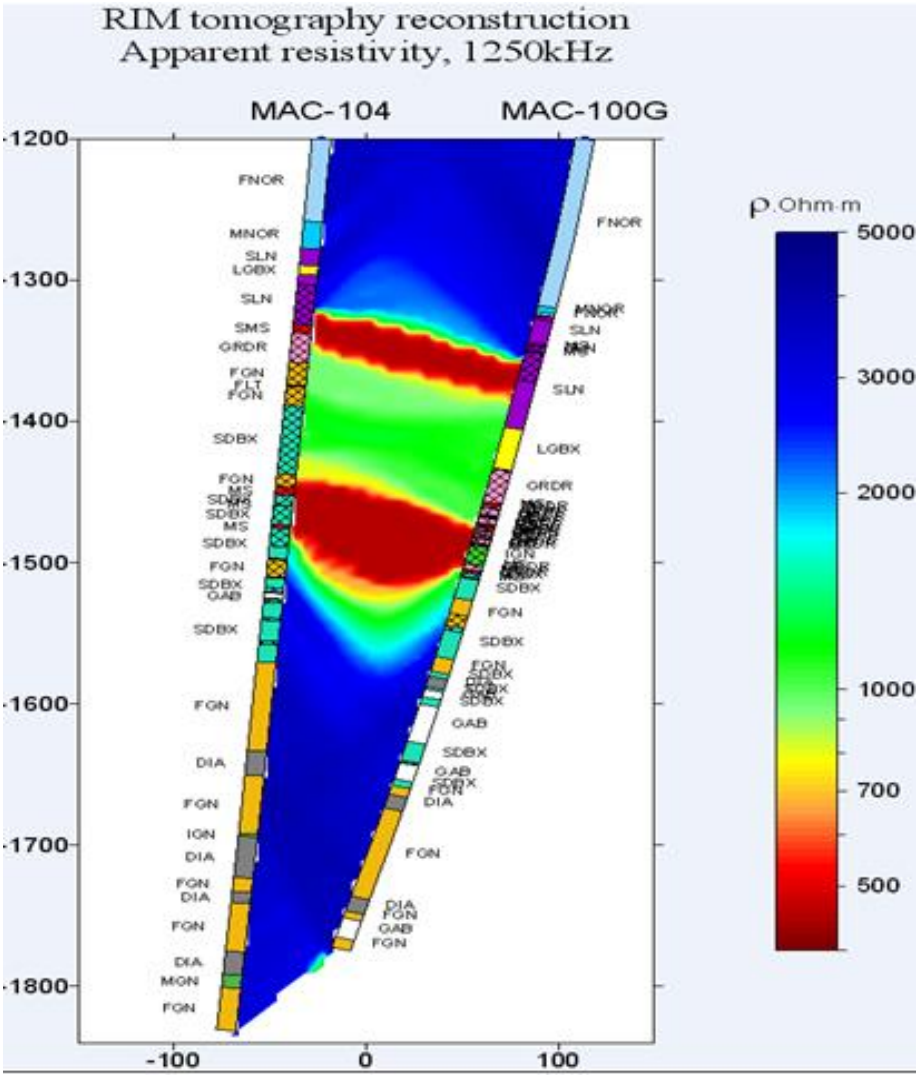

Figure 5-9: FARA tomogram for MAC104-MAC100G in 625 kHz (Figure taken by GEOFARA Ltd).

The FARA tomograms seem to be dominated by three colours, a blue resistive zone, a uniformly conductive red zone that stretches between the two holes and an intermediate zone between and above and below the two conductive zones. The Geosoft grid (Figure 5-8, left) shows a broader

range of colours, perhaps because the colour distribution has been normalized or equalized in some way. The tomograms derived from ImageWin show a variation in conductivity between holes. Determining which situation is more realistic requires geological input or control.

Both software packages ImageWin and FARA were able to identify the two conductive zones. Differences in the conductivity values of the upper and lower zones obtained from the two packages are to be discussed in the next chapter. It should be restated here that the author of this thesis has never used the FARA modeling tool and the comparison given here is based on the images provided by Sudbury Integrated Nickel Operations. However, the ImageWin tomograms seem to show more bias of the high conductivity zones RIM data to the location of the transmitter. The reciprocal data sets were similar in terms of being able to show the approximate location of conductive zones and continuity of the zones between the two holes. However, it is not known how the FARA algorithm deals with the reciprocal data sets. The maximum conductivity value obtained for the most conductive zones from the RIM tomography constructed in the ImageWin was relatively low, i.e. around 0.001 S/m corresponding to resistivity values of around 1000 Ω.m. The range of conductivity values obtained from ImageWin is equivalent to a conductive rock with less than 1wt% sulphide content. More detailed information about the sulphide contents in two of the studied holes (MAC 104 and MAC100G) has been provided by Sudbury Integrated Nickel Operations. For MAC 100G, the assays show 1.55 % Ni and 0.81 %

Cu for 11 m length sample in the contact zone and 0.53% Ni and 6.84% Cu for 9.67 m length sample in the footwall zone.

For MAC 104, the assays shows 2.05 % Ni and 1.06 % Cu for 6.2 m length sample in the contact zone and 0.53% Ni and 6.84% Cu for 9.67 m length sample in the footwall zone.

This section aims to further interpret the geological significance of the final results.

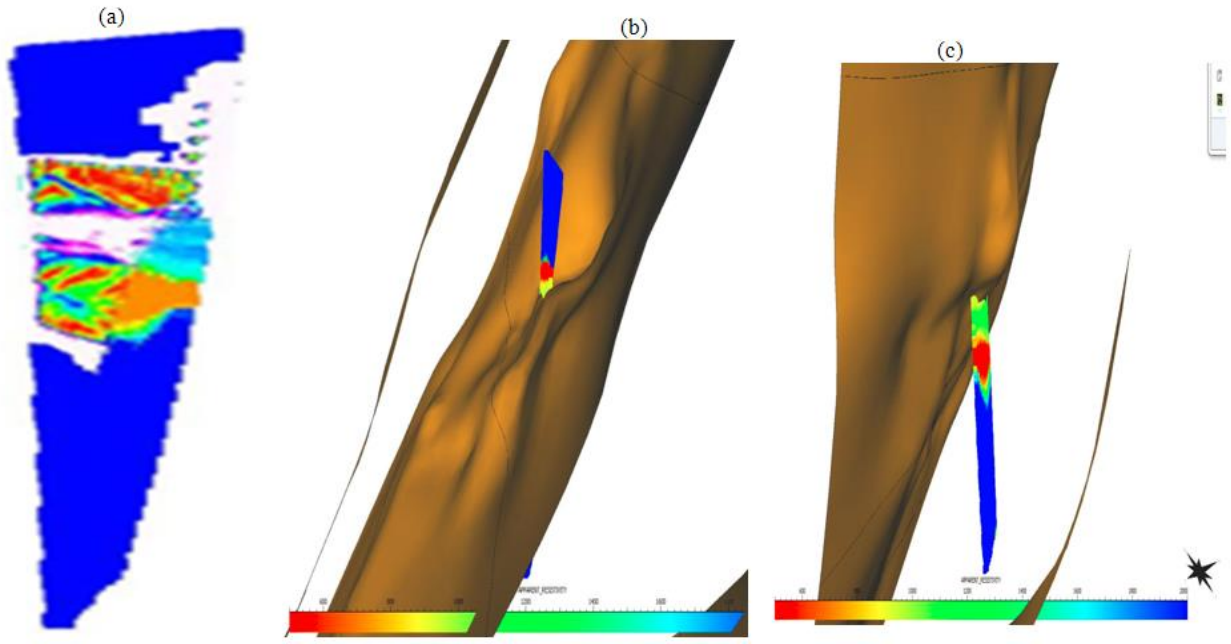

Figure 5-10: (a) The correlation of the ImageWin and FARA tomograms. (b) A view of the sub-layer contact surface showing the FARA tomogram for the upper zone, with the lower zone obscured and (c) the contact surface rotated so that the lower zone is evident and the upper zone obscured.

Figure 5-10.a shows the co-occurrence of the upper and lower conductive zones in the FARA and ImageWin tomograms and Figure 5-10.b and 5.10.c shows the imported RIM tomogram in GOCAD software with the brown surface representing the sub-layer contact. The explored zones are located in various locations along the contact zone. The upper zone is in the immediate vicinity of the contact (in the embayment structure) and the lower zone below the contact in the footwall area. Contact and footwall zones are the two dominant types of mineralization in this area.

As it is evident in the geology model shown in Figure 5-10, the upper zone is a contact mineralization which occurs at the base of the SIC. This type of mineralization consists of dominantly pyrrhotite with minor pentlandite and chalcopyrite. Deposits in this condition are mainly located along radial inflections or depressions in the SIC footwall contact characterized by thickened sublayer which are referred to as troughs (Morrison, 1984). Within these trough structures, second order embayment known as terraces act as traps for sulphide concentrations. The distribution ranges from finely disseminated in the upper portions of the sublayer through to semi-massive and massive sulphide along the lower contact of the sublayer within the trough or terrace structure. Commonly at the base of the sublayer, a transitional metamorphic textured Late Granite Breccia (LGBX) is host to the largest accumulations of economic sulphide within the terrace environment.

Figure 5-10.c shows that the lower zone is located in the Footwall zone. Footwall deposits are zones of sulphide mineralization which have migrated away from the base of the sublayer or footwall breccia and penetrate deep into the brecciated footwall rocks of the SIC. Footwall deposits occur in the form of massive sulphide veins and smaller subordinate stringers and disseminations within footwall Sudbury breccia. Sulphides in the footwall environment tend to be dominantly chalcopyrite with lesser amount of pentlandite and cubanite. As well, significant precious metal bearing minerals are present. These deposits often exhibit zonation outwards proximal to the contact, and Fe and S-poor sulphides near the outer margin of the deposit (Morrison, 1984).

6 RIM Tomograms derived from ImageWin and FARA software compared with the lithology and conductivity logs

6.1 Overview of LogView software

LogView is an application written to run in the Microsoft Window 3.1 operating system. It was developed by the Geological Survey of Canada for the side-by-side display of multiple geophysical logs collected with several downhole tools. In addition, the lithology can be plotted on its own as colours and patterns and with labels for the lithology. It can also be displayed as an infill (color or patterned) underlying the log traces. The imported data files can be either ASCII or binary format and the file created in LogView can be saved as a GSC file.

An example of the LogView display for MAC100G and MAC104 is shown in Figure 6-1.a and Figure 6-2.a. The logs are displayed between 1200 and 1800 m, with tick marks every 100 m on the depth axis. Using LogView, we can compare the electrical conductivity measurements made proximal to the hole (using the electrical conductivity log) with those made between the hole using the cross-hole radio imaging method. The cross-hole data presented are the FARA processed data (as conductivity) and the ImageWin processed results (as conductivity). Plotting the results in this way allows the results to be compared as a function of depth down the hole. Two LogView plots were generated for MAC104 and MAC100G. The geology and IFG

conductivity recorded in MAC100G are shown in Figure 6-1.a and Figure 6-1.b, and the geology and IFG conductivity recorded in MAC104 are shown in Figure 6-2.a and Figure 6-2.b. The measurements using the IFG conductivity probe were taken every centimeter and the details of the IFG instrument is given in Appendix D.

The tomograms derived by GEOFARA Ltd, St-Petersburg, Russia on behalf of FARA Systems Canada Ltd and the conductivity data file generated using ImageWin software use a grid with a different number of cells in the X and Y directions. Thus, to get a value at a specific depth Z, the average value at that depth was calculated for the whole tomogram using Excel. The average profiles were then imported into LogView and displayed next to MAC100G and MAC104 (Figure 6-1.b and Figure 6-2.b).

The geology and geophysical logs are plotted as depth down hole, but the FARA and ImageWin profiles are vertical depth. As MAC100G and MAC104 are inclined holes, the depth had to be adjusted for 370 m for MAC100G and 320 m for MAC104. The adjustment for MAC100G is greater in comparison to MAC104 mainly because the former is inclined at a shallower angle.

6.2 Profiles for MAC100G

Figure 6-1 shows the RIM conductivity profiles from FARA and ImageWin next to MAC100G. These data were displayed at 10 m intervals. The borehole intersects two major geological units; the SLN (Sublayer Norite), 2) an interbedding of the FGN, SDBX and GAB. The IFG

conductivity log data clearly indicate the zones with higher conductivities proximal to the hole. The conductive mineralization at these locations is consistent with the values from the RIM tomograms which are representative of values more distant from the hole.

The upper conductive zone can be seen at a depth of 1390-1410 m with high values of 590000 ppm (IFG conductivity log); 0.0011 S/m (RIM FARA profile); and 0.00064 S/m (RIM ImageWin profile), respectively. The lower zone is clearly distinguished in a depth of 1490-1550 m with high values of 295000 ppm (IFG conductivity log); 0.0024 S/m (RIM FARA profile); and 0.00032 S/m (RIM ImageWin profile), respectively.

The FARA profile shows that the upper zone with the conductivity of 0.0011 S/m is less conductive than the second zone with the conductivity of 0.0024 S/m. This is in contrast with the results of the conductivity log (Figure 6-1.a and 6.1.b). However, the ImageWin average conductivity profile is consistent with the conductivity log (Figure 6-1.a and 6.1.c).

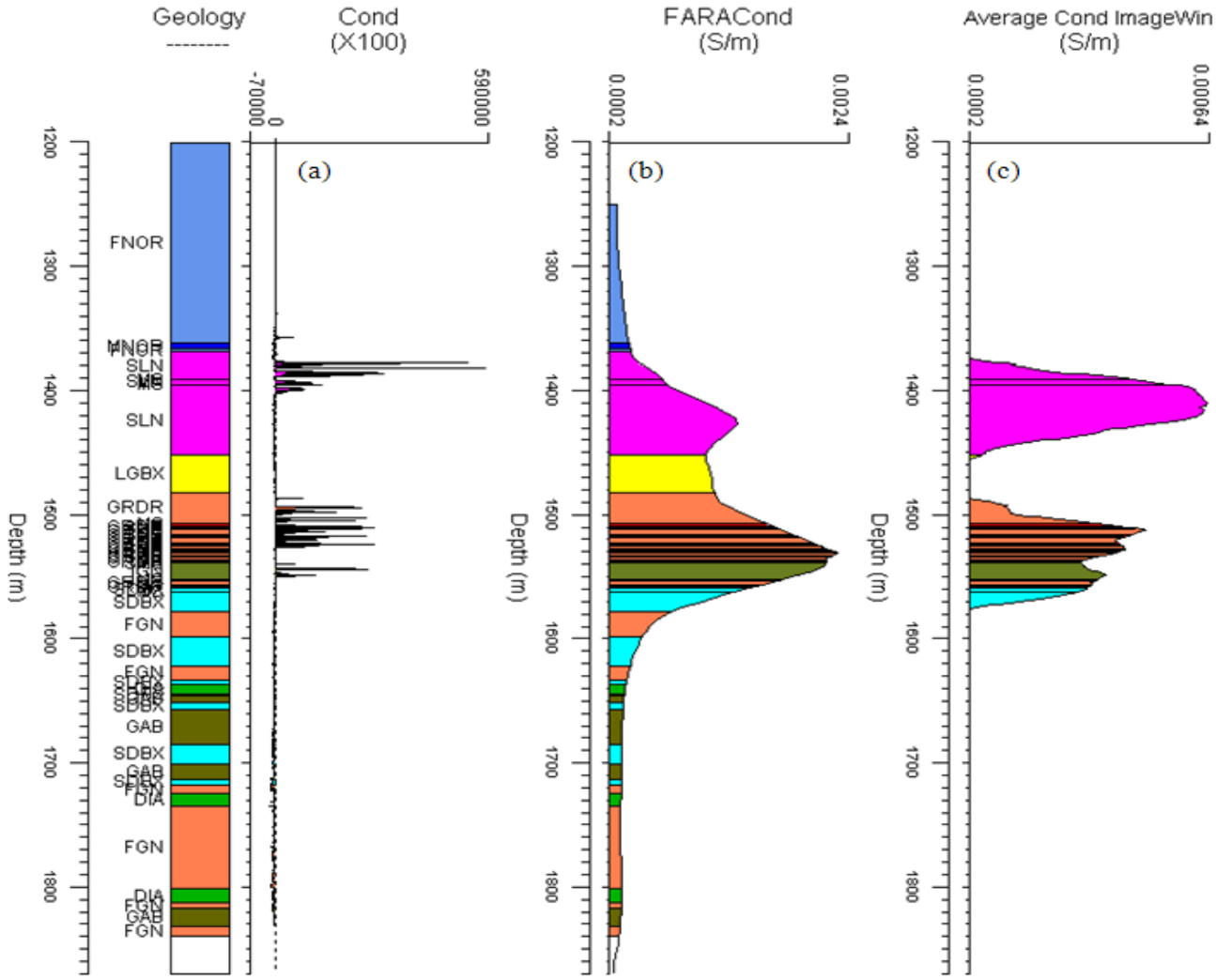

Figure 6-1: (a) Geology and IFG conductivity recorded in hole MAC100G. The highly conductive zones indicate sulphide mineralization within various rock types. (b) is the average RIM conductivity from FARA, and. (c) is the average RIM conductivity from ImageWin. The average is the average at a specific depth range across the tomogram. (Accounting for the 370 m discrepancy in the depth scale). The key geological feature in this section is that the upper zone is located at the base of the SIC (Sudbury Igneous Complex) and the lower zone is below LGBX (Late Granite Breccia), locating in GRDR (Granodiorite) at GAB (Gabbro) and SDBX (Sudbury Breccia).

The range of the minimum and maximum values of the profile is given in Table 6-1.

Table 6-1: The minimum-maximum values of the profiles next to next to MAC100G.

Log	Minimum	Maximum	Unit
IFG conductivity	-70000	590000	ppm
Apparent FARA conductivity	0.002	0.0024	S/m
ImageWin average conductivity	0.0002	0.00064	S/m

6.3 Profiles for MAC104

Figure 6-2 shows the IFG conductivity logs, FARA, and ImageWin profiles next to MAC104, the latter two are plotted with at a depth interval of 10 m. The borehole intersects two major logical units; the SLN (Sublayer Norite), 2) the FGN and SDBX. There are two high conductivity zones.

The upper conductive zone is clearly distinguished in a depth of 1320-1340 m as high values of -400000 ppm (IFG conductivity log); 0.0011 S/m (FARA profile); and 0.00064 S/m (ImageWin profile), respectively. The lower zone is clearly distinguished in a depth of 1450-1480 m as high values of 200000 ppm (conductivity log); 0.0024 S/m (FARA profile); and 0.00032 S/m (ImageWin profile), respectively.

Once again, the upper FARA zone is more resistive, while the ImageWin lower zone is more resistive. The locations and widths of the zones are roughly comparable. The IFG conductivity log is narrower, more erratic in character and in a slightly different location. An exact correspondence between the locations and widths of the zone is not expected. This is because the IFG probe is only sensitive to conductive material very close to the whole, while the RIM data is more distal. Further, the FARA and ImageWin tomograms were different in their location and dip, so the average results are expected to be spatially different. The values are also expected to be different. As we observed from chapter 2 different conductivities can be obtained when doing the tomographic inversion, so an exact agreement between the conductivities is not expected.

The range of values of the profiles next to MAC104 is given in Figure 6-2.

Table 6-2: The minimum-maximum values of the profiles next to MAC104.

Log	Minimum	Maximum	Unit
IFG conductivity	-70000	400000	ppm
Apparent FARA conductivity	0.002	0.0024	S/m
ImageWin average conductivity	0.0002	0.00064	S/m

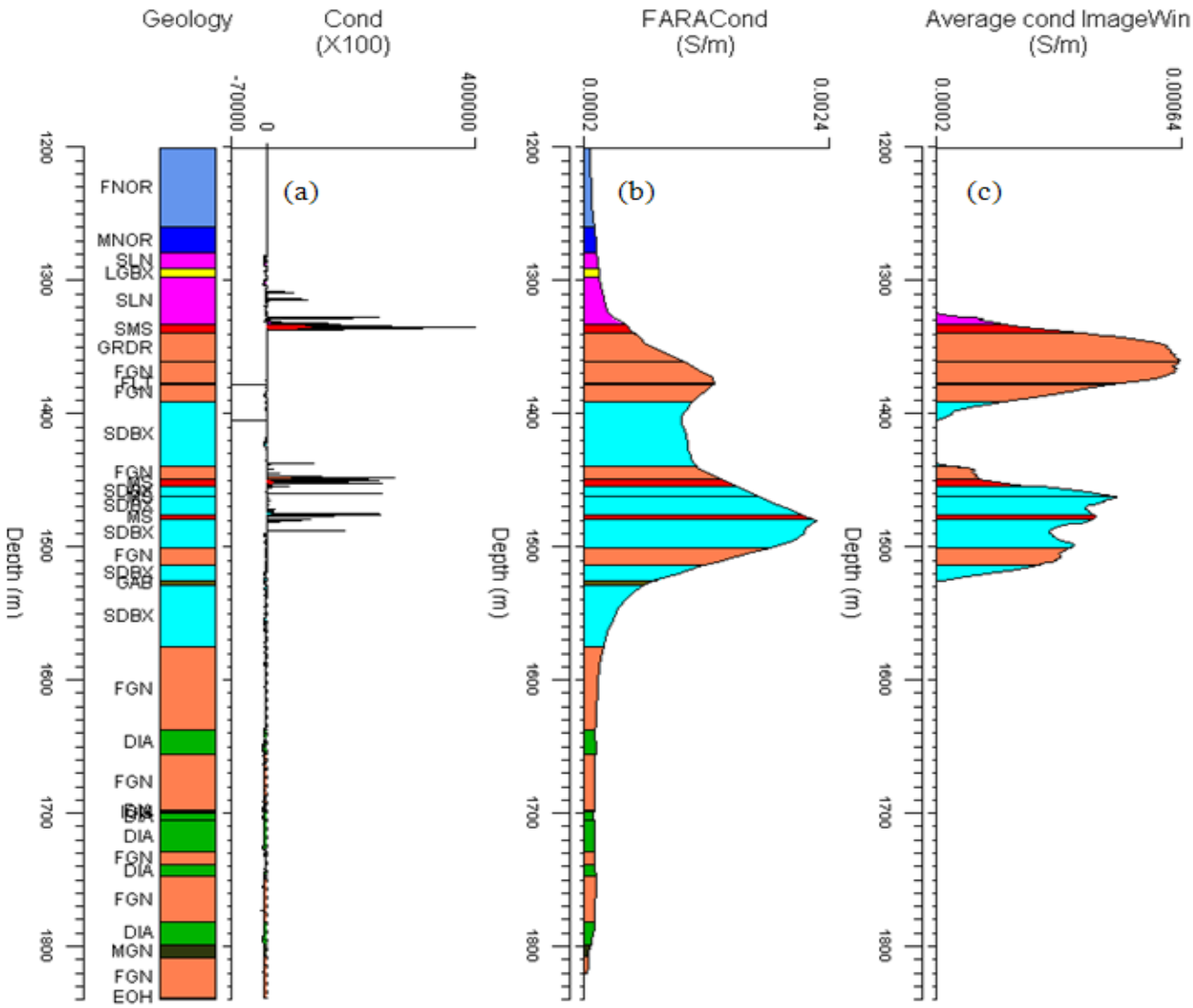

Figure 6-2: (a) Geology and IFG conductivity recorded in hole MAC104. The highly conductive zones indicate sulphide mineralization within various rock types. (b) is the average RIM conductivity from FARA, and (c) is the average RIM conductivity from ImageWin. The average is the average at a specific depth range across the tomogram. (Accounting for the 320 m discrepancy in the depth scale). The upper zone is located in SLN (Sublayer Norite) and the lower zone is located at the SDBX (Sudbury Breccia SDBX) and FGN (Felsic Gneiss).

7 Electromagnetic Theory for Radio Imaging Method Applications

7.1 The conductivity calculation procedure

In order to understand the propagation and attenuation of electric and magnetic fields in the radio imaging method a brief discussion of electromagnetic theory is included in this chapter.

Electromagnetic (EM) wave theory of light was developed by James Clerk Maxwell in 1864 (Sengupta and Sarkar, 2003). A propagating electromagnetic wave in free space consists of an electric field E and a magnetic field H oscillating in a direction perpendicular to each other and to the wave propagation direction as is shown in Figure 7-1(Nabighian, 1988).

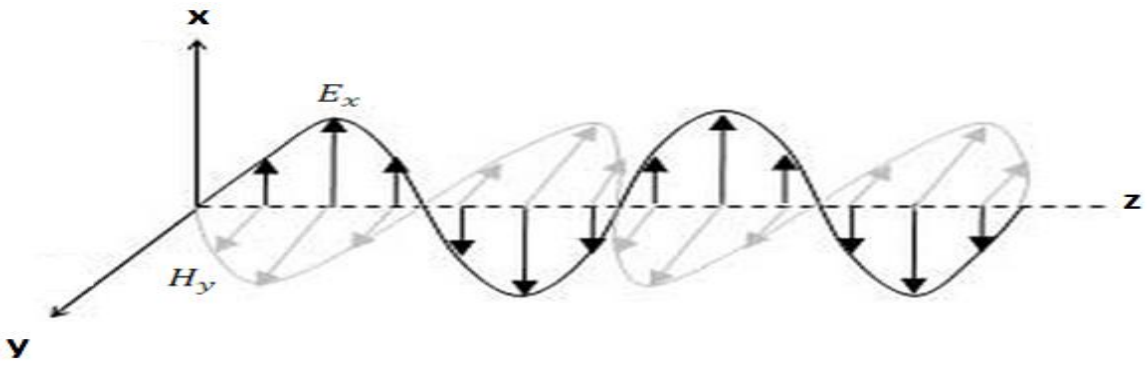

Figure 7-1: A schematic of perpendicularity of electromagnetic wave, the sinusoidal behavior of E_y and H_y as functions of propagation distance z (after Nabighian, 1988).

The nature of electromagnetic fields in rock varies as a function of distance (R) from the transmitter or source. There are three different regions characterized by the relation between R and the EM-field wavelength λ: (1) the near field zone (R<< λ); (2) the intermediate zone (R≅ λ) and (3) the far-field (the radiative) zone (R>>λ). Electromagnetic amplitude tomography is typically carried out when the source and receiver are separated by many wavelengths, so that far-field condition is satisfied (Korpisalo et.al. 2008). The Image Win tomographic software is based on the far-field assumption (Fullagar, 2012).

Following the discussion of (Nabighian, 1988).Maxwell's equations are written as follows:

$$\nabla \times E + \frac{\partial B}{\partial t} = 0 \qquad \textbf{(7.1)}$$

$$\nabla \times H - \frac{\partial D}{\partial t} = J \qquad \textbf{(7.2)}$$

$$\nabla . B = 0 \qquad \textbf{(7.3)}$$

$$\nabla . D = \rho \qquad \textbf{(7.4)}$$

There are four electromagnetic vector fields $\boldsymbol{E}$,$\boldsymbol{B}$, $\boldsymbol{D}$, and $\boldsymbol{H}$ where, $\boldsymbol{E}$ is the electric field intensity in (V/m); $\boldsymbol{B}$ is the magnetic induction in (Wb/m^2 or Tesla); $\boldsymbol{D}$ is the dielectric displacement (C/m^2) and $\boldsymbol{H}$ is the magnetic field intensity (A/m). Equation (7.1) shows the relationship between the curl of electric field strength $\boldsymbol{E}$ and the time derivative of the magnetic

flux density. By the same token, equation (7.2) establishes similar relationship between the curl of magnetic field $\boldsymbol{H}$ and the derivative of electric displacement field with respect to time. Equation (7.3) shows that the divergence of electric displacement vector D is equal to the electric charge ρ and equation (7.4) shows that the divergence of magnetic flux density B is zero.

Considering these equations separately, none of the equations express the relationship between the behavior of the electromagnetic field and the subsurface structure of the earth and its properties. As a result, each rock property appears to affect the electromagnetic field independently. There are three constitutive equations that can be combined to form a single number that is characteristic of the medium, the "wave number", which determines the behavior of the electromagnetic field.

The first constitutive law is Ohm's law which states that the current density is proportional to the electric field intensity and the constant of proportionality is the electric conductivity, σ, a characteristic property of the media.

$$J = \sigma E. \qquad (7.5)$$

Another constitutive equation relates the electric field intensity to the displacement current. The dielectric permittivity, ε, is the constant of proportionality and this is another characteristic property of the medium.

$$D = \varepsilon E. \tag{7.6}$$

The dielectric permittivity of free space is 8.854×10^{-12} and value of dielectric permittivity in most rocks is approximately the same.

Furthermore, the magnetic permeability μ is a physical property of the medium that relates the magnetic intensity $\boldsymbol{H}$ and the magnetic induction $\boldsymbol{B}$, such that,

$$B = \mu H. \tag{7.7}$$

In vacuum, the magnetic permeability is $4\pi \times 10^{-7}$ H/m.

Substituting these constitutive equations in 7.1 and 7.2 and taking the curl of both sides gives:

$$\nabla \times \nabla \times E + \nabla \times (\frac{\partial}{\partial t}(\boldsymbol{\mu H})) = 0 \tag{7.8}$$

$$\nabla \times \nabla \times H - \nabla \times (\frac{\partial}{\partial t}(\boldsymbol{\varepsilon E})) = \nabla \times (\sigma E) \tag{7.9}$$

Assuming all the physical properties are constant in the medium and as a function of time, equations (7.8) and (7.9) reduce to:

$$\nabla \times \nabla \times E + \boldsymbol{\mu}\nabla \times (\frac{\partial H}{\partial t}) = 0 \tag{7.10}$$

$$\nabla \times \nabla \times H - \boldsymbol{\varepsilon}\nabla \times (\frac{\partial \boldsymbol{E}}{\partial t}) = \sigma \nabla \times E \qquad (7.11)$$

Using the curl identity

$$\nabla \times \nabla \times a = \nabla\nabla.a - \nabla^2 a = 0 \qquad (7.12)$$

and equations (7.1), and (7.2), and using the fact that the divergence of the magnetic flux and the electric field in a charge free region are zero (equations (7.3) and (7.4)) these equations become:

$$\nabla^2 E + \mu\varepsilon \frac{\partial^2 E}{\partial t^2} + \mu\sigma \frac{\partial E}{\partial t} = 0 \qquad (7.13)$$

$$\nabla^2 H + \mu\varepsilon \frac{\delta^2 H}{\partial t^2} - \mu\sigma \frac{\partial h}{\partial t} = 0 \qquad (7.14)$$

When the conductivity is zero, these are wave equations for the electric and magnetic fields, stated in the time-domain.

Fourier transformation of equations (7.17) and (7.18) with respect to times leads to

$$\nabla^2 E + (\mu\varepsilon\omega^2 - i\mu\sigma\omega)E = 0 \qquad (7.15)$$

$$\nabla^2 H + (\mu\varepsilon\omega^2 - i\mu\sigma\omega)H = 0 \qquad (7.16)$$

or,

$$\nabla^2 E + k^2 E = 0\ , \qquad (7.17)$$

$$\nabla^2 H + k^2 H = 0 \,, \tag{7.18}$$

where

$$k^2 = \omega^2 \mu\varepsilon - i\mu\sigma\omega \,, \tag{7.19}$$

a single values that contains all the physical rock properties of the medium in addition to the frequency. This number characterizes the interaction of the electromagnetic field with the medium.

Considering a uniform medium with properties $\mu, \varepsilon,$ and σ where these values are constant in the formula can be solved.

Plane wave solutions of the wave equation:

Equations (7.17) through (7.18) are second order linear differential equations; two basic solutions are of interest. First for a sinusoidal time dependent $e^{-i\omega t}$

$$E = E_0^+ \, e^{-i(kz-\omega t)} + \, E_0^- e^{i(kz+\omega t)} \tag{7.20}$$

$$H = H_0^+ \, e^{-i(kz-\omega t)} + \, H_0^- e^{i(kz+\omega t)} \,, \tag{7.21}$$

where the (+) designates (the decay in the positive direction) the upgoing wave and the (–) the (decay in the negative direction) downgoing wave. Assume a uniform, homogeneous medium, in which the electric field has only an *x* component, the magnetic field has only a *y* component, and the amplitude of the two fields vary only in the positive *z* direction (downward). If we split the *k* into real and imaginary parts,

$$k = \alpha - i\beta, \tag{7.22}$$

The solution of the equation (7.20) and (7.21) when decay in the positive ***z*** direction may be written:

$$E = E_0^+ \, e^{-i(kz-\omega t)} = E_0^+ e^{-i\alpha z} e^{-\beta z} e^{-i\omega t} \tag{7.23}$$

$$H = H_0^+ \, e^{-i(kz-\omega t)} = H_0^+ e^{-i\alpha z} e^{-\beta z} e^{-i\omega t} \tag{7.24}$$

Solving the equations, the real and imaginary parts of the *k* are (Nabighian, 1988).

$$\alpha = \omega \left\{ \frac{\mu\varepsilon}{2} \left[(1 + \frac{\sigma^2}{\varepsilon^2\omega^2})^{\frac{1}{2}} - 1 \right] \right\}^{\frac{1}{2}} \tag{7.25}$$

$$\beta = \omega \left\{ \frac{\mu\varepsilon}{2} \left[(1 + \frac{\sigma^2}{\varepsilon^2\omega^2})^{\frac{1}{2}} + 1 \right] \right\}^{\frac{1}{2}} \tag{7.26}$$

Rearranging (7.25) the conductivity can be calculated from the attenuation:

$$\sigma = \omega\varepsilon\sqrt{\left(\frac{2\alpha^2}{\omega^2\mu\varepsilon}+1\right)^2-1} \qquad (7.27)$$

The attenuation coefficient (α) as computed during tomographic reconstruction is usually expressed in dB/m. However, in the conversion formula (7.27) α is in neper/m. Therefore, in computing conductivity from ImageWin attenuation coefficients the conversion factor from dB/m to neper/m is applied first (P. Fullagar pers. com):

$$\alpha\left(\frac{neper}{m}\right) = \frac{\alpha(\frac{dB}{m})}{20\log_{10} e} \approx \frac{\alpha(\frac{dB}{m})}{8.686} \qquad (7.30)$$

In the above formula, $\omega = 2\pi f_0$ is frequency in radian per second and f_0 is the operating frequency in Hz.

7.2 The conductivity calculation using data set (Rx=MAC104, Tx=MAC100G)

The two reciprocal tomograms derived using the optimal parameters in Chapter 4 (Figure 4-20 and Figure 4-21) show that the attenuation range is 0.10 to 0.45 dB/m and the associated conductivity range is 0.0002 to 0.0012 S/m (834-5000 ohm-m. In this section, the exported attenuation and conductivity obtained from (Rx=MAC104, Tx=MAC100G) shown in Figure 7-2 and the calculated conductivity values from attenuation values are plotted as a function of the Z

direction in order to precisely identify the difference between the exported and calculated conductivity values.

Figure 7-2.a shows that the upper zone is associated with the attenuation value of 0.26 dB/m while the lower zone with the attenuation value of 0.2 dB/m is shows less attenuation than the upper zone (Figure 7-2.b).

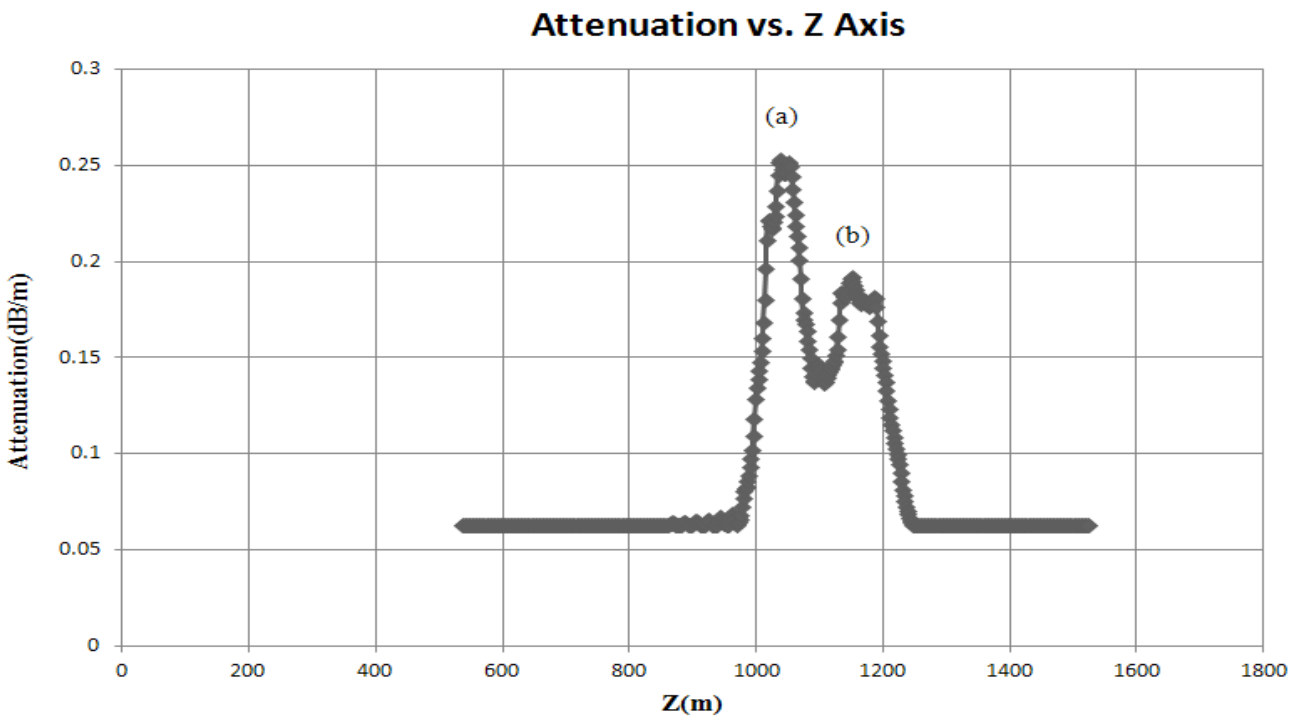

Figure 7-2: Exported attenuation in dB/m from ImageWin versus Z axis. (a) First attenuated zone. (b) Second attenuated zone. (this would be better for a range of z from 400 to 1600).

The exported conductivity values show a value of 0.00094 S/m for the upper zone (Figure 7-3.a) and the value of 0.0008 S/m for the second zone (Figure 7-3.b).

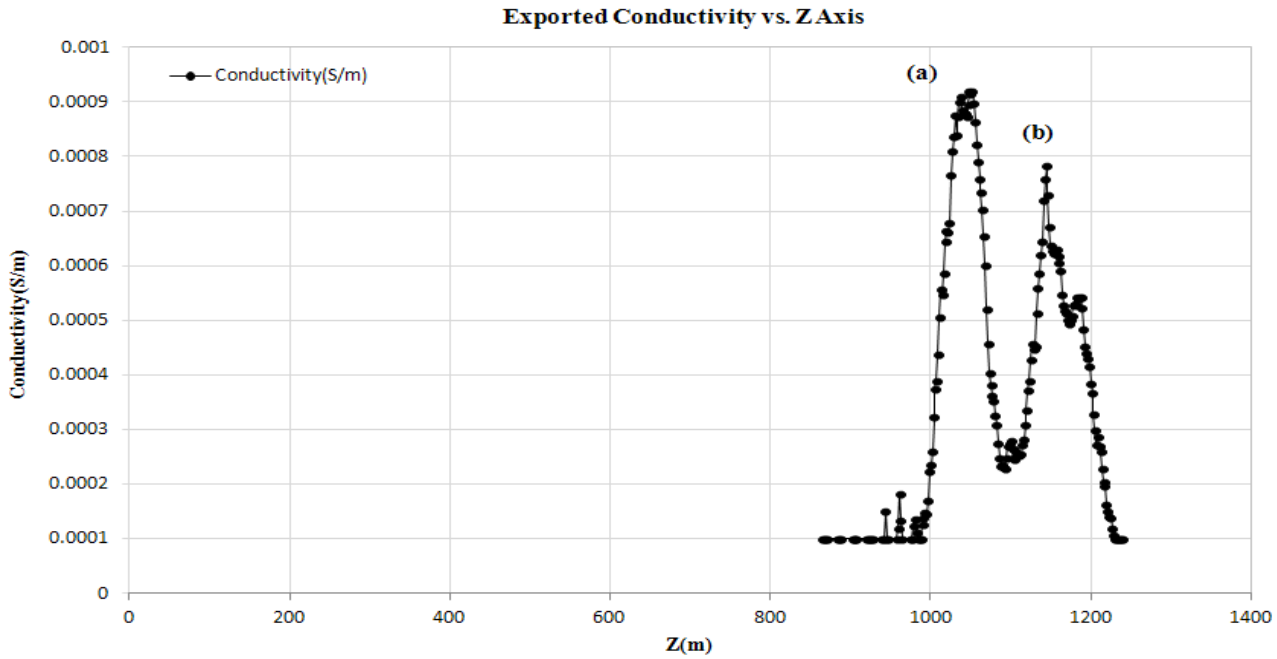

Figure 7-3: Exported conductivity in S/m from ImageWin versus Z axis. (a) First conductive zone. (b) Second conductive zone. Again, use the z range 400 to 1600.

The values of attenuation (α in dB/m) were converted to neper/m in equation (7.30), and then the value of angular frequency ($\omega = 2\pi f$), i.e. 3926990 radian per second for 625 kHz, the permeability value of $\mu_0 = 4\pi 10^{-7}$[Henry/m] for free space; the permittivity value of ε_0= $(1/(36\,\pi))\,10^{-9}$ [Farads/m] for free space, the electrical conductivity values were calculated in

Siemens/meter (S/m). The calculated conductivity values show the value of 0.00023 S/m for the upper zone (Figure 7-4.a) and the value of 0.00098 S/m of the lower zone (Figure 7-4.b).

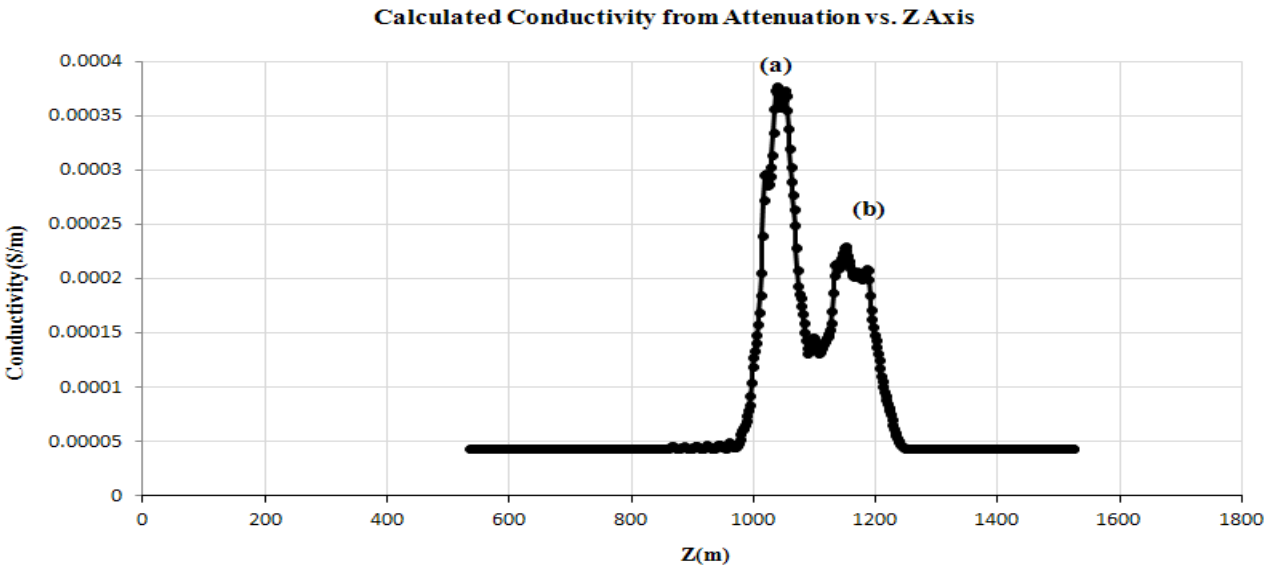

Figure 7-4: Calculated Conductivity using the exported attenuation. (a) First conductive zone. (b) Second conductive zone. (use the same z range 400-1600).

Table 7-1: The summary table of the attenuation, exported conductivity and calculated conductivity

Conductive Zones	**Attenuation**	**Exported Conductivity**	**Calculated Conductivity**
Upper Zone	0.26 dB/m	0.00094 S/m, (R=1063 ohm-m)	0.00038 S/m (R=2631 ohm-m)
Lower Zone	0.2 dB/m	0.0008 S/m, (R=1250 ohm-m)	0.00023 S/m (R=4347 ohm-m)

The upper zone is shown with the attenuation value of 0.26 dB/m (Figure 7-2.a) with the exported conductivity value of 0.00094 S/m (Figure 7-3.a) and the calculated conductivity of 0.00038 S/m (Figure 7-4.a). The lower zone is shown with the attenuation value of 0.2 dB/m (Figure 7-2.b) with the exported conductivity value of 0.0008 S/m (Figure 7-3.b) and the calculated conductivity of 0.00023 S/m (Figure 7-4.b). It is not clear why there is a discrepancy in the calculated and exported values.

One of the parameters that most strongly impacts on the tomograms is the global source strength. As the global source strength increases, the apparent conductivity increases. Therefore, one possible explanation for the relatively low apparent conductivities perceived at McLennan Township can be attributed to the fact that the global source strength is very small (158.8 dB) in those areas. However, there are other possible explanations. Probably the most important consideration is the loss of sensitivity in high absorption zones. If the signal amplitude decreases beyond the sensitivity of the receiver, then the RIM system will be unable to register further increases in conductivity. Moreover, the lower amplitudes will be more prone to noise. ImageWin does allow a great deal of flexibility is setting the source strength either setting one global value for all stations, or setting the value at each station individually. The latter approach might yield greater conductivities, but it is a great deal of work and was beyond the scope of this study.

On the other hand, perhaps the mineralization is disseminated and sparse rather than semi-massive or massive. In that case, the low conductivities may be valid. The assumption that the mineralization might be in low grade or thin veins of high grade is confirmed by downhole logs.

Conclusions

This study was intended to explore the occurrence of electrically conductive sulphide-based ore bodies in an otherwise highly resistive host rock by using the radio imaging method (RIM) and to explore the data processing capabilities of the ImageWin software to construct the conductivity tomograms and to locate attenuated zones. The rationale behind the RIM method was described and various features of the ImageWin software were experimented with. On the basis of the experimental data and computed tomograms, the following conclusions can be drawn from this research study:

1. The electromagnetic wave is drastically attenuated within the conductive zone at MacLennan Township. The high degree of attenuation can be inversely correlated to the low amplitude of the electromagnetic wave. The conductivity tomograms constructed from reduced amplitude data using the ImageWin software confirm that the most conductive zones are coincide with the most strongly attenuated zones. In ImageWin, the attenuation tomograms were computed based on the homogeneous space and far-field propagation assumptions. However, prior to creating the radio imaging tomography using the ImageWin software, one must undergo the following steps:

a. **Importing data:** This is done using files of the correct format, which can be generated using executable programs supplied by Fullagar Geophysics. For the data set processed, this was problematic, possibly because the reciprocal data sets were in the same file, or because there were some repeat measurements. The problem was solved by splitting the file into the two reciprocal data sets.

b. **The ImageWin program provides a quality control capability:** The amplitude masking tool was able to produce images that showed attenuated rays. This could be used to identify zones of attenuation and to check that the transmitter and receiver positions were correctly positioned. The ray masking tool allows the user to examine the ray path coverage.

c. **Inversion procedures using sensitivity analysis:** In order to obtain optimal results with the ImageWin software, experimentation was undertaken to determine the best processing parameters to use. The Vmin experimentation was virtually equivalent to changing the colour bar for the tomogram. The parameters Vmin and Vmax are intended to constrain the tomogram when rock property data are available. Different tomographic algorithms show different responses to the increased number of iterations. Both SIRT and CGLS algorithms showed reduction in the RMS misfit and larger conductive zones away from the transmitter as the number of iterations increased from 1

to 10. However, the LSQR and ART algorithm tended to diverge with the increased number of iterations. The SIRT inversion algorithm gave a very small data misfit after one iteration, and continued to give small improvements The CGLS algorithm reached a comparable level of data misfit, but required multiple iterations. The SIRT and CGLS tomograms actually looked very similar. The results obtained using ART algorithm appeared to be very noisy, showing ray-path artifacts. Editing and smoothing the results improved the appearance of the images. The initial velocity model had little impact on the results. Increasing the cell size resulted in smoother images and a corresponding loss in resolution. In this example, good results were obtained without weighting or clamping. These conclusions were based on the sensitivity analysis performed for this study and cannot be applied to other situations or data sets. Hence, to be able to successfully use ImageWin in another situation, a similar sensitivity analysis should be undertaken.

d. **Generating a single tomogram:** In this study, the reciprocal data sets were used to generate two conductivity tomograms. Although these two reciprocal tomograms were used for data quality control, there was still a need to generate a single tomogram as a final result for interpretation and comparison with other data. The Geosoft software was used to calculate a

single conductivity tomogram from two reciprocal tomograms. This result could be read into GOCAD, which provides a flexible platform for image processing of the results.

2. Comparison made between the locations (depth and dip) and conductivity values at MacLennan Township site (MAC104-MAC100G) showed that the radio imaging method is very sensitive to the distribution of the sulphide zones within the resistive rock. At the MAC104-MAC100G panel in the MacLennan Township, two highly conductive zones were identified and depicted both in a form of raw data (in MATLAB) (Figure 3-2 and Figure 3-3) and in a form of processed data using the LogView profile tools. The upper conductive zone can be conveniently identified at the downhole depth of 1320-1340 m next to MAC104 and 1390-1410 m next to MAC100G and the lower conductive zone is clearly distinguished at the downhole depth of 1450-1480 m next to MAC104 and in a downhole depth of 1490-1550 m next to MAC100G, whereas, the raw amplitude data showed a significant decrease between the depth of 1400 and 1560 m next to MAC100G and between the depth of 1320 and 1520 m next to MAC104. Therefore, solely relying on the acquired attenuation data can result in misinterpretation of the depth and dip of the conductive zones. The primary objective of performing a RIM survey is to image the shape of the conductive zones between the holes.

3. The conductive values predicated by the ImageWin processing software and the FARA processing software for the MacLennan Township region were slightly different while both results appeared to be able to qualitatively discriminate the conductive zones and the insulating resistive rock. The resulting average resistivity of the upper zone was modeled by ImageWin to be approximately 653 ohm-m higher than the average resistivity value determined by FARA. The average resistivity of the second zone is approximately 2709 ohm-m higher when determined by FARA compared to that predicted by ImageWin. The stratigraphy in the Sudbury area is extremely resistive in general, typically > 10^4 ohm.m and the average conductivity value obtained from ImageWin and displayed in Geosoft seems to be more reasonable compared to the result obtained from FARA. The detailed investigation of the ImageWin modeling techniques was performed in this research project. Substantially different results could be obtained in ImageWin using different algorithms, weighting, clamping, iterations, Vmin etc. However, due to the proprietary nature of the modeling process, only limited information about the FARA modeling package is available. Presumably there is similar variability in the FARA imaging algorithm, so quite different FARA results could also be obtained. Therefore, the results obtained from these two different modeling tools, FARA and ImageWin, cannot be directly compared which limited our ability to further analyze the results obtained from the FARA modeling tool.

4. It was shown that in the MacLennan region with the ore body of relatively high conductivity and with the range of frequencies that was used in this study, the attenuation profile is mainly governed by the distribution of conductive material within the resistive rock. The effects of dielectric permittivity and magnetic susceptibility of both conductive ore body and resistive rock were not investigated in this study. The attenuation profile is strongly dependent on the conductivity values within the given FARA frequencies. It was determined that the conductivity values of conductive ore bodies at this MacLennan site range from σ: 10^{-4} to 10^{-2}S/m and the attenuation α ranges from 0.1 to 0.45 dB/m at a frequency of 625 kHz.
5. The 625 kHz and 1250 kHz tomograms were quite different, with the higher frequency showing less resolutions and smoother results. This is contrary to what we might expect, since high frequencies normally correspond to shorter wavelengths and superior resolution. Perhaps it is a consequence of the higher frequencies being more strongly attenuated and containing poorer information. This is something which would have been interesting to investigate, both in terms of the raw data and the subsequent processing.

References

Anderson, C.G. and Logan, K.J., 1992. The history and current status of geophysical exploration at the Osborne Cu Au deposit, Mt. Isa. Exploration Geophysics, vol. 23, no. 1-2, 1-8.

Bohren, C. F., and Huffman, D. R., 2008. Absorption and scattering of light by small particles. Wiley.com.

Bureau International des Poids et Mesures, 2006. The International System of Units (SI), Organization Intergouvernementale de la Convention du Mètre, 8th edition, http://physics.nist.gov.pdf.

Devon G. Parry., 2012. A comparison study of physical property measurements collected around the Sudbury basin. Laurentian University M.Sc. Thesis. Department of Earth Sciences.

Fallon, G.N., Fullagar, P.K. and Sheard, S.N., 1997. Application of geophysics in metalliferous mines. Australian Journal of Earth Sciences, vol. 44, no. 4, 391-409.

FARA website: http://www.farasystem.ru/index.htm, 2002.

Fullagar, P.K., Zhang, P., Wu, Y. and Bertrand, M.J., 1996. Application of radio frequency tomography to delineation delineation of nickel sulphide deposits in the Sudbury Basin: SEG 66th Annual International Meeting & Exhibition, Denver, Extended Abstracts, 2065-2068.

Fullagar,P., 2012. CMTE Tomographic Software Package,

http://www.fullagargeophysics.com/downloads/flyers/flyer_ImageWin.pdf.

Heikkinen, E. J., Korpisalo, A., Jokinen, T., Zhienbaev, T., Shuval-Sergeev, A., Popov, N., and Ahokas, T., 2006. Crosshole radiowave imaging (RIM) at eurajoki, olkiluoto, Finland. Paper presented at the Near Surface 2006; 12th European Meeting of Environmental and Engineering Geophysics; Extended Abstracts and Exhibitors' Catalogue, 5.

Killeen, P.G., and Elliott, B.E., 1997. Mine site exploration and ore delineation, In proceedings of Exploration 97, Decennial International Conference on Mineral Exploration , 1003-1014. Edited by A.G. Gubins, GEO F/X Inc. 709–712.

Korpisalo, A., 2005. Radio imaging surveys with FARA equipment: Crosshole surveys in drillhole sections OL-KR4-OL-KR10 and OL-KR10-OL-KR2 in Olkiluoto with FARA. GTK Geological Survey of Finland, Q16.

Korpisalo, A., Jokinen, T., Popov, N., Shuval-Sergeev, A., Zhienbaev, T., Heikkinen, E. J., and Nummela, J., 2008. Review of crosshole radiowave imaging (FARA) in drillhole sections OL-KR4-OL-KR10 and OL-KR10-OLKR2 in Olkiluoto. Working report, GTK Geological Survey of Finland, FGUNPP (Geologorazvedka) and Pöyry Environment Oy.

Kruger, R.A., Kopecky, K.K., Aisen, A.M., Reinecke, D.R., Kruger, G.A. and Kiser, W.L., J., 1999. Thermoacoustic CT with radio waves: a medical imaging paradigm. Radiology, vol. 211, no. 1, 275-8.

Manohara, S.R., Hanagodimath, S.M. and Gerward, L., 2011. Energy absorption build up factors of human organs and tissues at energies and penetration depths relevant for radiotherapy and diagnostics. Journal of Applied Clinical Medical Physics, vol. 12, no. 4, 296-312.

Markarian, D., Grant, J.A. and Elliott, B.E. 1995. LogView – A Microsoft Winodws 3.1 application to view borehole log (geophysical and geological data); Geological Survey of Canada, Open File 3055.

Monaghan, W. D., 2007. Experimental studies of electromagnetic signals to enhance radio imaging method (RIM): M.S. thesis, West Virginia University.

Morris, W.A., 1984. Paleomagnetic constraints on the magmatic, tectonic, and metamorphic evolution of the Sudbury Basin region. In Pye, E.G., Naldrett, A.J. and Giblin, P.E. (eds.), The Geology and Ore Deposits of the Sudbury Structure. Ontario Geological Survey Special Volume 1, 411-427.

Mutton, A.J., 2000. The application of geophysics during evaluation of the Century zinc deposit, Geophysics, vol. 65, no. 6, 1946-60.

Nabighian, M. N., 1988. Electromagnetic methods in applied geophysics: Applications Part A and B. Vol.2. Society of Explration Geophyicists.

Nahin, P.J., Heaviside, O, 2002. The life, work and times of an electrical genius of the Victorian Age. Johns Hopkins University Press.

Nickel, H. and Cerny, I., 1989. More effective underground exploration for ores using radio waves, Exploration Geophysics, vol. 20, no. 3, 371-377.

Nuzzo, L., Leucci, G., Negri, S., Carrozzo, M.T. and Quarta, T., 2002. Application of 3D visualization techniques in the analysis of GPR data for archaeology. Annals of Geophysics 45,no.2.

Pears, G.A., and Fullagar, P.K., 1998. Weighted tomographic imaging of radio frequency data. Exploration Geophysics, vol. 29, no. 4, 554-559**.**

Prada, J., Fratta, d., and Santamarina, J.C., 2000. Tomographic detection of; low-velocity anomalies with limited data sets (velocity and attenuation). Geotechnical Testing Journal, vol. 23, no. 4, 472-486.

Ratnikov K., Fedorov A., Kholodov I., and Peredery. W., 2008. Cross-hole radiowave surveys with the FARA system in the Sudbury Igneous Complex. Logistics and interpretation report. St-Petersburg. Submitted to Wallbridge.

Rust W. M. J., 1938. A historical view of electrical prospecting methods. Geophysics 5, 243-249.

Schweiker, M., 2002. Governor's Commission on Abandoned Mine Voids and Mine Safety [Report]. Commonwealth of Pennsylvania, p.3.

Sengupta, D.L. and Sarkar, T.K., 2003. Maxwell, Hertz, the Maxwellians, and the early history of electromagnetic waves. IEEE Antennas and Propagation Magazine, vol. 45, no. 2, 13-19.

Spies, B.R., 1996. Electrical and electromagnetic borehole measurements: a review. Surveys in Geophysics, vol. 17, no. 4, 517-556.

Stevens, K., Watts, A. and Redko, G., 2000. In-Mine Applications of the Radio-Wave Method in the Sudbury Igneous Complex. Paper presented at the 2000 SEG Annual Meeting.

Stolarczyk, L. G., Horizon, P. S., Peng, S. S., 2003. Advanced electromagnetic wave technologies for the detection of abandoned mine entries and delineation of barrier pillars. Paper presented at the Interactive Forum on Geophysical Technologies for Detecting Underground Coal Mine Voids. http://www.stolarresearch.com.

Stolarczyk, L.G., 2011. Application of radio geophysics to mining engineering. Applied Radio Geophysics Institute for Mining Safety and Productivity, STOLAR research cooperation, SRC - 2011-09,.what is the 8-108. Should it be 108 pages. (http://www.stolarresearch.com).

Thomson, S., Young, J. and Sheard, N., 1992. Base metal applications of the radio imaging method; current status and case studies. Exploration Geophysics, vol. 23, no. 1-2, 367-372.

Thomson, S. and Hinde, S., 1993. Bringing geophysics into the mine; radio attenuation imaging and mine geology. Exploration Geophysics, vol. 24, no. 3-4, 805-810.

Van Schoor, M., Duvenhage, D., 1999. Comparison of crosshole radio imaging and electrical resistivity tomography for mapping out disseminated sulphide mineralisation at a surface test site in Mpumalanga, South Africa. Exploration Geophysics, vol. 30, no. 3-4, 135-139.

Wait, J.R., 1976. Note on the theory of transmission of electromagnetic waves in a coal seam. Radio Science, vol. 11, no. 4, 263-265.

Watts, A., 1997. Exploring for nickel in the 90's, or 'Til Depth us do part. In proceedings of Exploration 97, Decennial International Conference on Mineral Exploration , 1003-1014. Edited by A.G. Gubins, GEO F/X.

Wilkinson, P.B., 2005. Cross borehole electromagnetic tomography: scoping study and literature review. British Geological Survey, Internal report (IR/05/146), 15pp.

Wilson, J. and Patwari, N., 2011. See-through Walls: Motion Tracking Using Variance-Based Radio Tomography Networks, IEEE Transactions on Mobile Computing, vol. 10, no. 5, 612-621.

Wilson, J. and Patwari, N., 2011. Radio Tomographic Imaging with Wireless Networks. IEEE Transactions on Mobile Computing, vol. 9, no. 5, 621-632.

Zhou, B., Fullagar, P.K. and Fallon, G.N., 1998. Radio frequency tomography trial at Mt Isa Mine. Exploration Geophysics, vol. 29, no. 3-4, 675-679.

Appendix A: Sample drill hole files

The following tables are the sample collar and survey files for MAC100G, respectively.

Appendix Table 1: Collar file format

EASTING	NORTHING	ELEVATION
515816.32	5166838.9	300.8

Appendix Table 2: Survey file format

Depth	Azimuth	Dip
0	360	-90
30	99.58	-89.62
60	85.17	-89.47
90	84.27	-89.31
120	76.49	-89.27
150	67.84	-89.21

Appendix B: Detail instruction to generate the ray path file

The SURVEY.exe and XYZsrv.exe files are sent from Fullagar Geophysics in a zip file, but named as TXT files. These must be extracted and then renamed to EXE.

Following are a few steps to create the input file for ImageWin software:

1- Place the SURVEY.exe and XYZsrv.exe files in the directory where the drillhole survey files and FARA data are stored.

2- Open the DOS command window.

3- Type Survey at the DOS prompt in order to run the program; (The parameters of the survey file and collar file are given in one file in a text format). Note that the drill hole collar position (first line of survey file) should be specified as floating point numbers (EASTING, NORTHING, ELEVATION), i.e. without "E" and "N" characters in the first line of the file. By running the survey data for both holes, the XYZ files were created for the location of each compass reading.

4- Type XYZsrv at the DOS prompt in order to run the program and create the ImageWin data file (The inputs to the program are the output transmitter and receiver files from the Survey program and the raw FARA file which is exported using the FarEdit software and were save as, i.e. All data (*.dat).txt.

Appendix C: Removing the kinks problem at the end of the holes

A file with (x, y, z) for the transmitter hole and (x, y, z) for the receiver hole, plus the calculated amplitude and phase were used to create the input data file for ImageWin. When the data from MacLennan Township were imported as a complete data set, the borehole traces showed kinks at the bottom of the tomogram (Appendix Figure 1). The reason for this issue can be better understood by knowing how the data were acquired. During FARA data acquisition, the data were collected in "Tx gathers", i.e. transmitter stationary with the receiver moving. When the reciprocal data set is acquired, this is done by swapping the Tx and Rx from one hole to the other half way through the survey. On this survey, it appears that at some locations data was collected twice; on the way down and then on the way up. When the data and the reciprocal data are stored in one file and imported into ImageWin, it appears that the routine that assigned locations to each data point got confused. The imported data is shown in Appendix Figure 1 (masking range option using a low-cut amplitude value of 90 dB). The borehole trace goes down and then near the bottom suddenly changes of direction and goes up which does not happen in boreholes as they normally keep going down.

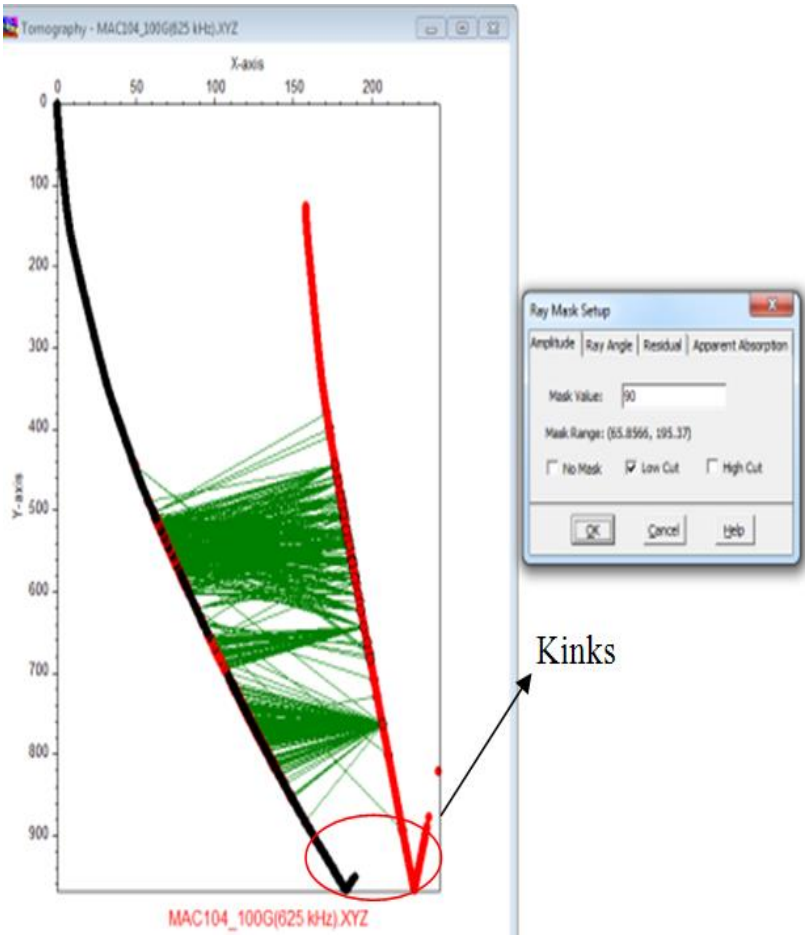

Appendix Figure 1: Ray Mask Set-up for amplitude of 90 dB/m.

The conductivity tomogram was calculated using the complete data set and the default inversion parameters were used for tomographic reconstruction (Appendix Figure 2). The resulting tomograms are displayed as a front view (Appendix Figure 3.a) and a back view (Appendix Figure 3.b), where the latter is simply a mirror image of the former. The ImageWin tomograms show two attenuated zones and kinks at the bottom of the boreholes. Therefore it is obvious that

the borehole geometry has not been correctly represented during the tomography and hence the results will be suspect.

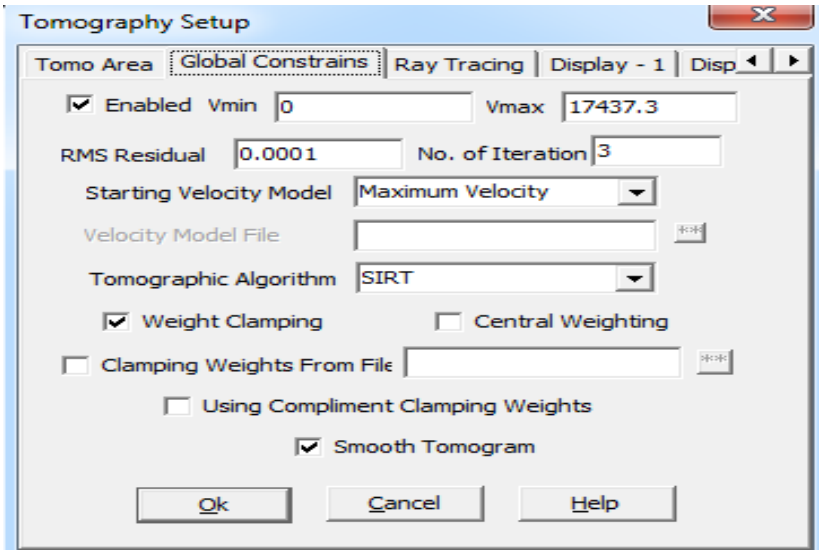

Appendix Figure 2: Inversion parameters for tomogram reconstruction

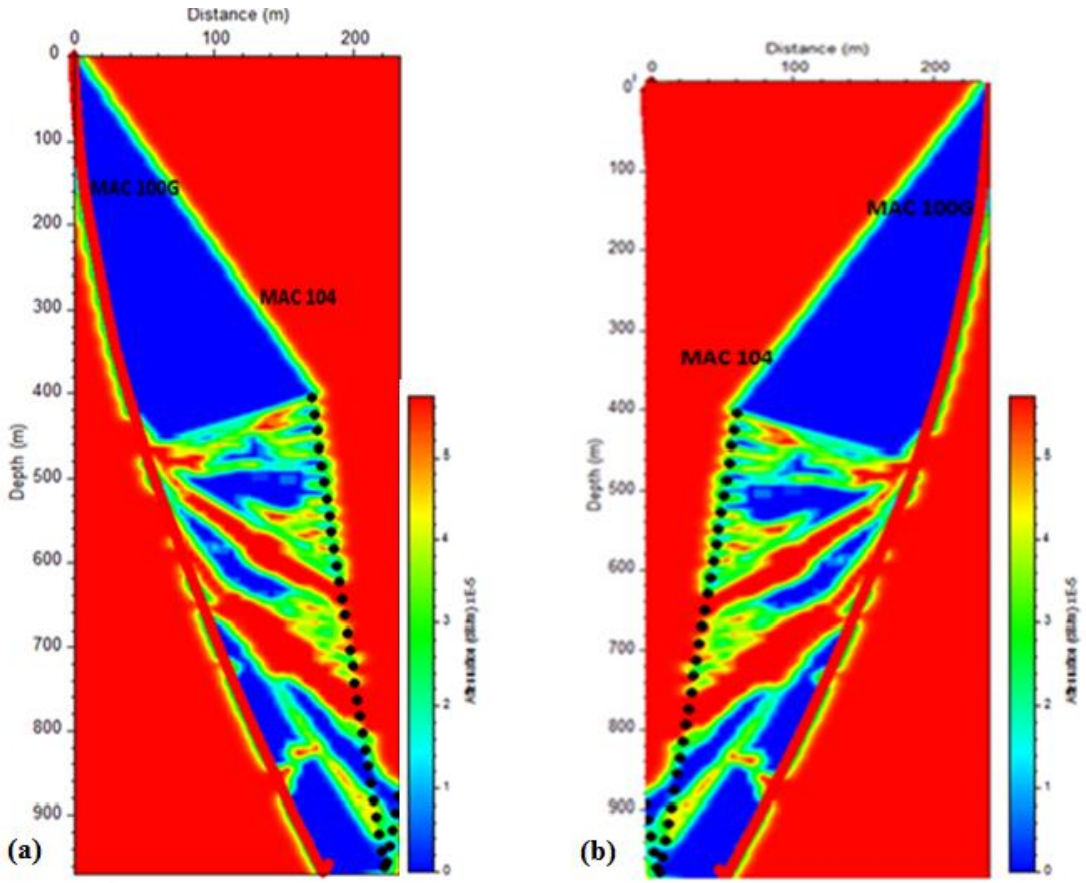

Appendix Figure 3: (a) Attenuation tomogram the front view. (b) Attenuation tomogram the back view.

In order for ImageWin to have the correct borehole geometry, it is necessary to edit the locations or delete the repeat stations. This means looking at the repeat data, deciding which is best and manually moving stuff around in the data file, which seems to be a time-consuming process. The best solution proposed for solving this issue, was to separate the FARA raw data into 2 subsets: (Tx=MAC104, Rx=MAC100G) and the reciprocal data set (Rx=MAC104, Tx=MAC100G). These two files contained the amplitude and phase information at both frequencies. In these two

files, the transmitter depth in one hole is fixed for many records in succession while the receiver depth in the other hole varies. The two files were examined separately to see if this was the case.

Separate tomograms were generated for the two subsets. These "reciprocal tomograms" show identical borehole traces with no kinks at the bottom (Appendix Figure 3). There are some differences in the tomograms. The results were shown very crude (no editing or smoothing) tomograms, but at least they are fairly consistent with one another in terms of broad features. This was a starting point for further refinement. Understanding these differences will help to understand the ImageWin program.

Finally, a single tomogram can be generated by combining the results from the two reciprocal data sets (see Chapter 5).

Displaying the results in the form of Appendix Figure 3.a and Appendix Figure 3.b is an important quality control (QC) procedure. It showed the miss-interpretation of the measurement locations in the borehole.

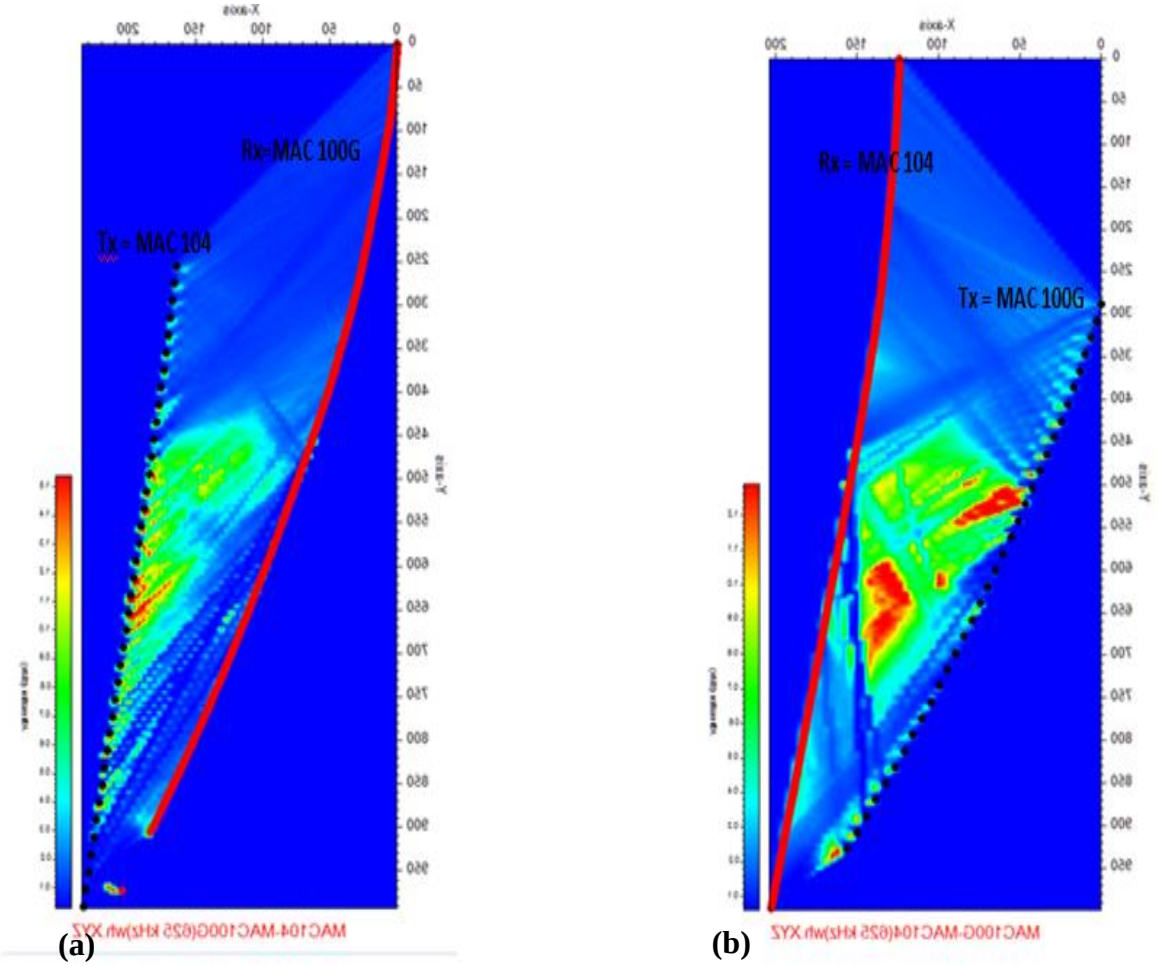

Appendix Figure 4: Tomograms from the two reciprocal data sets (using the default values in the inversion and with no editing or smoothing applied). The black dots are the transmitter locations and the red line is the trace of the hole with the receiver. (a) Attenuation tomogram for (Tx=MAC104 and Rx=MAC100G). (b) Attenuation tomogram for (Tx=MAC100G and Rx=MAC104).

Appendix D: Details of the IFG instrument

The physical rock properties are collected using IFG multi parameter probe (BMP-06) and the details of the specifications of this multi parameter probe are given in Appendix Table 4 (IFG website). This multi-probe is provided by the IFG (Instrumentation for geophysics). A Canadian owned Company that has been designing and manufacturing instrumentation for borehole geophysics since 1979. IFG is well-known for developing a wide range of borehole sensors to meet the needs for the mining, geophysics, geotechnical and environmental industries (http://www.ifgcorp.com/index.phtml).

The combo probe of BMP-06 measures the parameters of inductive conductivity, magnetic susceptibility, galvanic resistivity, natural gamma and temperature. The sensors and the electronics circuits are contained within the probe of the size of 170 cm by 40 mm. All measurements are taken synchronously at a rate of 2 times per second. Including the gamma counts are integrated over a time period of 0.5 second with a maximum dead time of 30 ms or 6% (http://www.ifgcorp.com/index.phtml).

The table above implies that the inductive conductivity outputs the data in calibrated conductivity units (mS/m), however, the data was uncalibrated in ppm.

Appendix Table 3: the details of the specifications using IFG multi parameter probe (BMP-06), (IFG website).

Probe management	
8 bit micro-controller	
Sample rate	2 Hz, all sensors synchronous
Data transfer	2400 baud, 5mA current loop
Power	48 VDC @100mA
Probe mechanics	
Diameter	40 mm up to 1500 m depth
Diameter	42 mm up to 3000 m depth
Diameter	34 mm up to 500 m depth
Length	168 cm
Weight	5 kg
Magnetic Susceptibility Sensor	
Length	30 cm
Sensitivity	10uSI
Resolution	+/- 1uSI
Range	1uSI to 2 SI units
Method	AC induction, near 2 kHz
Temperature stability	50uSI / C
Conductivity Sensor	
Length	10 cm
Sensitivity	10mS/m
Resolution	+/- 1mS/m
Range	10mS/m to 200 S/m
Method	AC induction at 38 kHz
Natural Gamma Sensor	
Size	38.6cm^3
Detector material	CsI
Energy	100 KeV to 3 MeV
Range	0 to 500 k CPS
Units	Counts/0.5 sec
Region of interest	Total count, K40, Bi214 and Tl208
Resistivity array	
Size	40 cm normal array
Sensitivity	1 mV
Resolution	0.1 mV
Range	+50 V to - 50 V
Method	Constant current (5mA)
Temperature	
Size	20 X 0.9 mm
Sensitivity	0.1 m °C
Range	0 to 50 °C
Method	Thermistor

Appendix E: Magnetic susceptibility data in borehole logs

In the previous sections, the conductivity values from similar depths across the image were calculated and averaged and used to compare with the borehole logs. However, it should be noted that the results obtained by averaging the conductivity data at a specific depth across the image might tend to distort the conductivity numbers. In this section the conductivity values from reciprocal data sets derived using ImageWin and the conductivity values of a single FARA tomogram were imported into ArcGIS software and the conductivity values within 10 meters of the boreholes were extracted from ArcGIS for comparison at specific depths with values measured in the boreholes (Appendix Figure 1).

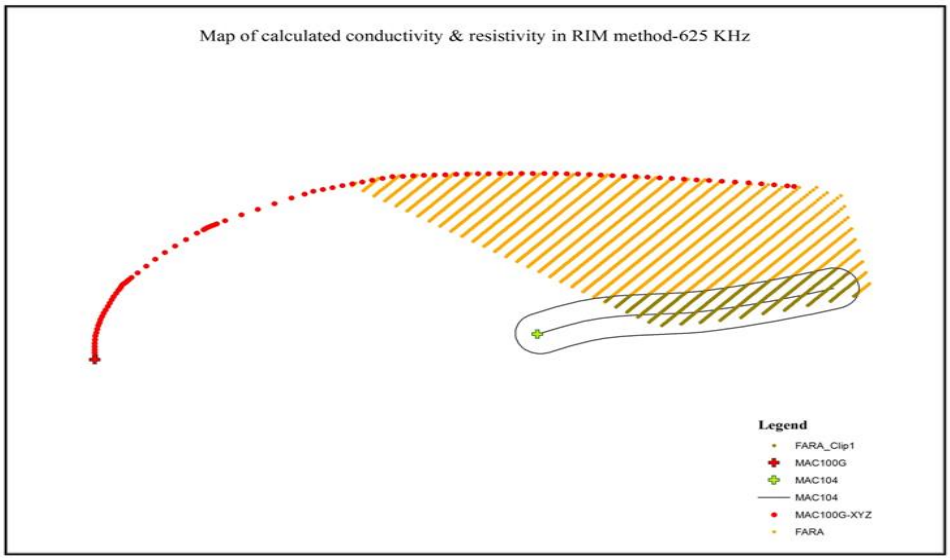

Appendix Figure 5: The region map of exported FARA and ImageWin data from ArcGIS.

The exported conductivity values for 10 meters buffering next to MAC104 and MAC100G were imported in LogView software and compared with borehole logs. This was done for the FARA tomogram and the two reciprocal ImageWin tomograms.

The results for MAC100G are in Appendix Figure 6 and MAC104 in Appendix Figure 7.

For the ImageWin results10 meters away from MAC100G, there are two profiles. One is when the receiver is in MAC100G and the transmitter in MAC104. In the case when the receiver is in MAC100G, there are two conductive zones; the location of the upper zone is consistent with the borehole conductivity logs while the location of the lower zone is slightly shallower (~ 60 meters) compared to the location of the lower zone in the borehole logs. The ImageWin profile for the case when the receiver is in MAC104 is very noisy. This is because the transmitter is close to MAC100G and tomograms are noisy close to the transmitter.

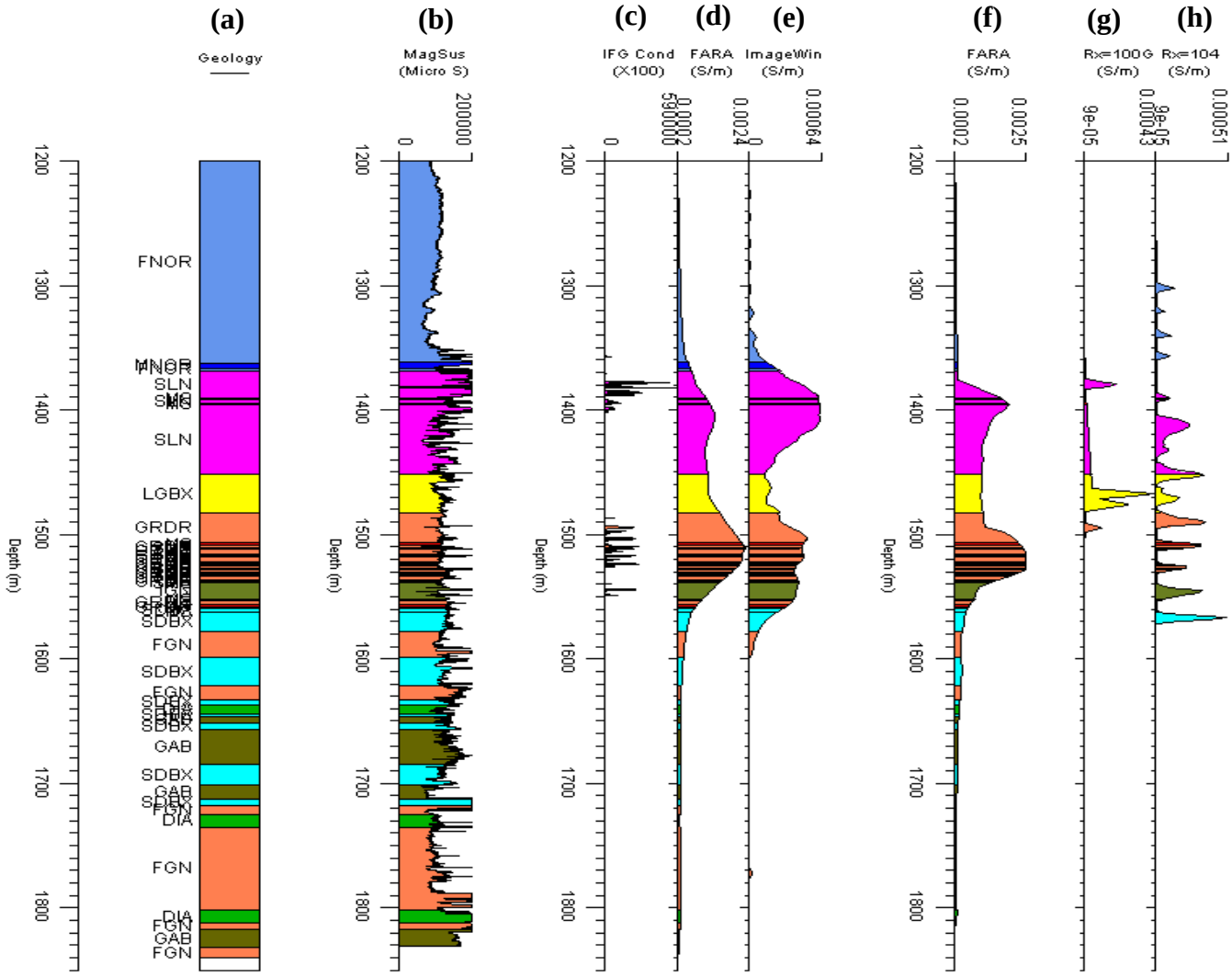

Appendix Figure 6: (a) Geological log, (b) magnetic susceptibility,(c) IFG conductivity (all recorded in hole MAC100G), and (d) is the depth averaged RIM conductivity from FARA, (e) is the depth averaged RIM conductivity from ImageWin. Plot (f) is the FARA profile 10 m away from MAC100G, (g) is the ImageWin profile 10 m away from MAC100G when the receiver is in MAC100G, and (h) is the ImageWin profile 10 m away from MAC100G when the receiver is in MAC104. (Accounting for the 320 m discrepancy in the depth scale).

For case of values close to MAC104, the ImageWin profile for the case when the receiver is in the distant borehole shows noisy results as the transmitter is close to MAC104. However, in the other case there are two conductive zones matching the location of conductive zones obtained from the borehole conductivity logs. The deeper zone is slightly too deep on the ImageWin data and too shallow on the FARA. However, the borehole logs show very rapid variation, suggesting that large variations can occur in 10 metres, so even averaging within 10 metres of the hole is likely to give a different value.

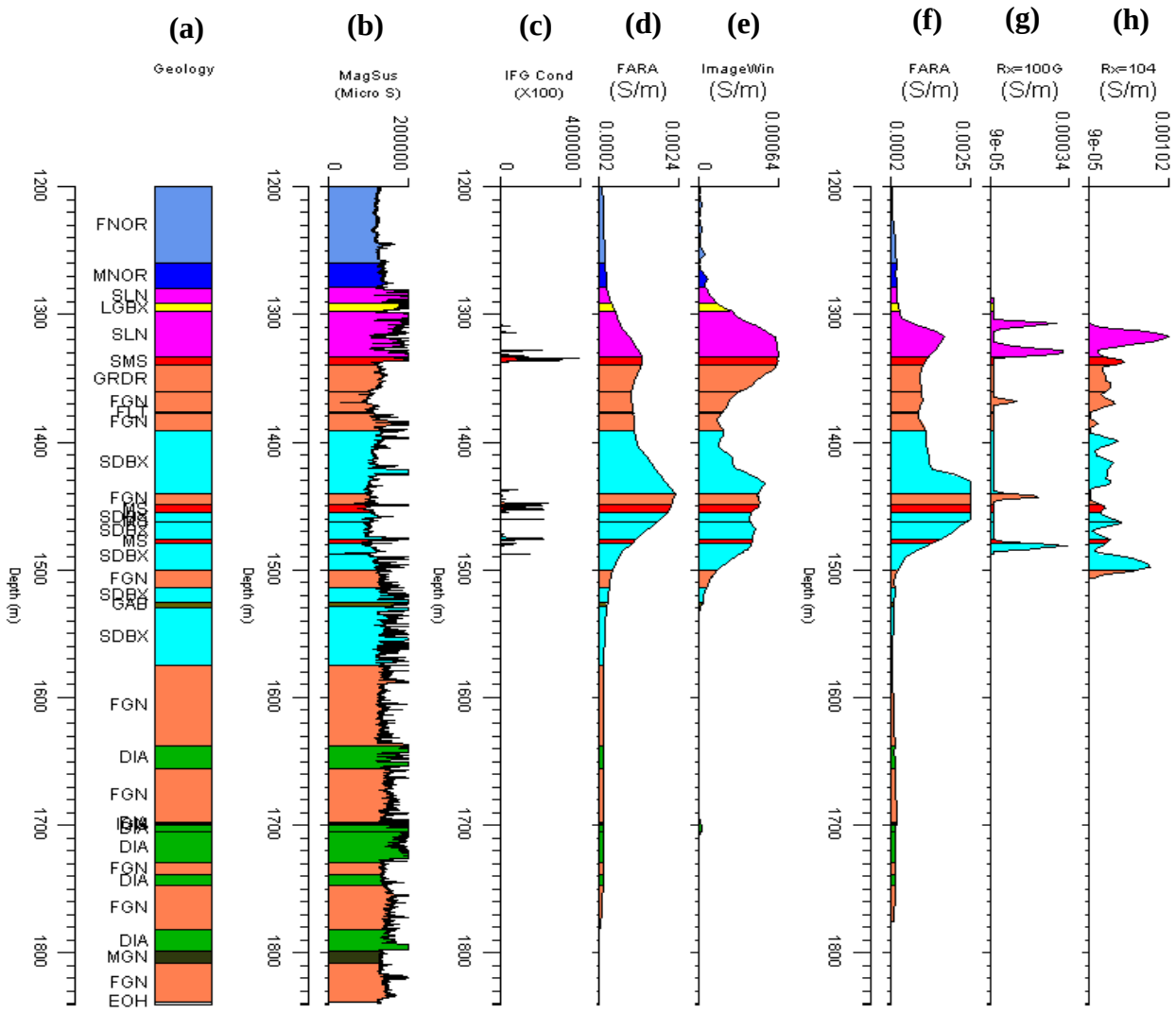

Appendix Figure 7: (a) Geological log, (b) magnetic susceptibility, (c) IFG conductivity (all recorded in hole MAC104), (d) is the depth averaged RIM conductivity from FARA, and (e) is the depth averaged RIM conductivity from ImageWin. Plot (f) is the FARA profile 10 m away from MAC104, (g) is the ImageWin profile 10 m away from MAC104 when the receiver is in MAC100G, and (h) is the ImageWin profile 10 m away from MAC104 when the receiver is in MAC104. (Accounting for the 270 m discrepancy in the depth scale).

The magnetic susceptibility profile shows that SLN (Sub layer Norite) and DIA (Diabase) are more susceptible, while SDBX (Sudbury Breccia) is highly variable. Similar variability was noted in the footwall at Lady Violet (Parry, 2013), a different location but still in the Sudbury area. At Lady Violet Parry, 2013 also noted very rapid variation in the conductivity with depth.

The RIM survey conducted at MAC104-MAC100G revealed that this area has relatively low electrical conductivity values (0.001 to 0.005 S/m). Geologically, however, this area intersects with SLN, LGBX, FGN and SDBX which are all known as the zones of high sulphide concentrations. Therefore, although the RIM proved to be a viable method to capture the conductive zones embedded in an electrically insulating host rock, the scale of measurements 10 m to hundreds of metres is different from the measurements in borehole, so precise agreement is not expected.